Convective Heat Transfer in Boundary Layer Flows of Sisko Fluid

By

Asif Munir

Department of Mathematics
Quaid-i-Azam University
Islamabad, Pakistan
2015

Convective Heat Transfer in Boundary Layer Flows of Sisko Fluid

By

Asif Munir

Supervised
By
Dr. Masood Khan
&
Dr. Abdullah Shah

Department of Mathematics
Quaid-i-Azam University
Islamabad, Pakistan
2015

Convective Heat Transfer in Boundary Layer Flows of Sisko Fluid

By

Asif Munir

A THESIS SUBMITTED IN THE PARTIAL FULFILLMENT OF THE REQUIREMENT FOR THE DEGREE

OF

DOCTOR OF PHILOSOPHY

IN

MATHEMATICS

Supervised
by
Dr. Masood Khan
&
Dr. Abdullah Shah

Department of Mathematics
Quaid-i-Azam University
Islamabad, Pakistan
2015

Convective Heat Transfer in Boundary Layer Flows of Sisko Fluid

By

Asif Munir

CERTIFICATE

A THESIS SUBMITTED IN THE PARTIAL FULFILLMENT OF THE REQUIREMENTS FOR THE DEGREE OF THE DOCTOR OF PHILOSOPHY

We accept this dissertation as conforming to the required standard

1. _____
Dr Masood Khan
(Supervisor)

2. _____
Prof. Dr. Tasawar Hayat
(Chairman)

3. _____
(External Examiner)

4. _____
(External Examiner)

Department of Mathematics
Quaid-i-Azam University
Islamabad, Pakistan
2015

This thesis is dedicated to ...

...my mother (late), for being my first teacher

...my father, for earning an honest living for us

...my lovely kids, Mohammad Faizan, Mohammad Umar and Abdullah

...and my wife.

Acknowledgements

Praise be to **Almighty Allah** and I bow my head with the deepest gratitude to him. Who enabled me to complete this piece of work. He is the Most Powerful, the Most Compassionate, the Most Kind and the Most Merciful. I offer my humblest and sincerest and millions of Durood to Holy Prophet Hazrat **Muhammad** (Peace be Upon Him), who exhorted **His** followers " to seek knowledge from cradle to grave " and showed us the right path.

I would like to express my sincere gratitude to my supervisor, Dr. Masood Khan for the continuous support of my Ph.D. study and related research, for his patience, motivation, and immense knowledge. His guidance helped me in all the time of research and writing of this thesis. I am in deficit of the words to write of his role during this period. My sincere thanks also go to my co-supervisor, Dr. Abdullah Shah, who provided me an opportunity to develop the research related numerical tools.

It was an incredible experience to do research in Quaid-i-Azam University and I truly feel that I was taught by the best and wonderful teachers, my words of thank cannot repay what they have given to me. I also want to express my gratitude to my friends and colleagues like Dr. Azeem Shahzad and Dr. Ayub, who lend a sympathetic ear and encouraged me to keep at it, when I was having a hard time.

I am grateful to my parent department for granting me study leave to complete my Ph. D. studies and Higher Education Commission of Pakistan for providing financial help through HEC indigenous scholarship program to undertake my studies.

Finally, it is a privilege for me to communicate my love for my mother (late, May Allah bless her soul), father, wife, sons, sister and brother and many more for supporting me spiritually throughout this span of time and my life in general.

Asif Munir

Abstract

The main theme of this thesis is to make a solid contribution for a meaningful research study of the boundary layer flows of a non-Newtonian fluid. The research focuses on the flow and convective heat transfer of the Sisko fluid, which is a subclass of a generalized Newtonian fluid. One of the main aims of this work is the mathematical modeling of the governing boundary layer equations for the steady three-dimensional flow over a flat surface and infinite rotating disk. To gain a better insight about the behavior of these flows, numerical and/or analytical solutions are needed. We also focus on the development of solutions for different circumstances. Each problem after being successfully modeled, and with comprehensive results obtained, are meaningfully interpreted.

The problems concerns convective heat transfer which include two-dimensional flow in the planer and axisymmetric over non-linear stretching sheets, flow past a wedge geometry, flow near a stagnation point with nonlinear stretching sheet and with nonlinear radiation effects, three dimensional flow due to a bidirectional stretching surface and flow due to an infinite rotating disk. The transformed boundary layer equations are solved numerically by the implicit finite difference method with Keller box. Further, simple shooting and multiple shooting techniques using adaptive Runge Kutta method with Broyden's/Newton's method in the flow domain are also utilized. In addition, exact solutions of the resulting nonlinear differential equations are also provided in some special cases. In some cases, the obtained numerical results are compared with the analytic solutions obtained by using the homotopy analytic method (HAM) to check the veracity of our results. The presented numerical results are also validated by comparing

them with previously published pertinent literature. The excellent correspondence inspires the confidence in the veracity of our numerical results.

The numerical data for the velocity and temperature fields is graphically presented and the effects of the relevant non-dimensional parameters such as the power-law index, stretching parameter, wall temperature parameter, material parameter of Sisko fluid, Prandtl number, Eckert number, wedge angle parameter, buoyancy parameter, velocity ratio parameter, temperature ratio parameter, radiation parameter, skin friction coefficient and local Nusselt number have been observed by encompassing a broader range. A profound observation is that the temperature profile and the corresponding thermal boundary layer thickness reduce with increasing values of the material parameter of the Sisko fluid. However, it is noted that the material parameter affects the temperature field marginally. In addition, effects of the material parameter on temperature field are more prominent for lower Prandtl number.

Chapter 1

Introduction

This chapter presents the motivation and literature survey and highlights the importance of studying the flow and heat transfer characteristics of the Sisko fluid. Moreover, it provides the structure of the thesis and briefly introduces the solution methodologies.

1.1 Motivation and Literature Survey

With the advent of fast computers and elegant numerical techniques, the modern period has witnessed a significant level of maturity in the simulation of different flow situations for the Newtonian fluid model. However, since the last few decades there has been a growing recognition of the fact that most of the materials of practical and industrial interest do not confirm to the simple Newtonian behavior and accordingly are known as ***non-Newtonian fluids***. The non-Newtonian behavior is more prevalent than generally considered. Many liquid foods are non-Newtonian, including emulsions and suspensions, as well as concentrated solutions that contain starches, pectin, gums and proteins. These liquids often show Newtonian properties at low concentration, but as the concentration of the solution is increased, there is a transition to non-Newtonian rheology.

Newtonian fluids follow simplest linear constitutive relation. Nevertheless, for non-Newtonian fluids, more elaborate constitutive equations, containing several material parameters, are needed to describe the response of these fluids. Presently, there is no universal constitutive model available that describe all non-Newtonian fluid behaviors. To cover the various characteristics of non-Newtonian fluids, several models

have been suggested in the literature. A distinguishing behavior of a large number of non-Newtonian fluids is the shear rate dependent viscosity. This class of non-Newtonian fluids is often called the generalized Newtonian fluids (GNF). A generalized Newtonian fluid differs from a Newtonian fluid only in that the viscosity is no longer independent of the shear rate. The concept of the dependence of the viscosity on shear rate is very useful, and can provide reasonable predictions in many circumstances. Nevertheless, this is able to describe the purely viscous non-Newtonian characteristic and cannot predict all flow phenomena encountered with the non-Newtonian fluids. When the fluid is relatively inelastic, the Sisko fluid model [1] (subclass of generalized Newtonian fluid) can be used to describe the non-Newtonian characteristic associated with shear dependent viscosity.

The Sisko model is a three parameter model that can be used when the viscosity is just coming out of the power-law region of the flow curve [2]. This situation can be dealt with by addition of the Newtonian contribution to the power-law description of viscosity. The Sisko model had been verified experimentally to fit accurately the viscosity data of commercial greases made from petroleum oils with thickening agents over a wide range of shear rate (0.04-22000 sec^{-1}) even wider (0.01-40,000 sec^{-1}) [3]. Other models such as the Powell-Eyring and the power-law cover only narrow ranges of shear rate. Further, the results of the power-law model that represent the flow behavior of a large class of process fluids can be retrieved. Indeed, over the years, significant advances have been made in the area of Sisko fluid flow [4-14].

In many chemical and processing applications, fluids need to be heated or cooled using a wide range of equipment. Such as in extrusion process, which is extensively carried out in the polymer and food industry. Moreover, the life of grease in moving parts of machinery is heavily dependent on temperature in addition to other factors. In most

applications, it is the rate of heat transfer within the process equipment which is of principal interest. However, with thermally sensitive materials (such as foodstuffs, fermentation froths, pharmaceutical formulations), the temperature profiles must be known and maximum permissible temperatures must not be exceeded. Thus, thermal convection plays a significant role during handling and processing of non-Newtonian fluids. Furthermore, shear stresses are generally so high that viscous heat generation can rarely be neglected.

Many technological processes involve the flow and heat transfer over stretching surfaces. Such a phenomenon has attracted many researchers to explore this problem. Some exemplary applications of such study are glass fiber production, the cooling and drying of paper under paper production, drawing of plastic films and so forth. Major research efforts have been commenced over the past few years on the flow and heat transfer of non-Newtonian fluids over a stretching surface owing to its tremendous industrial utilization. Primarily, Schowalter [15] obtained the similarity solutions for the boundary layer flow for the power-law pseudoplastic fluids. Jadhav and Waghmode [16] analyzed the heat transfer to power-law fluid over a permeable flat plate with heat flux boundary condition. Howel *et al.* [17] considered the laminar flow and heat transfer of a power-law fluid over a stretching sheet. Hassanien *et al.* [18] numerically analyzed the flow and heat transfer for a stretching sheet for non-uniform temperature distribution. Able *et al*. [19] studied the flow and heat transfer to a power-law fluid over a stretching sheet by considering variable thermal conductivity and heat source. Indeed, over the years voluminous literature regarding the flow and heat transfer of non-Newtonian over stretching sheet has been developed [20-23]. Flow of a Sisko fluid, caused by planar stretching surface, is comprehensively discussed by Khan and Shahzad [24]. An important variation in the flow induced by a planar stretching surface, is a radially

stretching surface. The same authors [25], investigated the axisymmetric flow of a Sisko fluid and found approximate analytic solutions.

Different investigators have been exploring diversified configurations to study the flow in conjunction with convection. Flow past a wedge has numerous applications in aerodynamics, geothermal systems, heat exchangers and so forth. Different aspects of this problem have been studied over time [26-30]. Beyond the domain of Newtonian fluids, a cursory review of literature reveals that several investigators including Kim [31], investigated the Falkner-Skan wedge flow of a power-law fluid through a porous medium. Chen and Radulovic [32] studied the heat transfer in laminar boundary layer flow of the power-law fluids past a wedge with a step discontinuity at surface temperature Postelnicu and Pop [33] examined the boundary layer flow of a power-law fluid past a porous stretching wedge. Rashidia *et al*. [34] analyzed the flow and heat transfer in a generalized third-grade viscoelastic power-law fluid over a porous wedge. Khan and Shahzad [35] explored the flow of Sisko fluid over a wedge, but limited information regarding power-law index (only integer value) and wedge angle parameter (only positive values) have been noted.

The limiting case when both forced and free convection are of equal importance is termed as mixed (or combined) convection. A number of theoretical studies have appeared in recent years focusing on mixed convection. Abundant information has accumulated in the literature regarding mixed convective heat transfer in non-Newtonian fluids. A concise overview of the available body of knowledge is presented here. Wang [36] investigated the mixed convective heat transfer in the power-law fluid and found non-similar solutions. Steady convection including buoyancy forces in the power-law fluid over a non-isothermal horizontal flat plate was studied by Hady [37]. Chen [38] reported numerically the mixed convection over a non-isothermal vertical stretching

sheet. Moreover, Chen [39] also studied the effects of thermal radiation and heat generation in a mixed convection for magneto-hydrodynamic flow of the power-law fluid. Further, the hydro-magnetic mixed convection flow of a non-Newtonian fluid over a moving plate for a large temperature difference between plate and ambient fluids has been studied by Saleem *et al.* [40]. Barletta [41] studied the mixed convection and flow reversal in a vertical annular duct with power law fluid.

Radiative heat transfer plays an important role in the problem of heat transfer and exerts a significant role on the heat transfer from a heated surface. A continued interest in the field has led to emergence of new research topics during past few years. The thermal radiation effects may be quiet significant at high operating temperatures in engineering processes or in the situation where the convective heat transfer coefficients are small. Over recent years many researchers including, Mohammadein and El-Amin [42], Elgazery [43], Kishan and Kavitha [44] investigated the combined radiation and convection in a non-Newtonian power-law fluid.

More general case of unidirectional stretching surface is bidirectional stretching surface. In bidirectional stretching surface the flow is three dimensional. Some previous works regarding bidirectional stretching surface was carried out by Wang [45], who presented exact similarity solutions for a three-dimensional flow due to stretching of a sheet in two lateral directions. Later, Ariel [46] addressed this problem by finding the approximate analytical solutions using the homotopy perturbation method. Liu and Andersson [47] also explored numerically the heat transfer characteristics of a fluid, when the sheet is stretched in two lateral directions with variable thermal boundary conditions. Lakshmisha *et al.* [48] obtained numerical solutions of unsteady three-dimensional boundary layer with a constant temperature and heat flux thermal boundary

conditions. Ahmad *et al.* [49] provided the approximate analytical solutions of the problem for heat transfer in hydromagnetic flow induced by bidirectional stretching sheet in a porous medium.

Various researchers explored the flow of non-Newtonian fluids due to bidirectional stretching surface, including Gorla *et al*. [50] who addressed the three dimensional flow of a power-law fluid over a bidirectional stretching surface. Recently, Nadeem *et al.* [51] analyzed the MHD three-dimensional Casson fluid flow past a porous linearly stretching sheet. Shehzad *et al.* [52,53] also studied the three-dimensional flow of Maxwell and Oldroyd-B fluids over bi-dimensional stretching surface. Shehzad *et al.* [54] further explored the three-dimensional flow of Jeffery fluid including the effects of magneto-hydrodynamics and Newtonian heating.

Several engineering flows involve swirl or rotation and rotational flows are encountered in turbo-machinery, mixing tanks and variety of other process industries. Admittedly, ever since, the pioneering study of von Karman, on the flow due to a rotating infinite disk, some remarkable works focusing on a topic of vital importance is cited in [55-58]. Extending these works various researchers investigated the flow and heat transfer in a non-Newtonian power-law fluid over an infinite rotating disk. Amongst them, Andersson *et al.* [59] elucidated the role of power-law rheology on the flow over a rotating disk. The effects of magnetic field on the flow of electrically conducting power-law rotating fluid are also illustrated by Andersson and de Korte [60]. Attia [61] studied the steady flow of a power-law fluid induced by a rotating disk with heat transfer in a porous medium in the presence of uniform suction and injection. Ming *et al*. [62] studied the effects of the power-law rheology on complete velocity and temperature fields.

In short, there has been, thus, no previous study delineating forced convective heat transfer to Sisko fluid. Albeit, Ref. [24,25,35,63] are valuable studies regarding the flow of a Sisko fluid, but the value of power-law index is limited to integral values, thus, missing the practical information about highly and moderately shear thinning/thickening $(0.2 \le n \le 2)$ Sisko fluid. Moreover, no prior investigation on the three-dimensional boundary layer flow and heat transfer to Sisko fluid over a bidirectional stretching surface is available. Furthermore, the study about the flow and heat transfer of a Sisko fluid over a rotating infinite disk is added to literature for the first time. The work in this thesis aims to fill this gap in the available literature.

1.2 Structure of the Thesis

There are ten chapters in all, covering different aspects related to convective heat transfer to Sisko fluid and summarized as follows:

The introductory material, *chapter 1* serves as the motivation and contains literature survey as well as the layout of the thesis.

The preliminary material, *chapter 2*, comprises the conservation laws, governing equations, approximations used, some basic concepts and the dimensionless numbers appearing in the subsequent chapters.

Chapter 3 provides an exposition to forced convective heat transfer in the steady boundary layer flow of a Sisko fluid over a nonlinear stretching sheet. The prescribed surface temperature and prescribed heat flux are applied at the heated surface. An extensive range of the rheological parameter and the power-law index has been focused spanning from highly a shear thinning to shear thickening Sisko fluid to investigate the flow and heat transfer characteristics. The governing partial differential equations are reduced to a system of nonlinear ordinary differential equations by using appropriate

transformation and solved numerically. Additionally, exact solutions are obtained in some particular cases. The effect of the pertinent parameters (stretching parameter, wall temperature parameter, material parameter of the Sisko fluid and Prandtl number) on the temperature field are explored in depth. In addition, the local Nusselt number versus wall temperature parameter is also graphed and tabulated for different values of pertaining parameters. This chapter is closed by validation of the numerical results and discussion of the results. We have stressed its importance in our common paper which has been ***published*** in ***PLoS ONE 9 (6): e100056. doi:10.1371/journal.pone.0100056.***

The flow and heat transfer characteristics of a Sisko fluid over a radially stretching sheet with viscous dissipation effects is dealt with in *chapter 4*. Viscous dissipation effects are significant for the flow of high consistency materials (such as polymer melts) [64]. The stretching velocity of sheet is assumed to be nonlinear. The flow and heat transfer aspects are thoroughly investigated particularly for non-integer values of the flow behavior index. The modeled partial differential equations are reduced to a system of nonlinear ordinary differential equations using the appropriate transformations. The resulting equations are then solved numerically by implicit finite difference method with Keller box technique. In addition, the skin friction coefficient and the local Nusselt number for different values of the pertaining parameters are given in tabulated form. Moreover, numerical results are compared with exact solutions as special cases of the problem. Furthermore, the present results for the velocity field are also validated by comparison with the previous pertinent literature. It is also noteworthy that the Bingham plastic and Newtonian fluids are special cases of the Sisko fluid, and a comparison of the momentum and thermal boundary layers characteristics of these fluids is also incorporated in this chapter. This work has been ***accepted*** for publication as a book

chapter in ***"Heat Transfer studies and application", ISBN-978-953-53-4191-4, INTECH Open Science.***

The flow passed a wedge produces different pressure profiles for each value of wedge angle, so we can investigate the boundary layer behavior in a number of situations. *Chapter 5* addresses convective heat transfer to a Sisko fluid over a wedge with viscous dissipation. This chapter analyzes the convective flow of a Sisko fluid past a wedge under the variable free stream velocity in the presence of viscous dissipation effects. The effects of shear thinning and shear thickening on flow and heat transfer are explored in depth. The influence of the wedge angle parameter on flow and heat transfer is spanned from the stagnation point down through the flat plate flow to the separation point. Employing suitable transformations the governing equations are converted to a system of nonlinear ordinary differential equations. The resulting equations are then solved numerically by an implicit finite difference method along with Keller box scheme in the domain $[0,\infty)$. The numerical results for the velocity and temperature fields are graphically presented and effects of the various parameters are discussed in detail. In addition, the displacement thickness, momentum thickness, skin-friction coefficient and local Nusselt number for different values of the pressure gradient parameter are calculated in tabulated form. Also, the present results are compared with the previously published work with an outstanding accuracy. The results of this investigation are ***published*** in the ***Journal of the Brazilian Society of Mechanical Sciences and Engineering.***

Mixed convection heat transfer in a Sisko fluid: effects of assisting and opposing buoyancy are treated in *chapter 6.* Steady mixed convection heat transfer in a Sisko fluid over a vertically stretching surface is considered in this chapter when the imposed and buoyancy induced flows are in the same and opposite directions. The flow is induced due

to nonlinear stretching sheet with a constant temperature distribution. The governing partial differential equations, under the framework of the Boussinesq approximation are transformed into ordinary differential equations using a suitable transformation. These equations are solved numerically using an implicit finite difference method with Keller box scheme for the following ranges of the parameters: the buoyancy parameter $(-3.0 \le \lambda \le 2.0)$, the power-law index $(0.3 \le n \le 1.9)$, the material parameter of the Sisko fluid $(0.2 \le A \le 1.9)$. In particular, the effects of these dimensionless parameters on the velocity and temperature fields, the skin friction coefficient, and the local Nusselt numbers have been graphically sketched. In addition, the numerical results are validated by comparison with analytic results as well as previously published results as a special case of the problem. The contents of this chapter are ***published*** in ***Chemical Engineering Research and Design***.

In *chapter 7*, we study the two-dimensional stagnation-point flow and heat transfer over a flat deformable sheet stretching in its own plane with a nonlinear stretching and free stream velocities. The effects of thermal radiation are incorporated using the nonlinear Rosseland approximation in the energy equation. The appropriate transformation is employed to transform the governing nonlinear partial differential equation to a couple of nonlinear ordinary differential equations. These equations are solved numerically using an implicit finite difference method with Keller box scheme for shear thinning and shear thickening Sisko fluids, encompassing the wider ranges of non-dimensional parameters namely; the material parameter of Sisko fluid, velocity ratio parameter, the radiation parameter, the temperature ratio parameter, and the Prandtl number.

The investigations in *chapter 8* focused on the flow and heat transfer characteristics of the steady three-dimensional Sisko fluid flow driven by a bidirectional stretching sheet. We incorporate the boundary layer equations for three-dimensional flow of an incompressible Sisko fluid in this chapter. The governing nonlinear partial differential equations are modeled and reduced to a coupled ordinary differential equations by utilizing a suitable transformation. The resulting equations are solved numerically by the shooting method using an adaptive Runge Kutta algorithm in combination with Newton's method in the flow domain. The numerical results for the velocity and temperature fields are graphically presented and effects of the relevant parameters are discussed in detail. Moreover, the skin-friction coefficient and local Nusselt number for different values of the power-law index and stretching ratio parameter are presented through tabulated data. The contents of this chapter have been ***accepted*** for publication in ***PLoS ONE***.

Chapter 9 deals with the study of the steady flow and heat transfer characteristics of a Sisko fluid over a rotating infinite disk. The boundary layer equations for incompressible rotating Sisko fluid are derived from the momentum equations and a new addition to the literature of non-Newtonian fluid mechanics is achieved. The flow and heat transfer aspects are thoroughly investigated encompassing a highly shear thinning and shear thickening Sisko fluid. The modeled boundary layer equations are reduced to a system of nonlinear ordinary differential equations using the appropriate transformation. The resulting equations are then solved numerically by a single shooting method for shear thickening and a multiple shooting method for shear thinning fluids in the domain $[0,\infty)$. The numerical data for the velocity and temperature fields are graphically sketched and effects of the relevant parameters are discussed in detail. In addition, the velocity gradients at the disk surface and the local Nusselt number for different values of the pertaining parameters are given in tabulated form. Moreover, a comparison with

previously published work, as a special case of the problem, has been conducted and the results are found to be in excellent agreement. The contents of this chapter have been submitted for publication.

Finally, *chapter 10* concludes the thesis and highlights the contributions made with major findings. Further, it highlights some possible directions for future studies which are briefly outlined.

1.3 Solution Methodologies

Most real world phenomena are modeled by ordinary and/or partial differential equations. Majority of these equations are highly nonlinear and exact solutions of these equations are not possible in general. Although, exact solutions, always give a good account of the physical nature of the phenomena modeled, existing analytical methods can only handle a limited range of these equations. In this work, numerical methods are used to find the solutions of the modeled, highly nonlinear two point boundary value problems. The obtained numerical results are sometimes compared with the previously published literature as a special case of the problem as well as with analytical results provided by the homotopy analysis method (HAM). Amongst the numerical methods, the shooting method using adaptive Runge Kutta method with Broyden's/Newton's method is utilized in chapters 3 and 8, a multiple shooting method in chapter 9, and in the rest of the thesis the solutions are sought by an implicit finite difference technique (Keller box technique). The shooting method certainly has the advantage of the speed and adaptability of methods for initial value problems, but the convergence to a solution may crucially depend on the choice of the initial guess. The multiple shooting method works better than the simple shooting method, owing to the fact that exponentially growing solution components have less time to grow large before they are reinitialized [65].

The Keller box scheme is an implicit finite difference scheme for finding numerical approximate solutions of differential equations. The nonlinear ordinary differential is written as an equivalent system of first order system and derivatives are approximated by central differences. The resulting set of nonlinear difference equations are linearized using the Newton's quasi-linearization technique and are solved using a block-tridiagonal algorithm [66]. A good initial guess satisfying boundary conditions guaranties rapid convergence. It is second order accurate, unconditionally stable and has fast convergence rate, which reduces the computation time and consumes less memory.

It is worthy to mention that the value of numerical infinity η_∞ changes as the value of the power-law index varies from highly shear thinning to shear thickening regimes and the step size of $\Delta\eta = 0.001$ is set. The results are generally given to six significant decimals and are considered accurate to 10^{-5}.

Chapter 2

Preliminaries

This chapter comprises the basic concepts and governing equations relevant to this thesis. The dimensionless numbers generally appearing in the flow and heat transfer phenomena are briefly discussed. Additionally, the equations of motion for flow of non-Newtonian Sisko fluid are derived in this chapter.

2.1 Conservation Laws

The conservation laws of mass, momentum, and energy are the cornerstone of fluid mechanics. The flow and heat transfer associated with any fluid is governed by the transport equations; namely continuity, momentum and thermal energy equations which are derived from these conservation laws are briefly outlined below in general tensorial form.

2.1.1 Continuity Equation

In differential form the continuity equation can be stated as

$$\frac{\partial \rho}{\partial t} + \nabla \cdot (\rho \mathbf{V}) = 0, \tag{2.1}$$

where ρ represents the fluid density, t the time and $\mathbf{V}$ the velocity vector. For the incompressible and time independent flow, Eq. (2.1) simplifies to

$$\nabla \cdot \mathbf{V} = 0, \tag{2.2}$$

whether the flow is steady or not. Here ∇ is the vector gradient operator.

2.1.2 Momentum Equation

The momentum equation plays a pivotal role in fluid mechanics and can be developed by the application of Newton's second law of motion for an arbitrary control volume. The differential expression of momentum equation for an incompressible, steady and laminar fluid flow, as vector equation can be expressed as

$$\rho(\mathbf{V}\cdot\nabla)\mathbf{V} = -\nabla \mathrm{p} + \nabla\cdot\mathbf{S} + \rho\mathbf{B}, \tag{2.3}$$

where ρ is density of the fluid, p the pressure, $\mathbf{B}$ the body force per unit mass and $\mathbf{S}$ the extra stress tensor. Due to the fact that the momentum equation (2.3) is a vector equation, for a general three dimensional problem, it involves four unknowns; namely, the pressure and three components of velocity vector.

2.1.3 Energy Equation

The energy equation may be obtained by applying the first law of thermodynamics to a control volume. It describes that changes in energy, heat transferred and work done by a system are in balance. For a fluid with constant thermal conductivity, the fundamental energy equation for steady flow in vector form is

$$\rho c_p(\mathbf{V}\cdot\nabla)T = -\nabla\cdot\mathbf{q} + \mathbf{S}\cdot\mathbf{L} + \rho\mathbf{r}, \tag{2.4}$$

where c_p is specific heat at constant pressure, $\mathbf{r}$ the possible heat source or sink per unit mass, T the temperature, $\mathbf{S}$ the extra stress tensor, and $\mathbf{q}$ the heat flux given by Fourier's law of heat conduction as

$$\mathbf{q} = -\kappa\nabla T, \tag{2.5}$$

where κ is the thermal conductivity of the fluid.

2.2 Modes of Heat Transfer

Basically, heat transports in three ways, namely conduction, radiation, and convection. In many cases heat transports in all the three modes simultaneously. Heat conduction is primarily a molecular phenomenon. Energy transfer by this mode is carried out in two ways: firstly, the molecules at a higher energy level impart energy to molecules at lower energy level and secondly, by free electrons. The former exists in all the systems (fluids, solids) in which temperature difference is present, the latter is significant in metallic solids.

Radiative heat transfer between surfaces requires no medium for propagation. A perfect vacuum between surfaces maximizes the energy transfer by radiation. Radiations travel at the speed of light. The electromagnetic spectrum between 0.1 and 100 μm is associated with thermal radiation and is termed as thermal band. Liquids containing gases, such as carbon dioxide and water vapor, and glasses transmit only a portion of incident radiation, while most of solids are essentially opaque to radiation.

2.3 Convection

Heat transfer by convection involves the energy exchange between a surface and an adjacent fluid by the movement of fluid. It is usually the dominant form of heat transfer in liquids and gases, it occurs extensively in practice. Heat is transferred in convection by the combined process of conduction (heat diffusion due to difference in temperature) and advection (heat transfer mass motion of fluid). The rate of heat transfer in this mode depends not upon the details of flow field but also on the fluid properties. *e.g* cooling of

the components of a computer, heating and cooling of buildings *etc*. There are three modes of convective heat transport.

2.3.1 Natural Convection

Natural convection refers to flow induced by heating of fluid that would otherwise be motionless in absence of heat transfer. The fluid motion is generated only by the density changes in the fluid occurring due to temperature gradients. In this mode fluid surrounding a heat source becomes hot, consequently becomes less dense and rises. The surrounding, cooler fluid then moves to replace it. This cooler fluid is then heated and the process continues, as a result convection current is formed, this current transfers heat energy from the bottom of the convection cell to the top. The driving force for natural convection is buoyancy, which is a result of differences in fluid density.

2.3.2 Forced Convection

In forced convection heat is transferred due to the fluid motion caused by some external means such as a fan, pump or moving boundary and not due to buoyancy forces. Common examples include heat radiator in the vehicles, heat transfer to a fluid due to a heated stretching surface are familiar examples of forced convection.

2.3.3 Mixed Convection

The flows in which the fluid is forcefully directed over a surface and the effect of buoyancy force are also significant, such flows are termed as mixed convective flows. An example of this would be a fan blowing upward on a heated plate. Since heat naturally rises, the air being forced upward over the plate adds to the heat transfer.

2.4 Fluid

We can define a fluid as the material that deforms continuously under the application of some external force, *i.e.* a fluid can flow and has no three dimensional rigid structure.

2.4.1 Newtonian and non-Newtonian Fluids

The Newton's law of viscosity states that the shear stress is directly proportional to the shear rate and the fluids obeying this law are called Newtonian fluids. Mathematically, it can be represented by

$$\tau_{yx} = \eta\left(\frac{\partial u}{\partial y} + \frac{\partial v}{\partial x}\right), \tag{2.6}$$

where τ_{yx} is the shear stress, $\frac{\partial u}{\partial y}$ and $\frac{\partial v}{\partial x}$ the shear rates and η the viscosity of the fluid appears as a constant of proportionality. A Newtonian fluid bears a constant viscosity at a given pressure and temperature. Such fluids include air, water, and many solutions with low molecular weight.

But, several fluids of practical importance behave in a way, which is not adequately described by the above Newton's law of viscosity. These fluids are commonly grouped together under the wider heading of ***non-Newtonian fluids.***

2.4.2 Generalized Newtonian Fluids

Unlike, the Newtonian fluid, it is very difficult to provide a universal constitutive model for non-Newtonian fluids, because they possess very complex molecular structure. A distinct feature of many non-Newtonian fluids is the dependence of apparent viscosity on the shear rate. This dependence of the apparent viscosity on the shear rate introduces the

modification of the constitutive relation of the Newtonian fluids and the resulting constitutive equations are called the generalized Newtonian fluids. In generalized Newtonian fluids the major difference is that the viscosity is no longer independent of flow kinematics.

A number of empirical models are available in the literature to describe the dependence of the apparent viscosity on the shear rate. A widely used amongst these models is the Ostwald–de Waele model for the power-law fluid, that can be expressed as

$$\tau_{yx} = \eta_{app}\left(\frac{\partial u}{\partial y} + \frac{\partial v}{\partial x}\right), \tag{2.7}$$

where

$$\eta_{app} = K\left|2\left(\frac{\partial u}{\partial x}\right)^2 + 2\left(\frac{\partial v}{\partial y}\right)^2 + \left(\frac{\partial u}{\partial y} + \frac{\partial v}{\partial x}\right)^2\right|^{\frac{n-1}{2}}, \tag{2.8}$$

in which K and n are constants for a particular fluid.

The simplest extension of the power-law model is the Sisko fluid model. The shear stress for this model is given by

$$\tau_{yx} = \eta_{app}\left(\frac{\partial u}{\partial y} + \frac{\partial v}{\partial x}\right), \tag{2.9}$$

where

$$\eta_{app} = a + b\left|2\left(\frac{\partial u}{\partial x}\right)^2 + 2\left(\frac{\partial v}{\partial y}\right)^2 + \left(\frac{\partial u}{\partial y} + \frac{\partial v}{\partial x}\right)^2\right|^{\frac{n-1}{2}}, \tag{2.10}$$

where a, b and n are the material constants.

The Sisko fluid model is of much importance due to its adequate description of a few non-Newtonian fluids over the most important range of shear rates. The extra stress

tensor $\mathbf{S}$ for an incompressible fluid obeys the Sisko rheological model can be expressed as [6-14]

$$\mathbf{S}=\left[a+b\left|\sqrt{\frac{1}{2}tr\ (\mathbf{A}_1^2)}\right|^{n-1}\right]\mathbf{A}_1, \tag{2.11}$$

where $\mathbf{A_1}$ is the rate of deformation tensor or the first Rivlin-Erickson tensor with a the dynamic viscosity, b the Sisko fluid parameter or the flow consistency index, $(n\geq 0)$ the power-law index or the flow behavior index (a non-negative real number).

The quantity

$$\eta_{app}=\left[a+b\left|\sqrt{\frac{1}{2}tr(\mathbf{A}_1^2)}\right|^{n-1}\right], \tag{2.12}$$

represents an apparent or effective viscosity as a function of the shear rate. If $a=0$ and $n=1$ (or $b=0$) the equations for Newtonian fluid, $a=0$ for the power-law model and $n=0$ with b as yield stress for the Bingham plastic model are obtained.

2.5 Approximations of Governing Equations

In this section we describe various approximations used in the governing equations.

2.5.1 Boussinesq Approximation

The Boussinesq approximation is employed when convective motions originating from buoyancy forces are considered. While using the approximation it is assumed that the temperature differences in a flow are small and pressure in free motion of the fluid does not exert a significant influence on density. The temperature changes are insufficient to cause the various properties of medium to vary significantly. By virtue of Boussinesq

approximation the density difference is taken as $g\Delta\rho \approx \rho g\beta\Delta T$, with $\beta = -\frac{1}{\rho}\left(\frac{\partial\rho}{\partial T}\right)_P$ is the coefficient of thermal expansion at constant pressure.

2.5.2 Boundary Layer Approximation

The concept of the boundary layer is one of the cornerstones in fluid mechanics. In this section we shall simplify the equations of motion for Sisko fluid within the boundary layer. Thin boundary layer exists next to solid walls if the Reynolds number is sufficiently high.

For a steady two-dimensional flow, the velocity and stress fields have the form

$$\mathbf{V} = \left[u(x,y), v(x,y), 0\right], \quad \mathbf{S} = \mathbf{S}(x,y), \tag{2.13}$$

where u and v are the x- and y-components of the velocity vector.

In view of Eqs. (2.3) and (2.13), ignoring the body forces, one has

$$\rho\left(u\frac{\partial u}{\partial x} + v\frac{\partial u}{\partial y}\right) = -\frac{\partial p}{\partial x} + \frac{\partial\left(s_{xx}\right)}{\partial x} + \frac{\partial\left(s_{xy}\right)}{\partial y}, \tag{2.14}$$

$$\rho\left(u\frac{\partial v}{\partial x} + v\frac{\partial v}{\partial y}\right) = -\frac{\partial p}{\partial y} + \frac{\partial\left(s_{yx}\right)}{\partial x} + \frac{\partial\left(s_{yy}\right)}{\partial y}, \tag{2.15}$$

where s_{xx}, s_{xy}, s_{yx} and s_{yy} are the components of extra stress tensor $\mathbf{S}$.

Now, substituting Eq. (2.13) into Eq. (2.11) we obtain

$$\left.\begin{aligned} s_{xx} &= \left(a + b\left|\frac{1}{2}tr\mathbf{A}_1^2\right|^{\frac{n-1}{2}}\right)\left(2\frac{\partial u}{\partial x}\right),\ s_{yy} = \left(a + b\left|\frac{1}{2}tr\mathbf{A}_1^2\right|^{\frac{n-1}{2}}\right)\left(2\frac{\partial v}{\partial y}\right), \\ s_{yx} &= s_{xy} = \left(a + b\left|\frac{1}{2}tr\mathbf{A}_1^2\right|^{\frac{n-1}{2}}\right)\left(\frac{\partial u}{\partial y} + \frac{\partial v}{\partial x}\right), \end{aligned}\right\} \tag{2.16}$$

where

$$J = \left|\frac{1}{2} tr\mathbf{A}_1^2\right|^{\frac{n-1}{2}} = \left|2\left(\frac{\partial u}{\partial x}\right)^2 + 2\left(\frac{\partial v}{\partial y}\right)^2 + \left(\frac{\partial u}{\partial y} + \frac{\partial v}{\partial x}\right)^2\right|^{\frac{n-1}{2}}. \tag{2.17}$$

Employing Eq. (2.16), momentum equations (2.14) and (2.15), for steady, two-dimensional flow of an incompressible Sisko fluid are written as follows:

$$\rho\left(u\frac{\partial u}{\partial x} + v\frac{\partial u}{\partial y}\right) = -\frac{\partial p}{\partial x} + a\left(\frac{\partial^2 u}{\partial x^2} + \frac{\partial^2 u}{\partial y^2}\right) + 2b\frac{\partial}{\partial x}\left[\frac{\partial u}{\partial x}J\right] + b\frac{\partial}{\partial y}\left[\left(\frac{\partial u}{\partial y} + \frac{\partial v}{\partial x}\right)J\right], \tag{2.18}$$

$$\rho\left(u\frac{\partial v}{\partial x} + v\frac{\partial v}{\partial y}\right) = -\frac{\partial p}{\partial y} + a\left(\frac{\partial^2 v}{\partial x^2} + \frac{\partial^2 v}{\partial y^2}\right) + b\frac{\partial}{\partial x}\left[\left(\frac{\partial u}{\partial y} + \frac{\partial v}{\partial x}\right)J\right] + 2b\frac{\partial}{\partial y}\left[\left(\frac{\partial v}{\partial y}\right)J\right]. \tag{2.19}$$

To facilitate the boundary layer approximation, the length and velocity scales for the boundary layer analysis are chosen as L and U, then the non-dimensional variables could be:`

$$\tilde{u} = \frac{u}{U},\ \tilde{v} = \frac{v}{U},\ \tilde{x} = \frac{x}{L},\ \tilde{y} = \frac{y}{L},\ \text{and}\ \tilde{p} = \frac{p}{\rho U^2}. \tag{2.20}$$

With the help of non-dimensionalization, given by Eq. (2.20), the momentum equations for a non-Newtonian Sisko fluid given as Eqs. (2.18) and (2.19) can be transformed as follows:

$$\tilde{u}\frac{\partial \tilde{u}}{\partial \tilde{x}} + \tilde{v}\frac{\partial \tilde{u}}{\partial \tilde{y}} = -\frac{\partial \tilde{p}}{\partial \tilde{x}} + \frac{a/\rho}{UL}\frac{\partial^2 \tilde{u}}{\partial \tilde{x}^2} + \frac{a/\rho}{UL}\frac{\partial^2 \tilde{u}}{\partial \tilde{y}^2}$$

$$+2\frac{b/\rho}{U^{2-n}L^n}\left(\frac{L}{\delta}\right)^{n+1}\frac{1}{(L/\delta)^2}\frac{\partial}{\partial \tilde{x}}\left[\left(\frac{\partial \tilde{u}}{\partial \tilde{x}}\right)\tilde{J}\right] + \frac{b/\rho}{U^{2-n}L^n}\left(\frac{L}{\delta}\right)^{n+1}\frac{1}{(L/\delta)^2}\frac{\partial}{\partial \tilde{y}}\left[\left(\frac{\partial \tilde{u}}{\partial \tilde{y}} + \frac{\partial \tilde{v}}{\partial \tilde{x}}\right)\tilde{J}\right], \tag{2.21}$$

$$\frac{1}{(L/\delta)^2}\left(\tilde{u}\frac{\partial \tilde{v}}{\partial \tilde{x}} + \tilde{v}\frac{\partial \tilde{v}}{\partial \tilde{y}}\right) = -\frac{\partial \tilde{p}}{\partial \tilde{y}} + \frac{1}{(L/\delta)^2}\left(\frac{a/\rho}{UL}\frac{\partial^2 \tilde{v}}{\partial \tilde{x}^2} + \frac{a/\rho}{UL}\frac{\partial^2 \tilde{v}}{\partial \tilde{y}^2}\right)$$

$$+\frac{1}{(L/\delta)^2}\left[\frac{b/\rho}{U^{2-n}L^n}\left(\frac{L}{\delta}\right)^{n+1}\frac{\partial}{\partial \tilde{x}}\left[\left(\frac{1}{(L/\delta)^2}\frac{\partial \tilde{v}}{\partial \tilde{x}}\right)\tilde{J}\right]\right]$$

$$+\frac{1}{(L/\delta)^2}\frac{b/\rho}{U^{2-n}L^n}\left(\frac{L}{\delta}\right)^{n+1}\frac{\partial}{\partial\tilde{y}}\left[\left(\frac{1}{(L/\delta)^2}\frac{\partial v}{\partial\tilde{y}}\right)\tilde{J}\right], \tag{2.22}$$

$$\tilde{J}=\left(\frac{U}{\delta}\right)^{n-1}\left|\frac{1}{(L/\delta)^2}\left[\left(\frac{\partial\tilde{u}}{\partial\tilde{y}}\right)^2+\left(\frac{\partial\tilde{v}}{\partial\tilde{x}}\right)^2+\left(\frac{\partial\tilde{u}}{\partial\tilde{x}}\right)^2+\left(\frac{\partial\tilde{v}}{\partial\tilde{y}}\right)^2+2\frac{\partial\tilde{u}}{\partial\tilde{y}}\frac{\partial\tilde{v}}{\partial\tilde{x}}\right]\right.$$

$$\left.+\frac{1}{(L/\delta)^2}\left[\left(\frac{\partial\tilde{u}}{\partial\tilde{x}}\right)^2+\left(\frac{\partial\tilde{v}}{\partial\tilde{y}}\right)^2\right]\right|. \tag{2.23}$$

Within the boundary layer, the inertial and viscous terms are of the same order of magnitude, gives us

$$\frac{a/\rho}{LU}\left(\frac{L}{\delta}\right)^2\sim 1,\ \left(\frac{\delta}{L}\right)^2\sim\left(\frac{1}{\mathrm{Re}_a}\right)\text{ and }\frac{b/\rho}{L^nU^{2-n}}\left(\frac{L}{\delta}\right)^{n+1}\sim 1, \tag{2.24}$$

where $\mathrm{Re}_a=\dfrac{LU}{a/\rho}$.

In the limit $\mathrm{Re}_a\to\infty$, Eqs. (2.21) to (2.23) asymptotically become

$$\tilde{u}\frac{\partial\tilde{u}}{\partial\tilde{x}}+\tilde{v}\frac{\partial\tilde{u}}{\partial\tilde{y}}=-\frac{\partial\tilde{p}}{\partial\tilde{x}}+\frac{\partial^2\tilde{u}}{\partial\tilde{y}^2}+\frac{\partial}{\partial\tilde{y}}\left(\frac{\partial\tilde{u}}{\partial\tilde{y}}\left|\frac{\partial\tilde{u}}{\partial\tilde{y}}\right|^{n-1}\right), \tag{2.25}$$

$$0=-\frac{\partial\tilde{p}}{\partial\tilde{y}}. \tag{2.26}$$

Thus, Eqs. (2.25) and (2.26) in dimensional form simplify to

$$u\frac{\partial u}{\partial x}+v\frac{\partial u}{\partial y}=-\frac{\partial p}{\partial x}+a\frac{\partial^2 u}{\partial y^2}+b\frac{\partial}{\partial y}\left(\frac{\partial u}{\partial y}\left|\frac{\partial u}{\partial y}\right|^{n-1}\right), \tag{2.27}$$

$$0=-\frac{\partial p}{\partial y}. \tag{2.28}$$

2.6 Some Dimensionless Numbers

2.6.1 Reynolds number *Re*

The Reynolds number, the most familiar dimensionless number in fluid mechanics can be written as

$$\mathrm{Re} = \frac{UL}{\nu}, \tag{2.29}$$

where ρ is the density of fluid, U fluid velocity, L the characteristic length, ν the kinemetic viscosity of fluid. It is a measure of ratio of the magnitude of inertial force in the flow to the viscous forces in the flow. It characterizes the nature of flow (laminar, transitional or turbulent).

2.6.2 Rotational Reynolds number Re_{rot}

The Reynolds number for rotating fluid can be expressed as [67]

$$\mathrm{Re}_{rot} = \frac{\Omega L^2}{\nu}, \tag{2.30}$$

where Ω is the angular frequency of rotating fluids and rest of the symbols are as defined above.

2.6.3 Eckert Number *Ec*

It expresses the ratio of Kinetic energy to the thermal energy change [67]

$$Ec = \frac{U_\infty^2}{c_p \Delta T}, \tag{2.31}$$

where U_∞ is the velocity fluid far from surface, c_p the specific heat capacity of fluid, and ΔT the temperature difference.

2.6.4 Grashof Number *Gr*

The Grashof number approximates the ratio of the buoyancy to viscous force acting on a fluid. It is used in heat transfer involving natural convection and can be expressed as

$$Gr = \frac{g\beta\left(T_w - T_\infty\right)L^3}{\nu^2}, \tag{2.32}$$

where g is the acceleration due to gravity, β the volume thermal expansion coefficient, T_w the temperature of the wall, T_∞ the temperature far away from the wall, L the characteristic length, and ν the kinematic viscosity of fluid.

2.6.5 Mixed Convection Parameter λ

It measures the ratio of the buoyancy force to the inertial force and given by expression

$$\lambda = \frac{Gr}{\mathrm{Re}^2}, \tag{2.33}$$

where Gr and Re are the Grashof and Reynolds numbers, respectively. When $\lambda >> 1$ the bouyancy forces dominate the inertial forces, then there will be natural convective heat transfer. On the contrary, when $\lambda << 1$ the inertial forces dominates the buoyant forces , the heat transfer will be of forced convection type. However, $\lambda \to 1$ represents the mix convective heat transfer.

2.6.6 Nusselt Number *Nu*

It expresses the ratio of the total heat transfer in a system to the heat transfer by conduction. It can be defined mathematically by

$$Nu = \frac{hL}{\kappa}, \tag{2.34}$$

where h is the heat transfer coefficient, L the characteristic length, and κ the thermal conductivity.

2.6.7 Prandtl Number *Pr*

This number depicts the ratio of momentum diffusivity to the thermal diffusivity. It characterizes the physical property of a fluid. It can be expressed as

$$\mathrm{Pr} = \frac{\nu}{\alpha}, \tag{2.35}$$

where ν is the kinematic viscosity of fluid and α the thermal diffusivity of fluid.

2.6.8 Skin Friction Coefficient C_f

It expresses the dynamic friction resistance originating in viscous fluid flow around a fixed wall and is given by [67]

$$C_f = \frac{\tau_w}{1/2\,\rho U_w^2}, \tag{2.36}$$

where τ_w is the shear stress on the wall, ρ the fluid density and U_w stretching velocity of the wall.

Chapter 3

Forced Convective Heat Transfer in Boundary Layer Flow of Sisko Fluid over a Nonlinear Stretching Sheet

In this chapter the major focus is to analyze the forced convective heat transfer in the steady boundary layer flow of Sisko fluid over a nonlinear stretching sheet. The prescribed surface temperature (PST case) and prescribed heat flux (PHF case) are applied at the surface bounding the flowing fluid. A wider range of the rheological parameter and the power-law index has been focused spanning from highly shear thinning to shear thickening Sisko fluids to investigate the flow and heat transfer characteristics. The governing partial differential equations are reduced to a system of nonlinear ordinary differential equations by using appropriate transformation and solved numerically. The numerical results are obtained by the shooting method using adaptive Runge Kutta method with Broyden's method in the domain $[0,\infty)$. Additionally, exact solutions are obtained in some particular cases. The effect of the pertinent parameters (stretching parameter, wall temperature parameter, material parameter of the Sisko fluid and Prandtl number) on temperature field are explored in depth. In addition, the local Nusselt number versus wall temperature parameter is also graphed and tabulated for different values of pertaining parameters. Further, numerical results are validated by comparison with exact solutions as well as previously published results in the literature.

3.1 Governing Equations

This section comprises the governing equations and the rheological model for the steady two-dimensional flow and heat transfer of incompressible and inelastic fluid Sisko fluid in the Cartesian coordinates. To derive such governing equations we make use of the following laws of conservations of mass, linear momentum and energy:

$$\nabla \cdot \mathbf{V} = 0, \tag{3.1}$$

$$\rho(\mathbf{V} \cdot \nabla)\mathbf{V} = -\nabla \mathrm{p} + \nabla \cdot \mathbf{S} + \rho\mathbf{B}, \tag{3.2}$$

$$\rho c_p(\mathbf{V} \cdot \nabla)T = -\nabla \cdot \mathbf{q} + \mathbf{S} \cdot \mathbf{L} + \rho\mathbf{r}. \tag{3.3}$$

In the above equations $\mathbf{V}$ is the velocity vector, ρ the density of the fluid, c_p the specific heat at constant pressure, $\mathbf{B}$ the body force per unit mass, $\mathbf{r}$ the possible heat source or sink per unit mass, p the pressure, T the temperature, $\mathbf{S}$ the extra stress tensor, and $\mathbf{q}$ the heat flux given by

$$\mathbf{q} = -\kappa(\nabla T), \tag{3.4}$$

where κ is the thermal conductivity of the fluid and ∇ the gradient operator.

The extra stress tensor $\mathbf{S}$ for an incompressible fluid obeys the Sisko rheological model. This model mathematically can be expressed as [6-14]

$$\mathbf{S} = \left[a + b\left| \sqrt{\frac{1}{2} tr\ (\mathbf{A}_1^2)} \right|^{n-1} \right] \mathbf{A}_1, \tag{3.5}$$

where $\mathbf{A}_1$ is the rate of deformation tensor or the first Rivlin-Erickson tensor defined as

$$\mathbf{A}_1 = \mathbf{L} + \mathbf{L}^{\mathsf{T}},\ \mathbf{L} = \nabla \mathbf{V}, \tag{3.6}$$

with a the dynamic viscosity, b the Sisko fluid parameter or the flow consistency index, n the power-law index or the flow behavior index (a non-negative real number) and T stands for transpose.

The quantity

$$\mu_{eff} = \left[a + b \left| \sqrt{\frac{1}{2} tr(\mathbf{A}_1^2)} \right|^{n-1} \right], \tag{3.7}$$

represents an apparent or effective viscosity as a function of the shear rate. If $a = 0$ and $n = 1$ or $b = 0$ the equations for Newtonian fluid, $a = 0$ for the power-law model and $n = 0$ with b as yield stress for Bingham plastic model are obtained.

For the steady two-dimensional flow, we assume the velocity, temperature and stress fields of the form

$$\mathbf{V} = \left[u(x,y), v(x,y), 0 \right], \; T = T(x,y), \; \mathbf{S} = \mathbf{S}(x,y), \tag{3.8}$$

when (x, y) denotes the Cartesian coordinates along the sheet and vertical to it, u and v the velocity components in the x - and y - directions, respectively.

The steady two-dimensional, incompressible equations of motion (3.2) including conservation of mass (3.1) and thermal energy (3.3), ignoring the viscous dissipation and source terms can be written as

$$\frac{\partial u}{\partial x} + \frac{\partial v}{\partial y} = 0, \tag{3.9}$$

$$\rho \left(u \frac{\partial u}{\partial x} + v \frac{\partial u}{\partial y} \right) = -\frac{\partial p}{\partial x} + \frac{\partial s_{xx}}{\partial x} + \frac{\partial s_{xy}}{\partial y}, \tag{3.10}$$

$$\rho\left(u\frac{\partial v}{\partial x}+v\frac{\partial v}{\partial y}\right)=-\frac{\partial p}{\partial y}+\frac{\partial s_{yx}}{\partial x}+\frac{\partial s_{yy}}{\partial y}, \tag{3.11}$$

$$\rho c_p\left(u\frac{\partial T}{\partial x}+v\frac{\partial T}{\partial y}\right)=\kappa\left(\frac{\partial^2 T}{\partial x^2}+\frac{\partial^2 T}{\partial y^2}\right). \tag{3.12}$$

In view of Eq. (3.8), the stress components are inserted into the equations of motion and the usual boundary layer approximations are made, the equations of motion and energy characterizing the steady boundary layer flow take the form (cf. Chapter 2)

$$\rho\left(u\frac{\partial u}{\partial x}+v\frac{\partial u}{\partial y}\right)=-\frac{\partial p}{\partial x}+a\frac{\partial^2 u}{\partial y^2}+b\frac{\partial}{\partial y}\left(\left|\frac{\partial u}{\partial y}\right|^{n-1}\frac{\partial u}{\partial y}\right), \tag{3.13}$$

$$0=-\frac{\partial p}{\partial y}, \tag{3.14}$$

$$u\frac{\partial T}{\partial x}+v\frac{\partial T}{\partial y}=\frac{\kappa}{\rho c_p}\frac{\partial^2 T}{\partial y^2}, \tag{3.15}$$

3.2 Geometry of the Problem

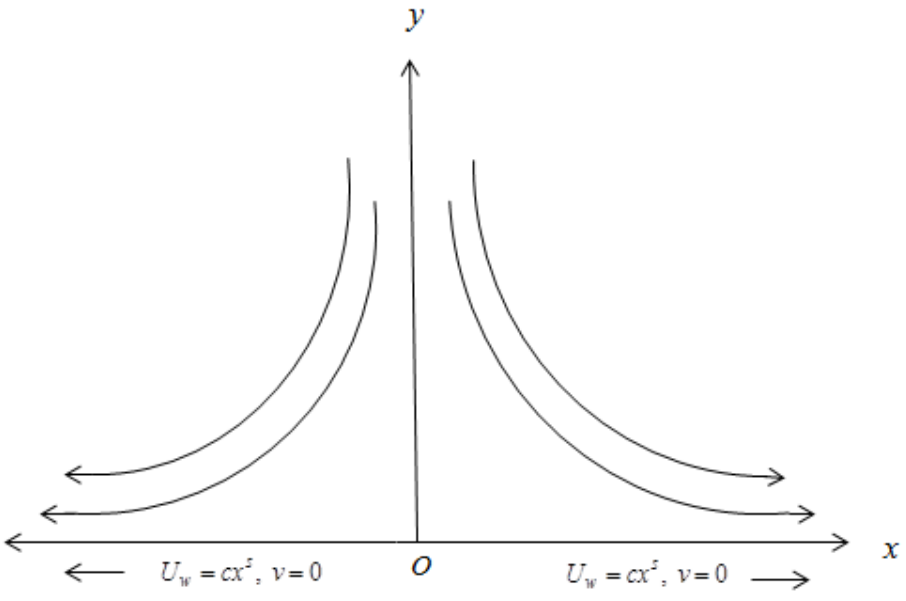

***Figure 3.1**:* Flow geometry and coordinate system.

3.3 Formulation of the Problem

3.3.1 Flow Analysis

We consider the steady, laminar and two-dimensional boundary layer flow of an incompressible viscous homogeneous non-Newtonian fluid obeying Sisko fluid model over a long continuous stretching sheet coinciding with the plane $y=0$ and the flow is confined to the region $y>0$ (shown in figure 3.1). Flow is induced due to the stretching of sheet in x- direction, while origin is fixed with velocity $U_w = cx^s$, where c and s are positive real numbers relating to stretching of the sheet. Further, it is assumed that the sheet is subjected to either prescribed surface temperature (*PST* case) or prescribed heat flux (*PHF* case). Note that if the streamwise velocity component u increases with the distance from the moving boundary then the velocity gradient and therefor the shear rate are positive. However, if u decreases with increasing y then the velocity gradient and therefore shear rate are negative. In the present problem, within the boundary layer the shear rate $\left(\frac{\partial u}{\partial y}\right)$ is assumed to be negative since the streamwise velocity component u decreases monotonically with increasing y from the moving boundary. (for more details see [68]). Thus, under the above assumptions, the momentum equation characterizing the steady boundary layer flow takes the form

$$\rho\left(u\frac{\partial u}{\partial x}+v\frac{\partial u}{\partial y}\right)=a\frac{\partial^2 u}{\partial y^2}-b\frac{\partial}{\partial y}\left(-\frac{\partial u}{\partial y}\right)^n. \tag{3.16}$$

The flow is subject to the boundary conditions

$$u=U_w=cx^s,\ v=0 \text{ at } y=0, \tag{3.17}$$

$$u\to 0 \text{ as } y\to\infty. \tag{3.18}$$

In view of the transformation variable [24]

$$\eta = \frac{y}{x}\mathrm{Re}_b^{\frac{1}{n+1}} \text{ and } \psi(x,y) = xU\,\mathrm{Re}_b^{\frac{-1}{n+1}} f(\eta), \tag{3.19}$$

and after mathematical simplification, we obtain the following problem

$$Af''' + n\left[-f''\right]^{n-1} f''' + \left(\frac{s(2n-1)+1}{n+1}\right) ff'' - s(f')^2 = 0, \tag{3.20}$$

$$f(0) = 0, \quad f'(0) = 1 \text{ and } f'(\eta) \to 0 \text{ as } \eta \to 0, \tag{3.21}$$

where prime denotes the differentiation with respect to η and the dimensionless quantities are defined by

$$\mathrm{Re}_a = \rho xU / a,\ \mathrm{Re}_b = \rho x^n U^{2-n} / b \text{ and } A = \mathrm{Re}_b^{\frac{2}{n+1}} / \mathrm{Re}_a. \tag{3.22}$$

The physical quantity of major interest is the local skin friction coefficient which arises from the friction of the fluid against the "skin" of the object over which the fluid is flowing. It is defined by

$$C_f = \frac{\tau_w\big|_{y=0}}{\frac{1}{2}\rho U_w^2}, \tag{3.23}$$

where $\tau_w = \left(a + b\left|\frac{\partial u}{\partial y}\right|^{n-1}\right)\frac{\partial u}{\partial y}$ is the shear stress at the wall.

In view of Eq. (3.19), the local skin friction coefficient reduces to

$$\frac{1}{2}\mathrm{Re}_b^{\frac{1}{n+1}} C_f = Af''(0) - \left[-f''(0)\right]^n. \tag{3.24}$$

Remark. From Eq. (3.20), it is noticed that the global similarity solutions for the problem only exists only for the case $s = 1/3$, for all the values of power law index *n*, otherwise the solutions are locally similar.

3.3.2 Heat Transfer Analysis

By using the usual thermal boundary layer approximations, neglecting viscous dissipation and heat generation, the thermal energy equation is given by

$$u\frac{\partial T}{\partial x}+v\frac{\partial T}{\partial y}=\frac{\kappa}{\rho c_p}\frac{\partial^2 T}{\partial y^2}, \tag{3.25}$$

where c_p is the specific heat of the fluid at constant pressure and κ the thermal conductivity.

Two types of thermal boundary conditions are considered in heat transfer analysis, and they are treated separately in the following sections.

Prescribed Surface Temperature (PST case)

In this case, the thermal boundary conditions are

$$T=T_w\left(=T_\infty+B\left(\frac{x}{L}\right)^m\right), \tag{3.26}$$

$$T\to T_\infty \text{ as } y\to\infty, \tag{3.27}$$

where B is a constant, L the characteristic length, T_∞ the constant fluid temperature far away from the sheet, T_w the wall temperature and m the wall temperature parameter.

Defining the non-dimensional temperature $\theta(\eta)$ by

$$\theta(\eta)=\frac{T-T_\infty}{T_w-T_\infty}, \tag{3.28}$$

and using Eqs. (3.19), (3.26) and (3.27), Eq. (3.25) takes the form

$$\theta''+\Pr\left(\frac{s(2n-1)+1}{n+1}f\theta'-mf'\theta\right)=0, \tag{3.29}$$

where $\Pr = \frac{xUR_b^{\frac{-2}{n+1}}}{\alpha}$ is the generalized Prandtl number.

The boundary conditions for $\theta(\eta)$ follow from Eqs. (3.26) and (3.27) are

$$\theta(0) = 1 \text{ and } \theta(\eta) \to 0 \text{ as } \eta \to \infty. \tag{3.30}$$

The rate of heat transfer at the sheet surface is

$$q_w\big|_{y=0} = -\kappa(T_w - T_\infty)\theta'(0)\frac{1}{x}R_b^{1/n+1}, \tag{3.31}$$

which on simplification reduces to

$$\mathrm{Re}_b^{-1/n+1} Nu_x = -\theta'(0), \tag{3.32}$$

where $Nu_x = \frac{xq_w}{k(T_w - T_\infty)}$ is the local Nusselt number.

Prescribed Heat Flux (PHF case)

In PHF case, the dimensionless temperature $g(\eta)$ is defined as

$$g(\eta) = \frac{T - T_\infty}{(D/\kappa)(x/L)^m xR_b^{-1/n+1}}, \tag{3.33}$$

with the following boundary conditions

$$q_w = -\kappa\left(\frac{\partial T}{\partial y}\right)_{y=0} = D\left(\frac{x}{L}\right)^m, \tag{3.34}$$

$$T \to T_\infty \text{ as } y \to \infty, \tag{3.35}$$

where D is a constant and $m = 0$ leads to a constant heat flux case.

Using Eqs. (3.19) and (3.33) in Eq. (3.25) one finds that

$$g'' + \Pr\left(\frac{s(2n-1)+1}{n+1} fg' + \frac{s(2-n)+n}{n+1} f'g - (m+1) f'g\right) = 0, \tag{3.36}$$

$$g'(0) = -1 \text{ and } g(\eta) \to 0 \text{ as } \eta \to \infty. \tag{3.37}$$

The local heat transfer coefficient is

$$h = \frac{q_w}{T_w - T_\infty} = \frac{\kappa}{g(0) x R_b^{1/n+1}}, \tag{3.38}$$

resulting in the local Nusselt number given by

$$R_b^{\frac{-1}{n+1}} Nu_x = \frac{1}{g(0)}, \tag{3.39}$$

with $Nu_x = \frac{hx}{k}$ as the local Nusselt Number.

3.4 Exact Solutions for Particular Cases

Since Eq. (3.20) has simple exact solution to a special case, namely $n = s = 1$ (see Ref. [24] for detail). For this case with $m = 0,$ Eq. (3.29) reduces to

$$\theta'' + \Pr f\theta' = 0. \tag{3.40}$$

The exact solution of Eq. (3.40) in terms of the incomplete Gamma function, satisfying boundary conditions (3.30) is

$$\theta(\eta) = \frac{\Gamma(\frac{\Pr}{\beta^2}, 0) - \Gamma(\frac{\Pr}{\beta^2}, \frac{\Pr}{\beta^2} e^{-\alpha\eta})}{\Gamma(\frac{\Pr}{\beta^2}, 0) - \Gamma(\frac{\Pr}{\beta^2}, \frac{\Pr}{\beta^2})}, \tag{3.41}$$

where $\beta = \frac{1}{\sqrt{1+A}}$ and $\Gamma(\cdot)$ the incomplete Gamma function.

For $n = s = 1$ and $A = 0,$ Eq. (3.29) reduces to

$$\theta'' + \Pr(f\theta' - mf'\theta) = 0. \tag{3.42}$$

The exact solution of the above equation satisfying the boundary conditions (3.30) in terms of Kummer's function is expressed as [69]

$$\theta(\eta) = e^{-\Pr\eta}\frac{M\left[\Pr - m, \Pr + 1, -\Pr e^{-\eta}\right]}{M\left[\Pr - m, \Pr + 1, -\Pr\right]}, \tag{3.43}$$

where $M(\cdot)$ is the Kummer's function.

When $n = s = 1$ and $A = 0,$ Eq. (3.36) has exact solution satisfying boundary conditions (3.37) of form [69]

$$g(\eta) = \frac{1}{\Pr}e^{-\Pr\eta}\frac{M\left[\Pr - m, \Pr + 1, -\Pr e^{-\eta}\right]}{M\left[\Pr - m, \Pr + 1, -\Pr\right]}. \tag{3.44}$$

3.5 Solution Methodology

In general it is very difficult to find the exact analytical solution of non-linear two point boundary value problems (3.20), (3.29) and (3.36) along with boundary conditions (3.21), (3.30) and (3.37). Therefore, these problems are solved numerically by the shooting technique. The equations are firstly written as a system of first order ordinary differential equations as:

$$f' = p, \tag{3.45}$$

$$p' = q, \tag{3.46}$$

$$q' = \frac{sp^2 - \frac{s(2n-1)+1}{n+1}fq}{A + n(-q)^{n-1}}, \tag{3.47}$$

with flow boundary conditions

$$f(0) = 0 \text{ and } p(0) = 1. \tag{3.48}$$

For prescribed surface temperature

$$\theta' = t, \tag{3.49}$$

$$t' = -\Pr\left[\frac{s(2n-1)+1}{n+1}ft - mp\theta\right], \tag{3.50}$$

with thermal boundary condition

$$\theta(0) = 1. \tag{3.51}$$

And for prescribed heat flux

$$g' = h, \tag{3.52}$$

$$h' = -\Pr\left[\frac{s(2n-1)+1}{n+1} fh + \frac{s(2-n)+n}{n+1} pg - (m+1)pg\right], \tag{3.53}$$

with thermal boundary condition

$$h(0) = -1. \tag{3.54}$$

Then the corresponding initial value problems are solved by the adaptive Runge-Kutta method. The initially guessed values $f''(0)$ and $\theta'(0)$ are refined iteratively using the Boryden's method to satisfy boundary condition at infinity. The iterative process is terminated when the absolute error is less than the tolerance 10^{-5}.

3.6 Validation of the Results

Before ensuing the detailed presentation and discussion of new results obtained in this study it is worthy to validate the reliability of the present numerical results by comparing them with the exact results obtained for some limiting case of the problem. Figures 3.2 to 3.4 compare these results for PST and PHF cases, and an excellent agreement confirms the credibility of our numerical results. Also, in table 3.1, a comparison with the results of Chen [21] is made and an excellent agreement is found. This comparison lends the support to the credibility of the numerical solution methodology employed herein.

3.7 Numerical Results and Discussion

The main aim of the present study is to investigate the heat transfer to a Sisko fluid over a nonlinear stretching sheet with the non-isothermal wall and variable heat flux boundary

conditions. In order to comprehend the heat transfer phenomena in detail, Eqs. (3.29) and (3.36) with their respective boundary conditions are solved numerically and the results are displayed through graphs. Mainly, the effects of the power-law index n, stretching parameter s, Prandtl number $\Pr$, material parameter A, and surface temperature parameter m are investigated in detail, both for PST and PHF cases. Moreover, the heat transfer aspects are explored in terms of the local Nusselt number at the wall. Figures 3.5 to 3.15 give the various perspectives of heat transfer for both PST and PHF cases. The values of the local Nusselt number are recorded in tables 3.2 and 3.3 for both PST and PHF cases, respectively.

The effect of the power-law index n on temperature profile $\theta(\eta)$ is presented in figures 3.5 and 3.6 for both PST and PHF cases, respectively. A wider range of the power law index n is spanned in the analysis $(0.2 \le n \le 1.9)$ covering from highly shear thinning to thickening fluids. Most polymeric melts and solutions have value of the power law index n in the range 0.3-0.7 [70]. Moreover, typical starch-in-water and corn flour-in-water dispersion have values of the power-law index n in the range 1.4-1.6 [71]. The figure 3.5(a) shows that the temperature profile increases when the power-law index n is decremented below one. The increase is large for smaller values of n. This increase can be attributed to the fact that the reduction in viscosity favors the heat transfer. The temperature profile also decreases as the value of n is incremented gradually (figure 3.5(b)) for $n > 1$. A comparison of the two patterns reveals a strong dependence of heat transfer on flow behavior index for $n < 1$ and weaker when $n > 1$. Figures 3.6(a,b) elucidate the temperature profiles for the PHF case for $n < 1$ and $n > 1$, respectively. It is quite clear from these figures that the temperature profiles decrease when the value of the power-law index is increased for shear thinning $(n < 1)$ and shear thickening $(n > 1)$

regimes. These figures show that, in the PHF case, the qualitative behavior of temperature profile with change in n is similar to the PST case. However, a stronger dependence of the temperature profile can be noticed in the PHF case. Both these figures put in an evidence that an augmentation in the value of the power-law results in a decrease of the thermal boundary layer thickness.

The stretching parameter s affects the temperature profile and thermal boundary layer by virtue of imparting shear stress at the boundary. A broader range $1/3 \le s \le 2.0$ is included in the analysis, including $s = 1.0$ for linear stretching. Its effects on heat transfer for both boundary conditions are presented in figures 3.7 and 3.8, respectively. For the PST case, when the value of the power-law index $n < 1$, the effect of the stretching parameter *s* on heat transfer to the fluid is very meager; however, the thermal boundary layer thickness increases a bit as the value of *s* is incremented progressively. We can ascribe this increase to the amplification of shear stress with each increment in *s*. For shear thinning regime $(n < 1)$ the enhancement of shear stress lowers the effective viscosity that favors the heat transfer. Figure 3.7(b) presents the effect of the stretching parameter *s* on the temperature profile for $n = 1.5.$ The temperature and thermal boundary layer decrease and *s* affects the thermal boundary layer thickness substantially for this case. In this case the rise in shear stress increases the effective viscosity that in turn impedes the heat transfer. Figure 3.8(a) depicts that the temperature profile rises as the value of *s* is augmented for shear thinning ($n < 1$) regime. The temperature near the wall grows quite prominently as the value of s is incremented. For shear thickening $(n = 1.5)$ regime, the temperature profile and corresponding thermal boundary layer show a diminution as the value of *s* is raised (figure 3.8b).

The effect of the material parameter A on the temperature profile for nonlinear stretching is presented in figures 3.9 and 3.10, respectively, for PST and PHF cases. These figures also make a comparison amongst the temperature profiles of the Newtonian fluid $(A=0 \text{ and } n=1)$ and the power-law fluid $(A=0 \text{ and } n\neq 1)$ with those of the Sisko fluid $(A\neq 0)$. Figures 3.9(a,b) reveal that the temperature profile and corresponding thermal boundary layer thickness depress in each case with increasing value of the material parameter *A*. It is noticed that the increasing values of A increases the entrainment of cooler ambient fluid that lowers the temperature profile. It can also be noticed from the sketches that the effect of A on the thermal boundary layer is pronounced for low Prandtl number as compared to higher one. Figures 3.10(a,b) demonstrate that the temperature profile and corresponding thermal boundary layer thickness also decrease with an increase in the value of A for different values of the power-law index *n*. Effects are more prominent for lower Prandtl number.

The influence of the wall temperature parameter *m* for both PST and PHF cases on the temperature distribution and thermal boundary layer thickness is presented in figures 3.11 and 3.12, respectively. Numerical solutions are sought in the range $-0.5\leq m\leq 1.0$ and $0\leq m\leq 1.5$ for PST and PHF cases, respectively. From these figures, it is observed that as the value of *m* is incremented progressively from negative to positive, the temperature and thermal boundary layer thickness decrease as shown for some values of the power-law index *n*. But, this effect turn out to be diminish for larger values of *n*.

The Prandtl number $\Pr$ of a fluid plays a dominant role in forced convective heat transfer. The computations are carried out for large Prandtl number, many non-Newtonian fluids exhibit a value of Prandtl number as high as 100 or even greater [64,72]. Its effect for the PST case for different values of the power-law index *n* is shown

in figures 3.13(a,b). It is notified that the temperature profile decreases prominently by thinning the thermal boundary layer thickness when $\Pr$ is increased. The decrease can be ascribed to the enhanced momentum diffusivity for larger Prandtl number. The same qualitative aspects are observed for the PHF case as shown in figures 3.14(a,b).

Figure 3.15a depicts the variation of the local Nusselt number $\theta'(0)$ with change in wall temperature parameter *m* for PST case. It is clearly observed from the plots that the heat transfer at the wall increases rapidly for the fluids with greater Pr. Moreover, the fluids with $n>1$ carry larger heat out of heated surface. These plots also give the value of *m* where the value of $\theta'(0)$ approaches to zero. This value of *m* is strong function of the power-law index *n.* Figure 3.15b illustrates the effect of *m* on the local Nusselt number for the Sisko fluid (both for shear thinning and shear thickening regimes) for PHF case. The Prandtl number affects the heat transfer in same fashion as previous one, but here more heat is transferred for each value of *m* as compared to the PST case.

Table 3.2 briefly shows the trend in the local Nusselt number for shear thinning and thickening fluids when the material parameter A and stretching parameter *s* are varied for the PST case. It can be noticed from this table that the local Nusselt number shows a boost with an each increment of A. It is also clear that there is much rise in the local Nusselt number for flow behavior index $n>1$. Table 3.3 displays the same information and qualitatively similar trends are observed for the PHF case. Variation of local Nusselt number with material parameter for isothermal (special case) stretching sheet is shown in table 3.4. It will be used for comparison in a forthcoming chapter.

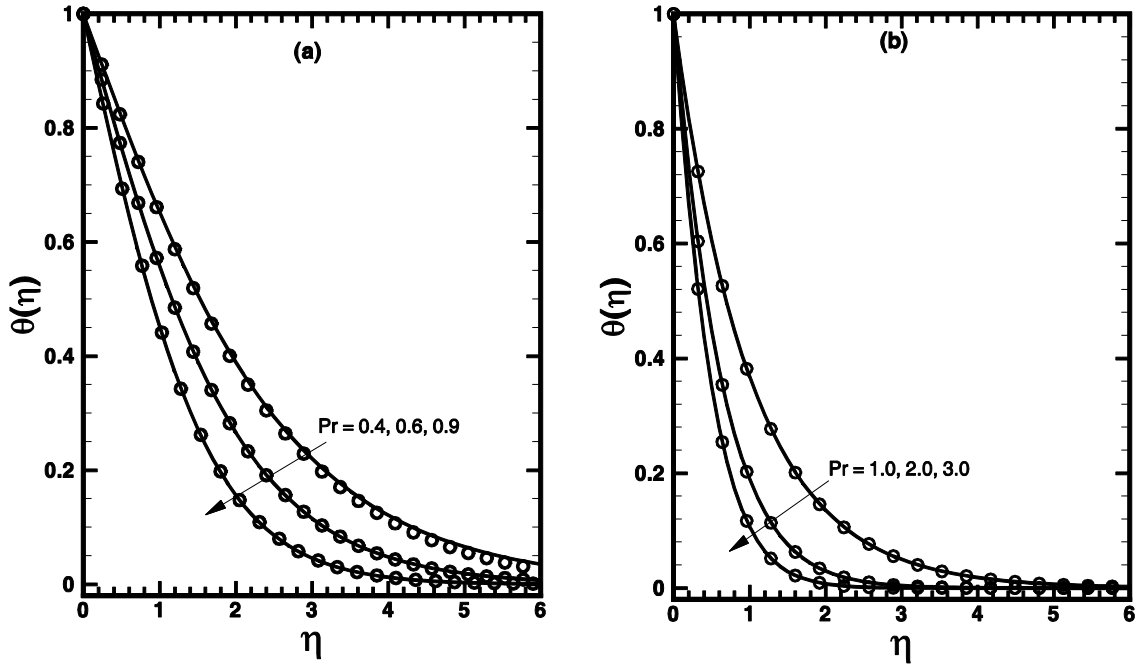

Figure 3.2: A comparison of the exact and numerical results (solid line numerical results and open circles exact results) in the PST case when $n = s = 1$ and $A = 1$ are fixed.

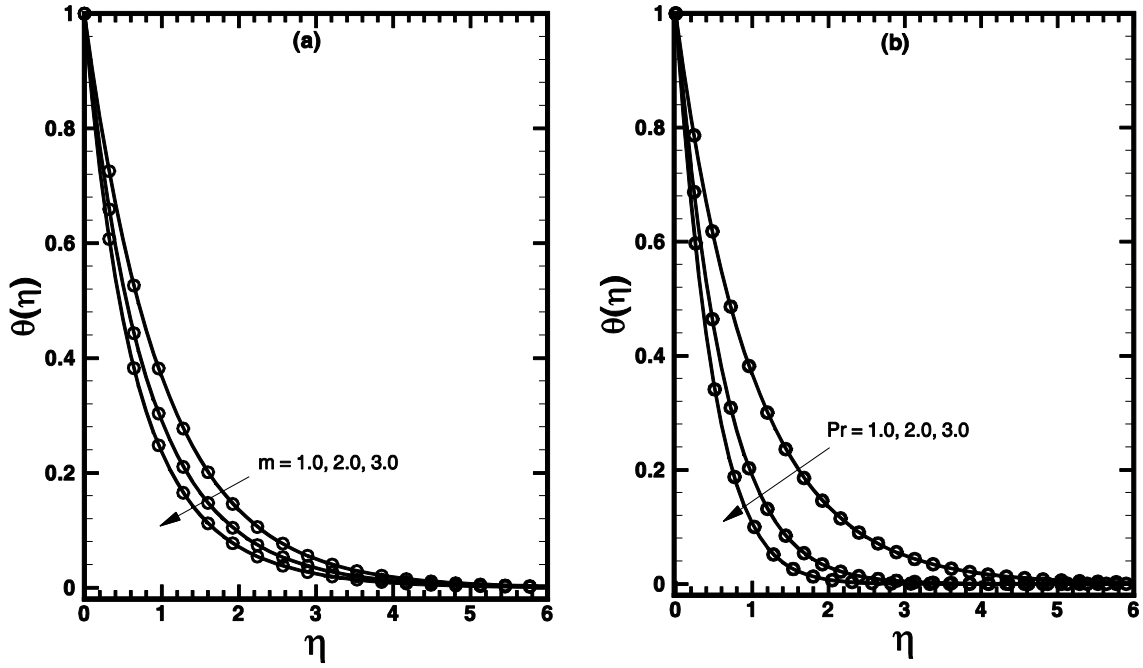

Figure 3.3: A comparison of the exact and numerical results (solid line numerical results and open circles exact results) in the PST when $n = s = 1$, and $A = 0$ are fixed.

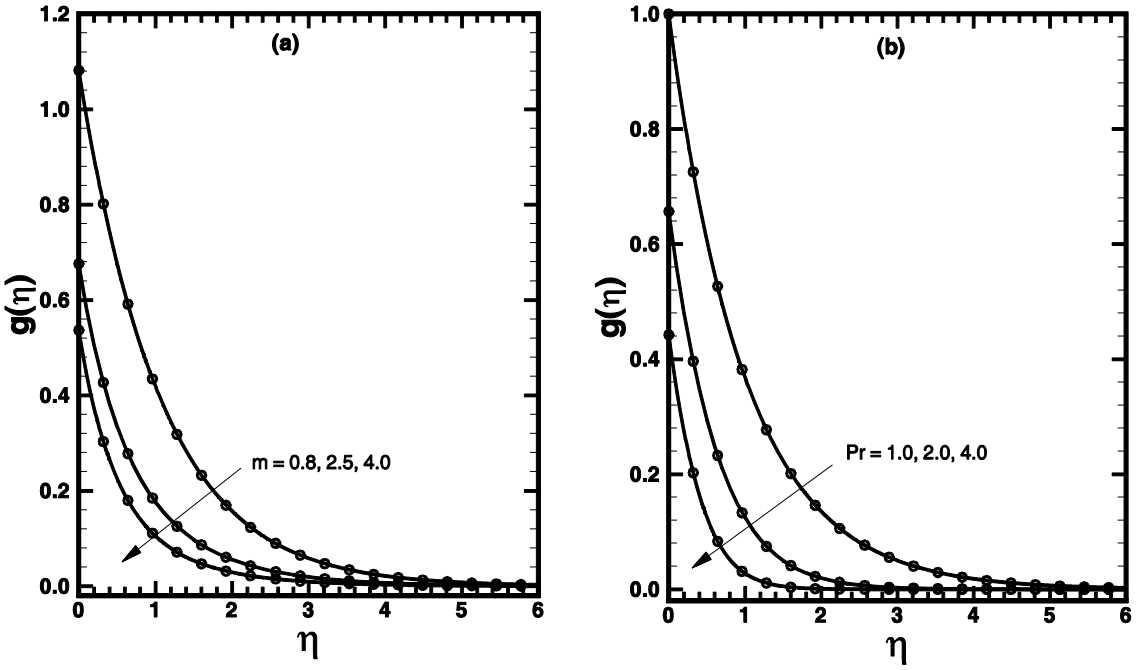

Figure 3.4: A comparison of the exact and numerical results (solid line numerical results and open circles exact results) in the PHF case when $n = s = 1$ and $A = 0$ are fixed.

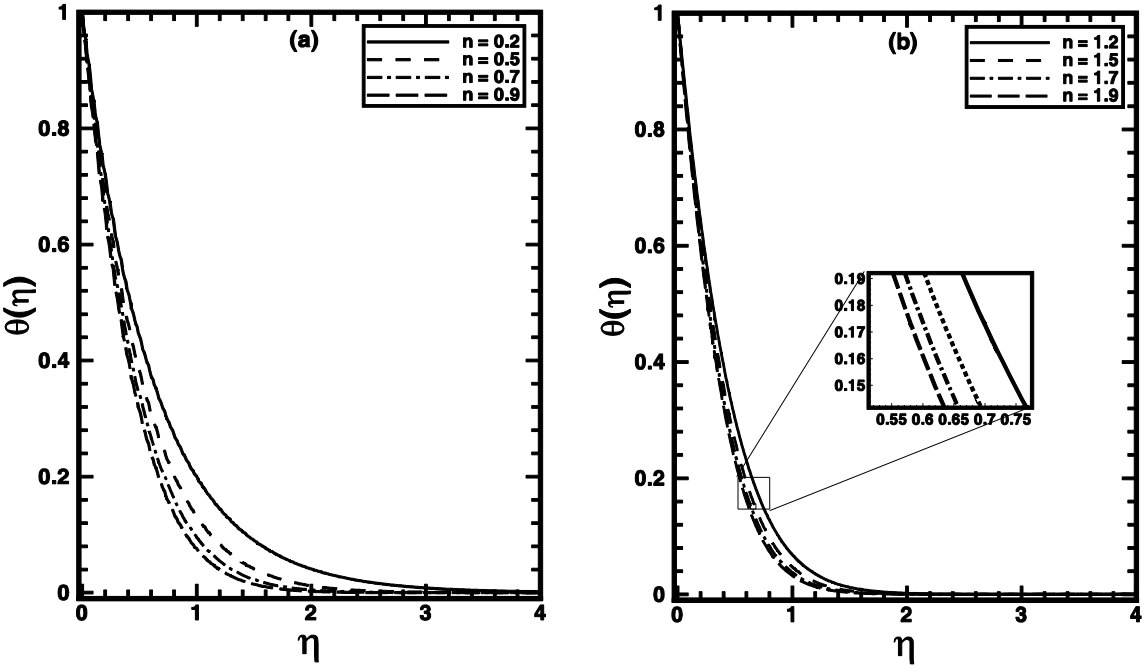

Figure 3.5: The temperature profile $\theta(\eta)$ in the PST case for different values of the power-law index n when $s = 1.5$, $\Pr = 3$, $m = 1$, and $A = 1.5$ are fixed.

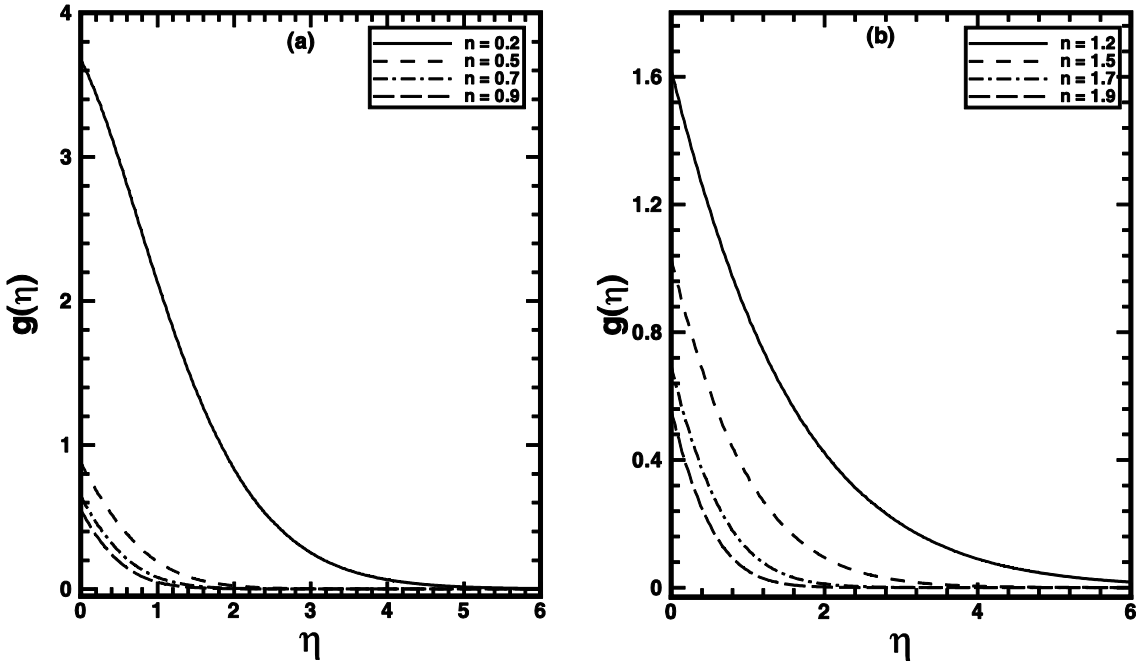

Figure 3.6: The temperature profile $g(\eta)$ in the PHF case for different values of the power-law index n when $s=1.5$, $\Pr=3$, $m=1$, and $A=1.5$ are fixed.

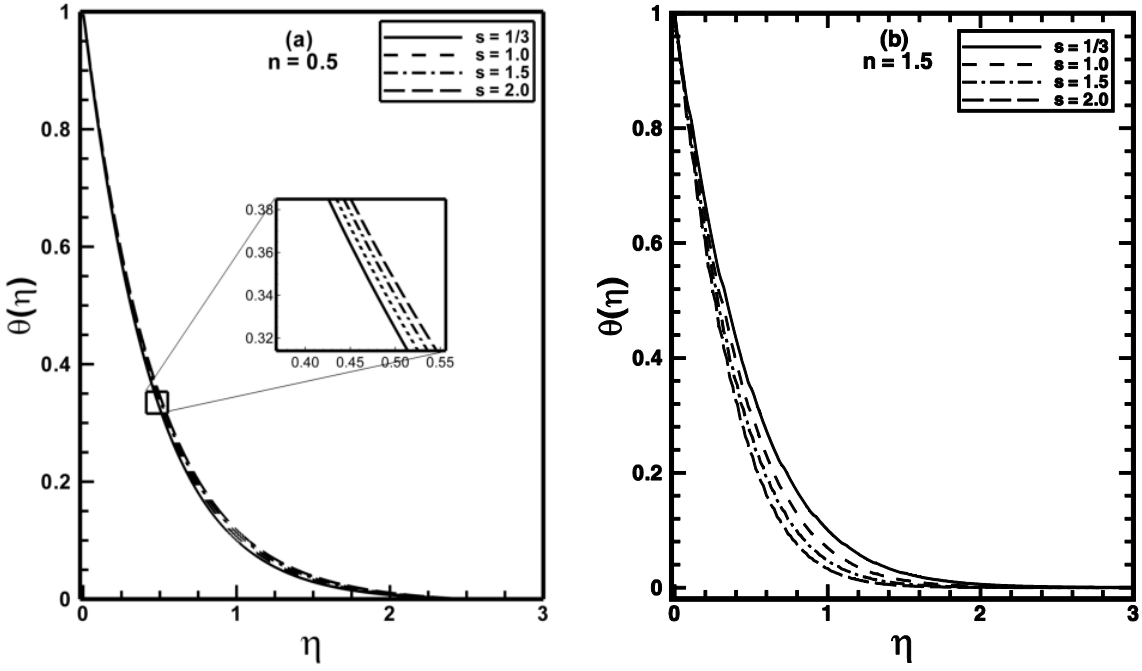

Figure 3.7: The temperature profile $\theta(\eta)$ in the PST case for different values of the stretching parameter *s* when $m=1.5$, $\Pr=3$, and $A=1.5$ are fixed.

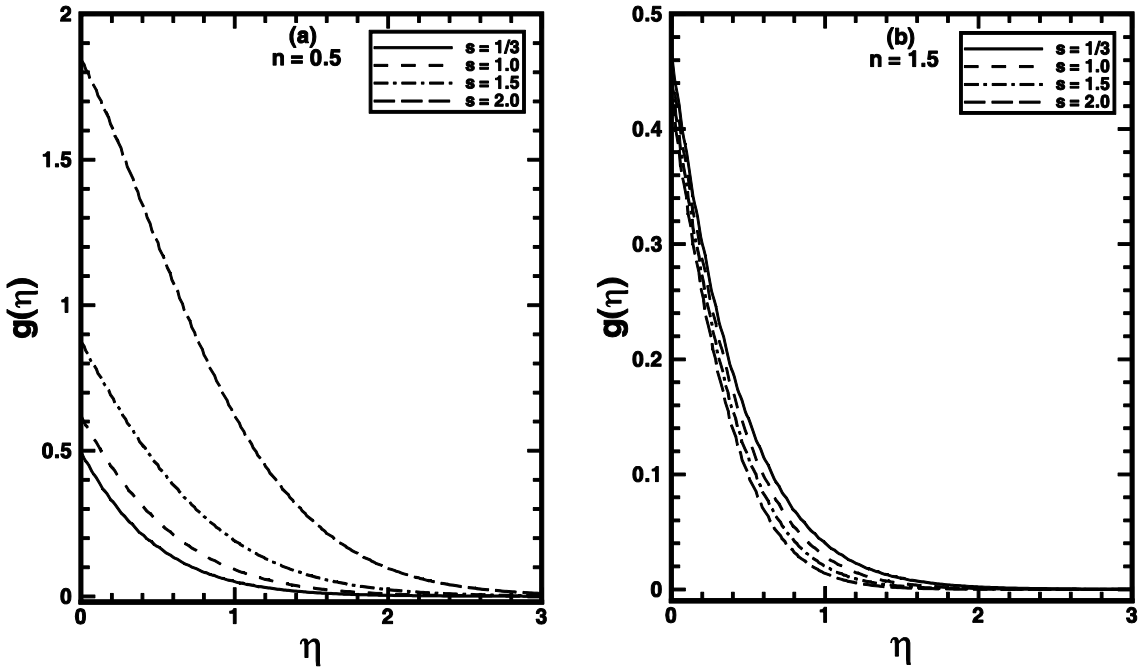

Figure 3.8: The temperature profile $g(\eta)$ in the PHF case for different values of the stretching parameter *s* when $m=1.5$, $\Pr=3$, and $A=1.5$ are fixed.

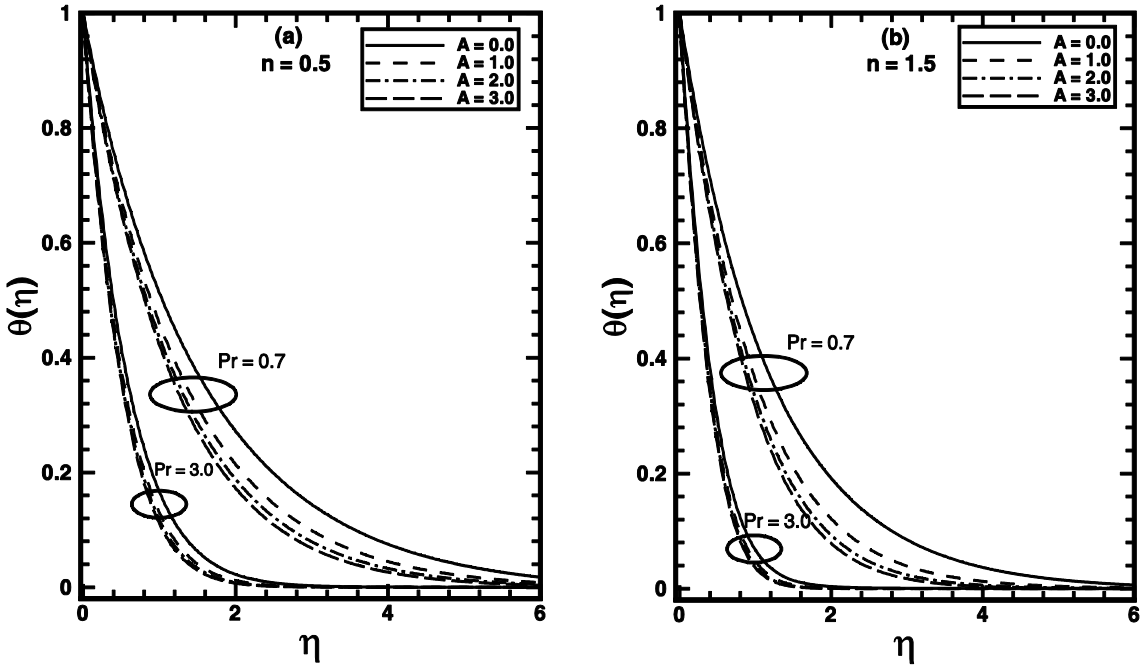

Figure 3.9: The temperature profile $\theta(\eta)$ in the PST case for different values of the material parameter *A* when $s=1.5$ and $m=1$ are fixed.

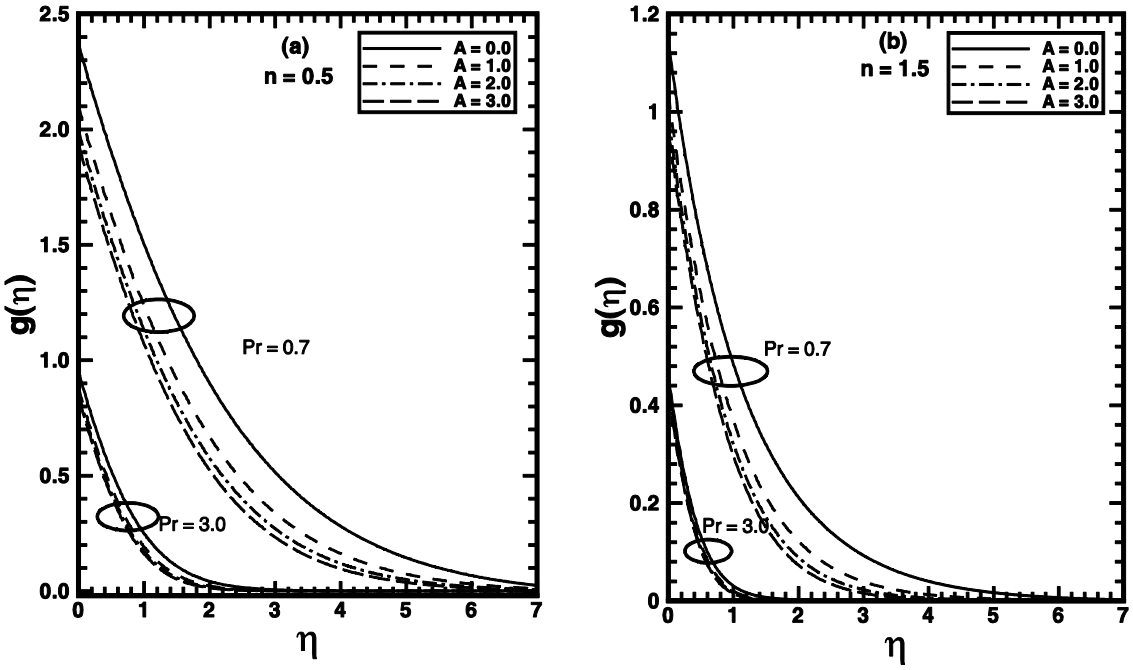

Figure 3.10: The temperature profile $g(\eta)$ in the PHF case for different values of the material parameter A when $s=1.5$ and $m=1$ are fixed.

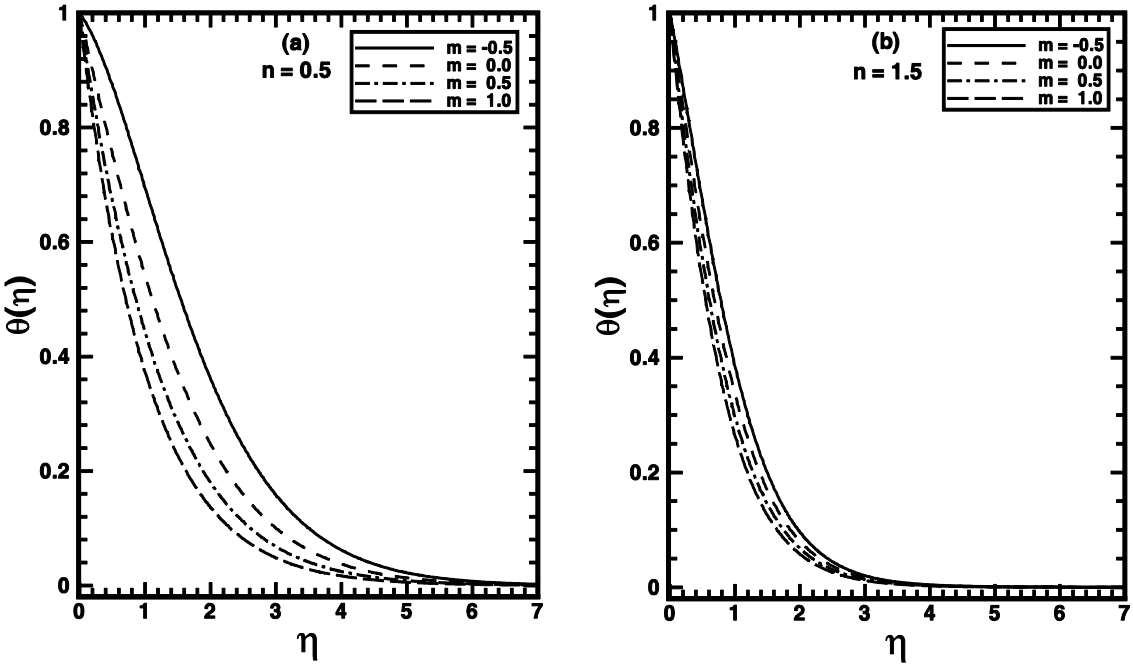

Figure 3.11: The temperature profile $\theta(\eta)$ in the PST case for different values of the temperature parameter m when $s=1.5$, $\Pr=3$ and $A=1.5$ are fixed.

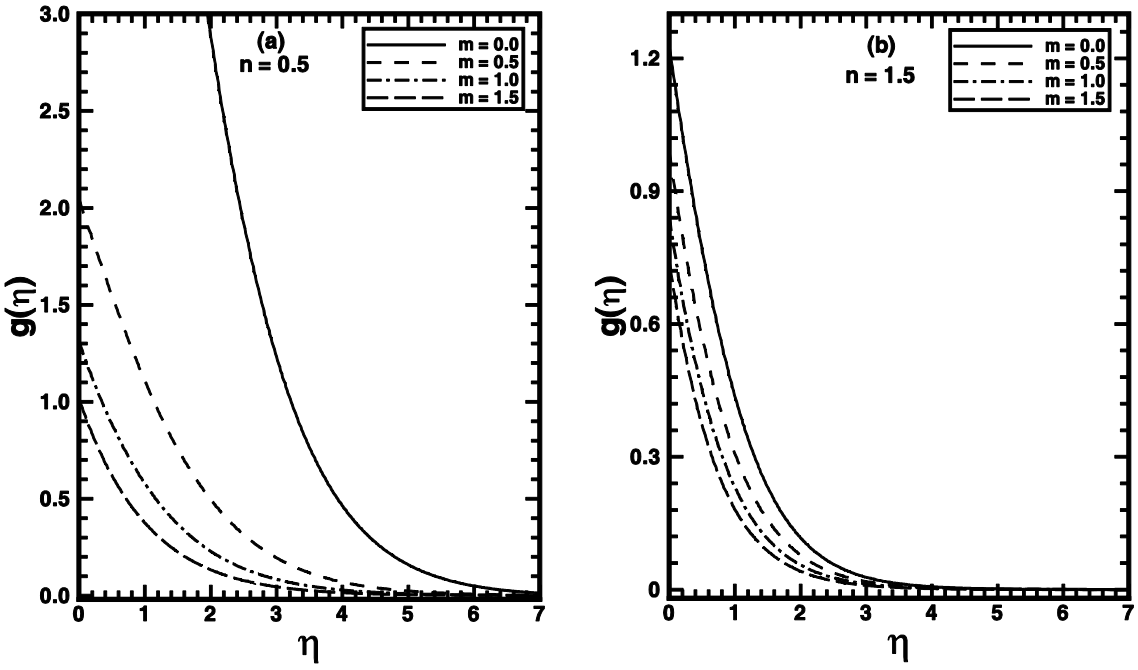

Figure 3.12: The temperature profile $g(\eta)$ in the PHF case for different values of the temperature parameter *m* when $s=1.5$, $\Pr=3$ and $A=1.5$ are fixed.

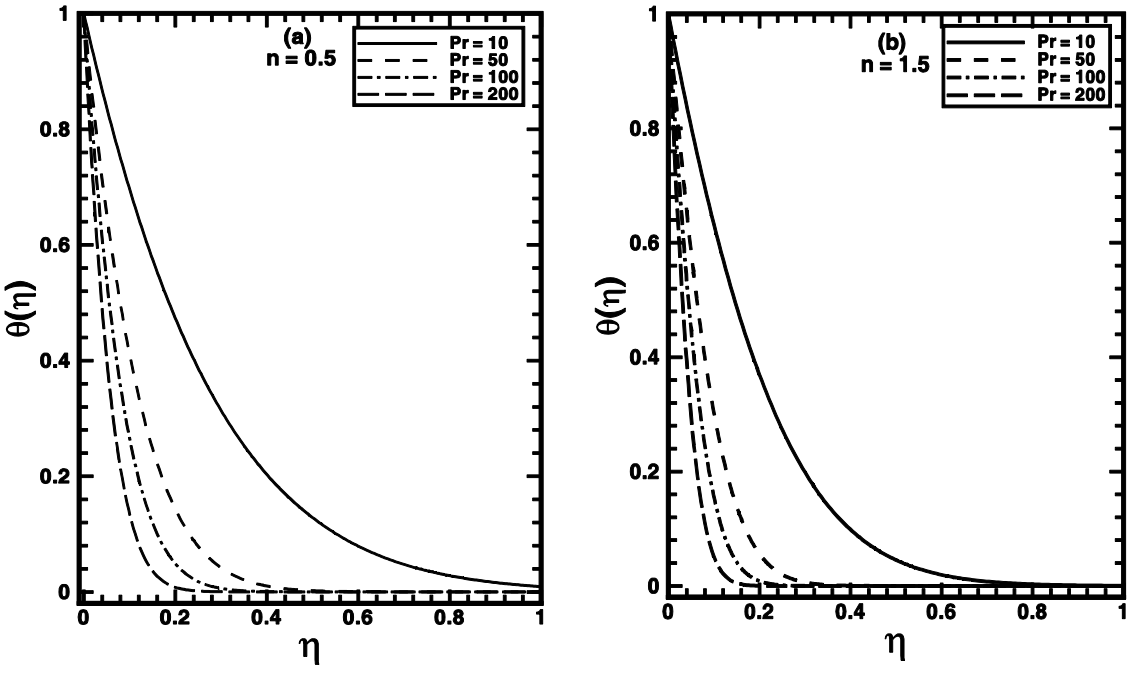

Figure 3.13: The temperature profile $\theta(\eta)$ in the PST case for different values of the Prandtl number Pr when $s=1.5$, $m=1$ and $A=1.5$ are fixed.

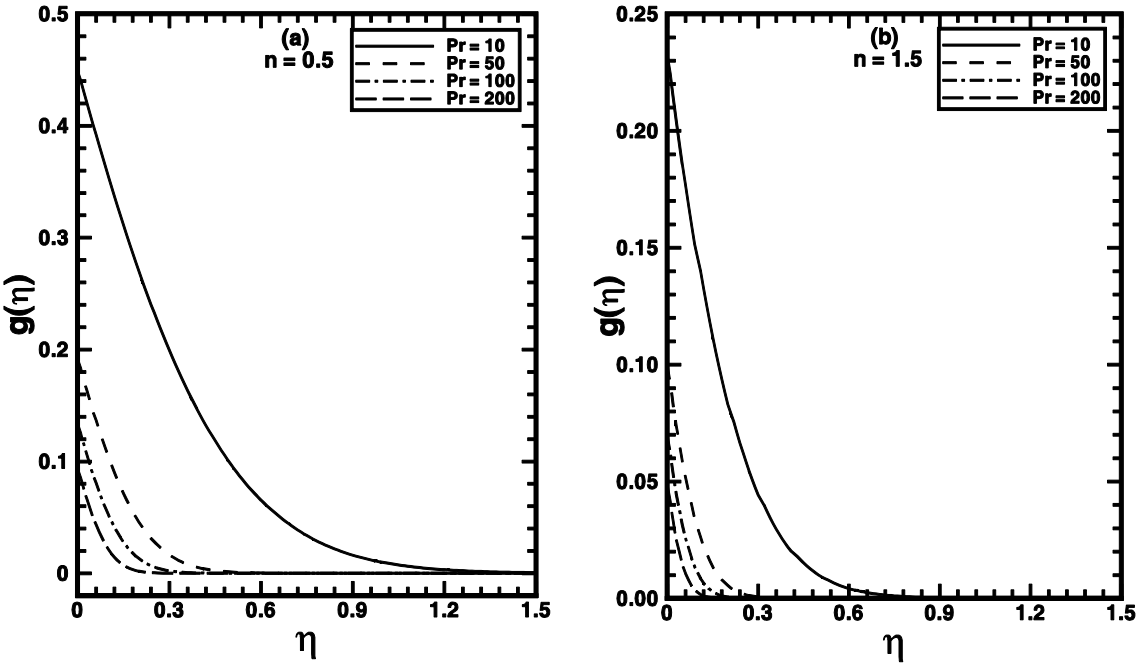

Figure 3.14: The temperature profile $g(\eta)$ in the PHF case for different values of the Prandtl number Pr when $s=1.5$, $m=1$ and $A=1.5$ are fixed.

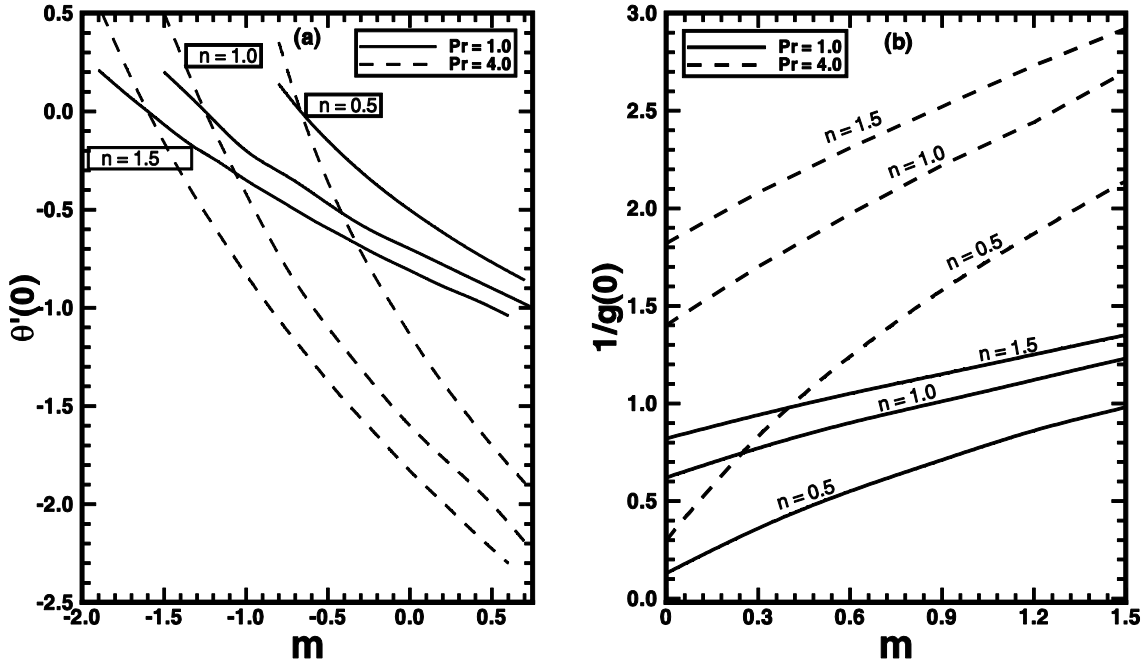

Figure 3.15: The variation of the local Nusselt number with *m* for some value of the power-law index *n* and Prandtl number Pr, when *A=1.5* and *s=1.5*.

Table 3.1: A comparison of the local Nusselt number in the PHF case.

	Chen[21]		Present study	
n	$g(0)$	$\mathrm{Re}_b^{-1/n+1} Nu_x$	$g(0)$	$\mathrm{Re}_b^{-1/n+1} Nu_x$
0.5	0.659092	1.517239	0.659091	1.517019
1.0	0.590316	1.694009	0.590312	1.694001
1.5	0.561785	1.780041	0.561781	1.780040

Table 3.2: The numerical values of the Local Nusselt number in the PST case when $m=1$ and $\mathrm{Pr}=1$ are fixed.

		-$\mathrm{Re}_b^{-1/n+1} Nu_x$	
A	s	$n=0.5$	$n=1.5$
1	1	1.01162	1.10805
2	1	1.04162	1.14661
3	1	1.05911	1.16897
1	2	0.96658	1.23540
2	2	1.00436	1.28120
3	2	1.02653	1.30854

Table 3.3: The numerical values of the Local Nusselt number in the PHF case when $m=1$ and $\mathrm{Pr}=1$ are fixed.

		$\mathrm{Re}_b^{-1/n+1} Nu_x$	
A	s	$n=0.5$	$n=1.5$
1	1	0.86916	1.17826
2	1	0.89766	1.21713
3	1	0.91446	1.23968
1	2	0.27308	1.23540
2	2	0.29081	1.28121
3	2	0.30209	1.30854

Table 3.4: The numerical values of the Local Nusselt number in the PST case when $s = 1.5,\ m = 0$ and $\Pr = 2$ are fixed.

$-\mathrm{Re}_b^{-1/n+1} Nu_x$		
A	$n = 0.5$	$n = 1.5$
1	0.76469	1.23231
2	0.79325	1.26755
3	0.81002	1.28841

Chapter 4

Convective Heat Transfer to Sisko Fluid over a Nonlinear Radially Stretching Sheet

The aim of present chapter is to study the flow and heat transfer characteristics of Sisko fluid over a radially stretching sheet with viscous dissipation effects. The stretching velocity of sheet is assumed to be nonlinear. The flow and heat transfer aspects are thoroughly investigated particularly for non-integer values of the flow behavior index. The modeled partial differential equations are reduced to a system of nonlinear ordinary differential equations using the appropriate transformations. The resulting equations are then solved numerically by implicit finite difference method in the flow domain. The numerical results for the velocity and temperature fields are graphically depicted and effects of the relevant parameters are discussed in detail. In addition, the skin friction coefficient and the local Nusselt number for different values of the pertaining parameters are given in tabulated form. Moreover, numerical results are compared with exact solutions as special cases of the problem. Furthermore, the present results for the velocity field are also validated by comparison with the previous pertinent literature. It is also noteworthy that the Bingham plastic and Newtonian fluids are special cases of the Sisko fluid, and a comparison of the momentum and thermal boundary layers characteristics of these fluids is also incorporated in this chapter.

4.1 Geometry of the Problem

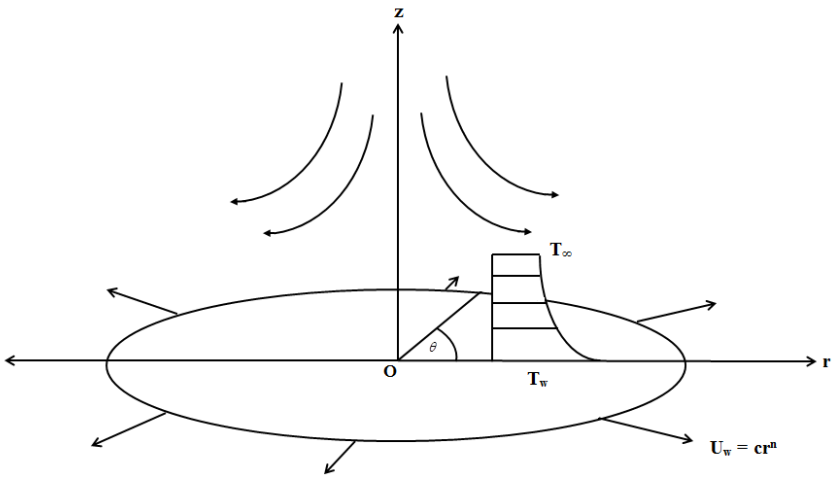

Figure 4.1: Flow geometry and coordinate system.

4.2 Mathematical Analysis

4.2.1 Flow Analysis

Consider the steady, two-dimensional and incompressible flow of a Sisko fluid over a nonlinear radially stretching sheet. The fluid is confined in the region $z > 0$, and flow is induced due to stretching of the sheet along the radial direction with velocity $U_w = cr^s$ with c and s are positive real numbers pertaining to stretching of the sheet. We assume that the constant temperature of the sheet is T_w, while T_∞ is the uniform ambient fluid temperature with $T_w > T_\infty$. The flow geometry is given by figure 4.1. For mathematical modeling we take the cylindrical polar coordinate system (r, ϕ, z). Due to the rotational symmetry, all the physical quantities are independent of ϕ. Under these conditions, the flow is governed by Eqs. (3.1) and (3.2). For a two-dimensional axisymmetric flow, we assume the velocity and stress fields of the form

$$\mathbf{V} = \left[u(r,z), 0, w(r,z)\right], \ \mathbf{S} = \mathbf{S}(r,z) \tag{4.1}$$

where u and v are the velocity components along the radial (r) and axial (z) directions, respectively.

In view of Eq. (4.1), the law of conservation of mass (3.1) results in

$$\frac{\partial u}{\partial r}+\frac{u}{r}+\frac{\partial w}{\partial z}=0, \tag{4.2}$$

while the equation of motion (3.2) takes the relevant component form:

$$\rho\left(u\frac{\partial u}{\partial r}+w\frac{\partial u}{\partial z}\right)=-\frac{\partial p}{\partial r}+\frac{\partial s_{rr}}{\partial r}+\frac{\partial s_{rz}}{\partial z}+\frac{s_{rr}-s_{\phi\phi}}{r}, \tag{4.3}$$

$$\rho\left(u\frac{\partial w}{\partial r}+w\frac{\partial w}{\partial z}\right)=-\frac{\partial p}{\partial z}+\frac{1}{r}\frac{\partial}{\partial r}\left(rs_{rz}\right)+\frac{\partial s_{zz}}{\partial z}. \tag{4.4}$$

Upon substitution of the stress components as given by Eq. (4.1) and within the frame work of simplifying assumptions the momentum Eqs. (4.3) and (4.4) turn out to be the following

$$\rho\left(u\frac{\partial u}{\partial r}+w\frac{\partial u}{\partial z}\right)=a\frac{\partial^2 u}{\partial z^2}-b\frac{\partial}{\partial z}\left(-\frac{\partial u}{\partial z}\right)^n, \tag{4.5}$$

where a, b and n (≥ 0) are the material constants.

The boundary conditions associated to flow field are

$$u=cr^s,\ w=0 \ \text{ at } \ z=0, \tag{4.6}$$

$$u\to 0 \ \text{ as } \ z\to\infty. \tag{4.7}$$

We define the following variables

$$\eta=\frac{z}{r}\mathrm{Re}_b^{\frac{1}{n+1}} \ \text{ and } \ \psi\left(r,z\right)=-r^2U\,\mathrm{Re}_b^{\frac{-1}{n+1}}\,f\left(\eta\right), \tag{4.8}$$

where $\psi\left(r,z\right)$ is the Stokes stream function defined by $u=-\frac{1}{r}\frac{\partial\psi}{\partial z}$ and $w=\frac{1}{r}\frac{\partial\psi}{\partial r}$ giving

$$u=Uf'\left(\eta\right) \text{ and } w=-U\,\mathrm{Re}_b^{\frac{-1}{n+1}}\left[\frac{s\left(2n-1\right)+n+2}{n+1}f\left(\eta\right)-\frac{s\left(n-2\right)+1}{n+1}\eta f'\left(\eta\right)\right]. \tag{4.9}$$

On employing the above transformations, Eqs. (4.5) to (4.7) take the form [25]

$$Af''' + n\left[-f''\right]^{n-1} f''' + \left(\frac{s(2n-1)+n+2}{n+1}\right) ff'' - s(f')^2 = 0, \tag{4.10}$$

$$f(0) = 0,\ \ f'(0) = 1 \text{ and } f'(\eta) \to 0 \text{ as } \eta \to \infty, \tag{4.11}$$

where prime denotes differentiation with respect to η and

$$\mathrm{Re}_a = \rho r U / a,\ \mathrm{Re}_b = \rho r^n U^{2-n} / b \text{ and } A = \mathrm{Re}_b^{\frac{2}{n+1}} / \mathrm{Re}_a . \tag{4.12}$$

The physical quantity of pivotal interest is the local skin friction coefficient and is given by [25]

$$\frac{1}{2}\mathrm{Re}_b^{\frac{1}{n+1}} C_f = Af''(0) - \left[-f''(0)\right]^n . \tag{4.13}$$

4.2.2 Heat Transfer Analysis

The energy balance equation (3.3), by taking into account the viscous dissipation effects and neglecting heat generation effects for temperature field $T = T(r,z)$ may be written as

$$u\frac{\partial T}{\partial r} + w\frac{\partial T}{\partial z} = \frac{\kappa}{\rho c_p}\frac{\partial^2 T}{\partial z^2} + \frac{1}{\rho c_p}\left[a\left(\frac{\partial u}{\partial z}\right)^2 + b\left(-\frac{\partial u}{\partial z}\right)^{n+1}\right], \tag{4.14}$$

where c_p is the specific heat at constant pressure and κ the thermal conductivity.

The corresponding boundary conditions are

$$T = T_w \ \text{ at } \ z = 0, \tag{4.15}$$

$$T \to T_\infty \ \text{ as } \ z \to \infty. \tag{4.16}$$

Using the transformations (4.8) the above problem reduces to

$$\theta'' + \Pr \frac{s(2n-1)+(n+2)}{n+1} f\theta' + Br(f'')^2 + \Pr Ec(-f'')^{n+1} = 0, \tag{4.17}$$

$$\theta(0) = 1 \text{ and } \theta \to 0 \text{ as } \eta \to \infty, \tag{4.18}$$

where $\theta(\eta) = \frac{T-T_\infty}{T_w-T_\infty}$, $Br = \frac{aU^2}{\kappa(T_w-T_\infty)}$, the Brinkman number, $Ec = \frac{U^2}{c_p(T_w-T_\infty)}$ the Eckert number and $\Pr = \frac{rUR^{\frac{-2}{n+1}}}{\alpha}$ the generalized Prandtl number.

The local Nusselt number Nu_r at the wall is defined as

$$Nu_r = \left.\frac{rq_w}{\kappa(T_w - T_\infty)}\right|_{z=0}, \tag{4.19}$$

where the wall heat flux at the wall is $q_w = -\kappa\left(\frac{\partial T}{\partial z}\right)\Big|_{z=0}$, which by virtue of Eq. (4.19) reduces to

$$\mathrm{Re}_b^{-1/n+1} Nu_r = -\theta'(0). \tag{4.20}$$

4.3 Exact Solutions for Particular Cases

It is pertinent to mention that Eq. (4.10) has simple exact solution to special cases, namely (i) $n = 0$ and $s = 1$ [25] (*ii*) $n = 1$, and $s = 3$ [73]. For case (*i*), with $Br = Ec = 0$, Eq. (4.17) reduces to

$$\theta'' + \Pr f\theta' = 0. \tag{4.21}$$

The exact solution to Eq. (4.21) in terms of the incomplete Gamma function, satisfying boundary conditions (4.18) is

$$\theta(\eta) = \frac{\Gamma(\frac{\Pr}{\beta^2}, 0) - \Gamma(\frac{\Pr}{\beta^2}, \frac{\Pr}{\beta^2} e^{-\beta\eta})}{\Gamma(\frac{\Pr}{\beta^2}, 0) - \Gamma(\frac{\Pr}{\beta^2}, \frac{\Pr}{\beta^2})}, \tag{4.22}$$

where $\beta = \frac{1}{\sqrt{A}}$ and $\Gamma(\cdot)$ is the incomplete Gamma function.

For case (ii), with $Br = Ec = 0$, Eq. (4.17) reduces to

$$\theta'' + 3\Pr f\theta' = 0. \tag{4.23}$$

Here the exact solution of Eq. (4.23) in terms of incomplete Gamma function, satisfying boundary conditions (4.18) is

$$\theta(\eta) = \frac{\Gamma(\frac{3\Pr}{\alpha^2}, 0) - \Gamma(\frac{3\Pr}{\alpha^2}, \frac{3\Pr}{\alpha^2} e^{-\alpha\eta})}{\Gamma(\frac{3\Pr}{\alpha^2}, 0) - \Gamma(\frac{3\Pr}{\alpha^2}, \frac{3\Pr}{\alpha^2})}, \tag{4.24}$$

where $\alpha = \frac{\sqrt{3}}{\sqrt{1+A}}$.

4.4 Solution Procedure

The two point boundary value problems comprising Eqs. (4.10) and (4.17) along with the associated boundary conditions are solved by implicit finite difference scheme along with Keller box scheme. To implement the scheme, Eqs. (4.10) and (4.17) are written as a system of first-order differential equations in η as follows

$$f' = p, \tag{4.25}$$

$$p' = q, \tag{4.26}$$

$$Aq' + n(-q)^{n-1}q' + Dfq - sp^2 = 0, \tag{4.27}$$

where $D = \frac{s(2n-1) + (n+2)}{n+1}$.

$$\theta' = t, \tag{4.28}$$

$$t' + \Pr Ec(-q)^{n+1} + \Pr Dft + Brq^2 = 0. \tag{4.29}$$

The boundary conditions in terms of new variable are written as

$$f(0) = 0,\ p(0) = 1 \text{ and } \theta(0) = 1, \tag{4.30}$$

$$p \to 0 \text{ and } \theta \to 0 \text{ as } \eta \to \infty. \tag{4.31}$$

The functions and their derivatives are approximated by central difference at the mid-point $\eta_{j-\frac{1}{2}}$ of the segment $\eta_{j-1}\eta_j$, where $j = 1, 2, \ldots N$

$$\eta_0 = 0,\ \eta_j = \eta_{j-1} + h_j,\ \eta_N = \eta_\infty. \tag{4.32}$$

Using the finite difference approximations equations (4.25) to (4.29) can be written as

$$f_j - f_{j-1} - h_j p_{j-1/2} = 0, \tag{4.33}$$

$$p_j - p_{j-1} - h_j q_{j-1/2} = 0, \tag{4.34}$$

$$A(q_j - q_{j-1}) + nh_j(-q_{j-1/2})^{n-1}(q_j - q_{j-1}) - \mathrm{s}\, h_j (p_{j-1/2})^2 + Dh_j f_{j-1/2} q_{j-1/2} = 0, \tag{4.35}$$

$$\theta_j - \theta_{j-1} - h_j t_{j-1/2} = 0, \tag{4.36}$$

$$(t_j - t_{j-1}) + \mathrm{Pr}\, Ech_j(-q_{j-1/2})^{n+1}(q_j - q_{j-1}) + Brh_j(q_{j-1/2})^2 + D\,\mathrm{Pr}\, h_j f_{j-1/2} t_{j-1/2} = 0, \tag{4.37}$$

where $j = 1, 2, 3, \cdots N$ and $p_{j-1/2} = \dfrac{p_j + p_{j-1}}{2}$.

Boundary conditions (4.30) and (4.31) are written as

$$f_0 = 0,\ p_0 = 1,\ \theta_0 = 1, \tag{4.38}$$

$$p_N = 0 \text{ and } \theta_N = 0. \tag{4.39}$$

Eqs. (4.33) to (4.37) are system of nonlinear equations, these equations are linearized employing the Newton's method and using the expressions:

$$f_j^{(k+1)} = f_j^{(k)} + \delta f_j^{(k)},\ p_j^{(k+1)} = p_j^{(k)} + \delta p_j^{(k)},\ q_j^{(k+1)} = q_j^{(k)} + \delta q_j^{(k)},$$

$$\theta_j^{(k+1)} = \theta_j^{(k)} + \delta\theta_j^{(k)},\ t_j^{(k+1)} = t_j^{(k)} + \delta t_j^{(k)}, \tag{4.40}$$

where $k = 1, 2, 3, \ldots$

Putting the left hand side of the above expressions into Eqs. (4.33) to (4.37) and dropping the quadratic terms in $\delta f^{(k)}$, $\delta p^{(k)}$, $\delta q^{(k)}$, $\delta\theta^{(k)}$ and $\delta t^{(k)}$, the following linear equations is obtained:

$$\delta f_j - \delta f_{j-1} - h_j \delta p_{j-1/2} = (r_1)_{j-1/2}, \tag{4.41}$$

$$(\xi_1)_j \delta q_j + (\xi_2)_j \delta q_{j-1} + (\xi_3)_j \delta f_j + (\xi_4)_j \delta f_{j-1} +$$

$$(\xi_5)_j \delta p_j + (\xi_6)_j \delta p_{j-1} + (\xi_7)_j \delta\theta_j + (\xi_8)_j \delta\theta_{j-1} = (r_2)_{j-1/2}, \tag{4.42}$$

$$(\eta_1)_j \delta t_j + (\eta_2)_j \delta t_{j-1} + (\eta_3)_j \delta f_j + (\eta_4)_j \delta f_{j-1} +$$

$$(\eta_5)_j \delta p_j + (\eta_6)_j \delta p_{j-1} + (\eta_7)_j \delta\theta_j + (\eta_8)_j \delta\theta_{j-1} = (r_3)_{j-1/2}, \tag{4.43}$$

$$\delta p_j - \delta p_{j-1} - h_j \delta q_{j-1/2} = (r_4)_{j-1/2}, \tag{4.44}$$

$$\delta\theta_j - \delta\theta_{j-1} - h_j \delta t_{j-1/2} = (r_5)_{j-1/2}, \tag{4.45}$$

where

$$\xi_1 = \left[A - n(n-1)\left(\frac{q_j - q_{j-1}}{2}\right)\left(-q_{j-1/2}\right)^{n-2} + n\left(-q_{j-1/2}\right)^{n-1} + \frac{Dh_j}{2} f_{j-1/2} \right] \tag{4.46}$$

$$\xi_2 = \left[-A - n(n-1)\left(\frac{q_j - q_{j-1}}{2}\right)\left(-q_{j-1/2}\right)^{n-2} + n\left(-q_{j-1/2}\right)^{n-1} + \frac{Dh_j}{2} f_{j-1/2} \right] \tag{4.47}$$

$$\xi_3 = \xi_4 = \frac{Dh_j}{2} q_{j-1/2},\ \xi_5 = \xi_6 = -sh_j p_{j-1/2},\ \xi_7 = \xi_8 = 0, \tag{4.48}$$

and

$$\eta_1 = 1 + \frac{D\,\mathrm{Pr}}{2} h_j f_{j-1/2},\ \eta_2 = \eta_1 - 2,\ \eta_3 = \eta_4 = \frac{D\,\mathrm{Pr}}{2} h_j t_{j-1/2}, \tag{4.49}$$

$$\eta_5 = \eta_6 = Brh_j q_{j-1/2} - \frac{\Pr Ec}{2}(n+1)h_j\left(-q_{j-1/2}\right)^n. \tag{4.50}$$

The right hand sides of Eqs. (4.41) to (4.45) are given by

$$r_1 = -\left(f_j - f_{j-1}\right) + h_j p_{j-1/2}, \tag{4.51}$$

$$r_2 = -\left[A\left(q_j - q_{j-1}\right) + Dh_j f_{j-1/2} q_{j-1/2} - sh_j p_{j-1/2}^2\right] - n\left(q_j - q_{j-1}\right)\left(-q_{j-1/2}\right)^{n-1}, \tag{4.52}$$

$$r_3 = -\left[\left(t_j - t_{j-1}\right) + D\Pr h_j f_{j-1/2} t_{j-1/2} + Brh_j q_{j-1/2}^2 + \Pr Ec\left(-q_{j-1/2}\right)^{n+1}\right], \tag{4.53}$$

$$r_4 = -\left(p_j - p_{j-1}\right) + h_j q_{j-1/2},\ r_5 = -\left(\theta_j - \theta_{j-1}\right) + h_j t_{j-1/2}. \tag{4.54}$$

The boundary conditions (4.38) and (4.39) become

$$\delta f_0 = 0,\ \delta p_0 = 0,\ \delta q_0 = 0,\ \delta\theta_0 = 0,\ \delta q_N = 0 \text{ and } \delta\theta_N = 0. \tag{4.55}$$

Linearized Eqs. (4.41) to (4.45) can be solved by using block elimination method as outlined by Na [66]. The iterative procedure is stopped when the difference in computing the velocity and the temperature in the next iteration is less than 10^{-5}. The present method is unconditionally stable and has second-order accuracy.

4.4.1 Validation of the Numerical Results

The validation of results is essential to check the credibility of the numerical solution methodology. The presently computed results are compared with the exact results obtained for some limiting cases of the problem. Figures 4.2 and 4.3 compare these results, and an excellent correspondence is seen to exist between the two sets of data. In addition, table 4.1 shows the comparison values of the local skin friction coefficient with those reported by of Khan and Shahzad [25]. It is seen that the comparison is in very

good agreement, and thus gives us confidence to the accuracy of the numerical results.

4.5 Numerical Results and Discussion

The focus of this chapter is to study the flow and heat transfer characteristics of a Sisko fluid over a nonlinear radially stretching sheet. To obtain the physical insight of the flow and heat transfer, Eqs. (4.10) and (4.17) subject to boundary conditions (4.11) and (4.18) are solved numerically and results are illustrated graphically. The influence of the flow behavior index n, the material parameter A, stretching parameter s, and Eckert number Ec on flow and heat transfer is the main interest of the study. Further, the effect of variation of Prandtl number $\Pr$ on heat transfer is also analyzed in depth. A comparison amongst the flow and heat transfer aspects of the Bingham, Newtonian, and Sisko fluids is also precisely depicted. Moreover, the flow and heat transfer characteristics are also discussed in terms of the local skin friction coefficient and local Nusselt number.

Figure 4.4 depicts the influence of the power-law index n on the velocity profile for pseudo-plastic and dilatant regimes for a nonlinearly stretching sheet. The lower is the value of n, greater is the degree of shear thinning. Figure 4.4(a) shows that the velocity profile and momentum boundary layer thickness decrease with an increase in value of the power-law index n, owing to an increase in apparent viscosity. The shear thickening behavior $(n>1)$ is illustrated in figure 4.4(b). This figure reveals that as value of the power-law index n is progressively incremented, the velocity profile and corresponding momentum boundary layer thickness decrease due to gradual strengthening of viscous effects.

The heat transfer aspects of the Sisko fluid over a constant surface temperature stretching sheet for shear thinning and thickening fluids for different values of the power-

law index n, for nonlinear stretching is illustrated in figures 4.5. Figure 4.5(a) depicts that the temperature profile and thermal boundary layer reduce with incrementing value of power-law index $n<1.$ The effect on the temperature profile is marginalized when the power-law index approaches unity. Figure 4.5(b) reveals that the power-law index n does not affect the temperature profile strongly for $n>1.$ However, a slight decrease in the thermal boundary layer thickness is observed.

The stretching parameter s affects the temperature distribution and thermal boundary layer due to application of shear stress at the boundary. Its effect on heat transfer is illustrated in figures 4.6(a,b). For the power-law index $(n<1),$ stretching parameter s does not affect the heat transfer in the Sisko fluid very strongly. The thermal boundary layer thickness increases when value of s is incremented progressively (figure 4.6(a)). Figure 4.6(b) represents the temperature profiles for $n=1.5.$ The temperature profile seems to decrease as value of the stretching parameter is incremented. Moreover, it is also noticed that larger the value of the power-law index n the more is the decrease in the temperature profile.

The effect of the material parameter A on the temperature profile for nonlinear stretching is presented in figures 4.7(a,b). These figures also make a comparison amongst the temperature profiles of the Newtonian fluid $(A=0$ and $n=1)$ and the power-law fluid $(A=0$ and $n\neq 1)$ with those of the Sisko fluid $(A\neq 0).$ Qualitatively, figures 4.7(a,b) reveal that the temperature profile and the corresponding thermal boundary layer thickness reduce in each case with increasing value of the material parameter $A.$

The Prandtl number $\Pr$ of a fluid plays a significant role in forced convective heat transfer. Figures 4.8(a,b) present its effect on heat transfer in Sisko fluid for pseudo

plastic and dilatant regimes. These figures depict that the Pr affects the heat transfer process strongly by thinning the thermal boundary layer thickness. It in turn augments the heat transfer at the wall. The augmentation can be ascribed to the enhanced momentum diffusivity for larger Prandtl number. The temperature profile is slightly lower for fluids with shear thickening behavior than that of the shear thinning for same Prandtl number.

Eckert number (Ec) measures the transformation of kinetic energy into heat by viscous dissipation. The variation of temperature with increasing Ec is given in figures 4.9(a,b). Figure 4.9(a) describes the effect of increasing Ec on highly shear thinning $(n=0.2)$ and moderately shear thinning $(n=0.6)$ Sisko fluids. This figure clearly elucidates that the temperature profile increases with increasing Ec. Further the strongly shear thinning fluids are dominantly affected by Ec as compared to that of the moderately shear thinning regime. Figure 4.9(b) reveals the same phenomenon for shear thickening fluids $(n>1)$, but here the effects are less prominent.

Figures 4.10(a,b) compare the velocity and temperature profiles of the Bingham $(n=0 \text{ and } A\neq 0)$ and Newtonian $(n=1 \text{ and } A=0)$ fluids with those of the Sisko fluid $(n\neq 0 \text{ and } A\neq 0)$. While sketching figure 4.10(a), the value of the material parameter A is adjusted at 1.5. This figure clearly shows that for a particular value of η, the velocity profile of the Bingham fluid substantially higher than those of the Newtonian and Sisko fluids. This figure also delineates that the velocity variation of the Bingham fluid approaches free stream velocity for larger values of η as compared to those the Newtonian and Sisko fluids. The temperature profiles of three different fluids are demonstrated in figure 4.10(b). The Bingham fluid shows larger thermal boundary layer thickness, whilst that of the Sisko fluid least, resulting better heat transfer. A wider variation in the concomitant heat transfer slopes at wall is observed in this figure with

least slop for the Bingham fluid, showing a minimum heat transfer at the wall.

The adiabatic Eckert number Ec_a is a measure of heat flux (q_x) direction; the heat flows from heated sheet to fluid $(q_x > 0)$ when $Ec < Ec_a$, and vice versa. Figure 4.11 shows a series of adiabatic Eckert numbers evaluated numerically for shear thinning $(n = 0.5)$ and shear thickening $(n = 1.5)$ Sisko fluids. It is clearly noticed from these figures that the adiabatic Eckert number increases at an accelerated pace for smaller values of the Prandtl number. Further inspection of these figures show that value of Ec_a decreases at a rapid rate for shear thinning fluid as compared to that of shear thickening fluid.

Table 4.2 summarizes the overall trends in the skin friction coefficient for shear thinning and thickening fluids when the material parameter A, stretching parameter s, Eckert number Ec and Br are varied. This table reveals that the value of the skin friction increases with each increment in value of the material parameter A for linear as well as nonlinear stretching of the sheet, which results in increased drag to the Sisko fluid. Further, this table also shows the variation in the local Nusselt number with the increasing value of A for linear and nonlinear stretching. The Nusselt number shows improvement with an each increment of A. It is also clear that the improvement is better for the power-law index $n > 1$. Moreover, a decrease in local Nusselt number is observed with an increase in Ec and Br. It is further noticed that the decrease in heat transfer from wall to fluid is about 24% for shear thinning and 13% for shear thickening fluids over the range taken in the table. Table 4.3 shows the effects of the Prandtl number $\Pr$ on the local Nusselt number for different values of the power-law index n. An increase in the Prandtl number augments the Nusselt number at the sheet. Moreover, an increase in the Nusselt number is larger for fluids with medium power-law index n. Variation of local

Nusselt number with material parameter without viscous dissipation (special case) is shown in table 4.4. The table depicts that Nusselt number is much larger than the planar stretching case (cf. chapter 3).

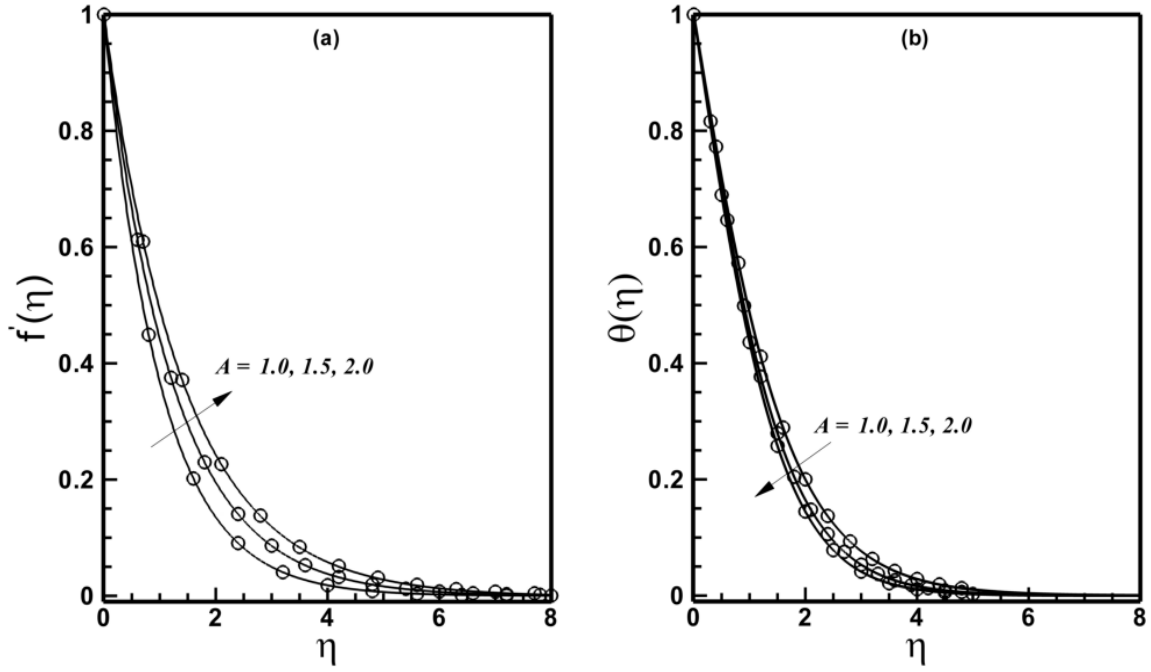

Figure 4.2: A comparison of the exact and numerical results (solid line numerical results and open circles exact results) when $n=0$ and $s=1$ are fixed.

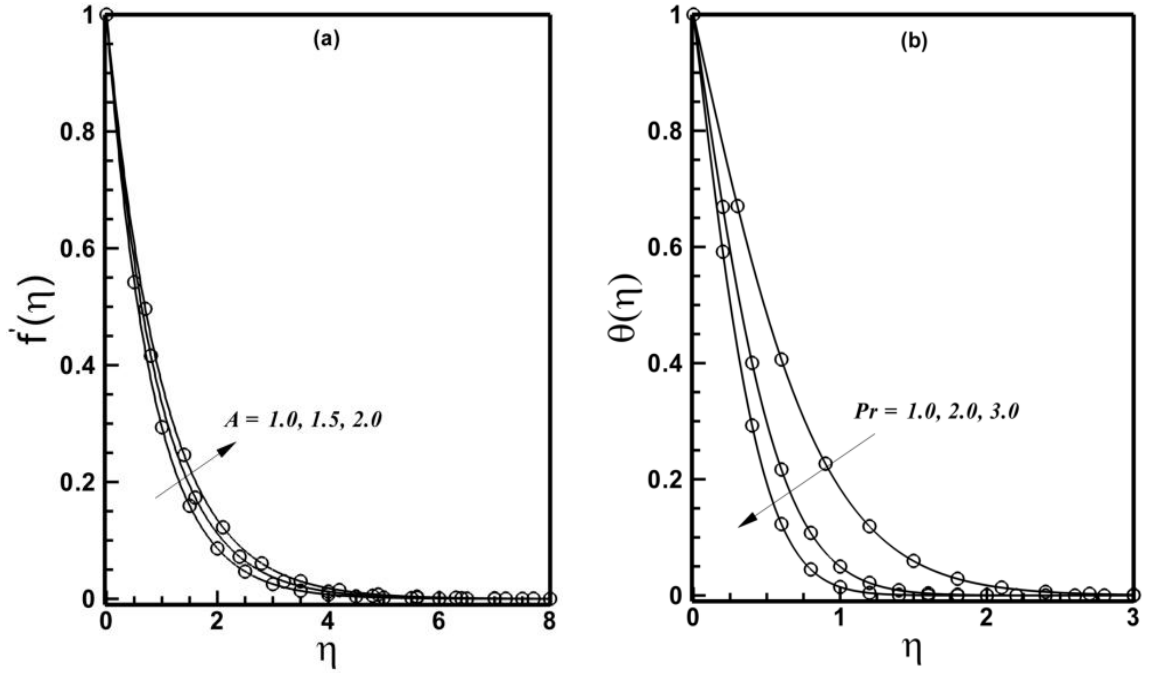

Figure 4.3: A comparison of the exact and numerical results (solid line numerical results and open circles exact results) when $n=1$ and $s=3$ are fixed.

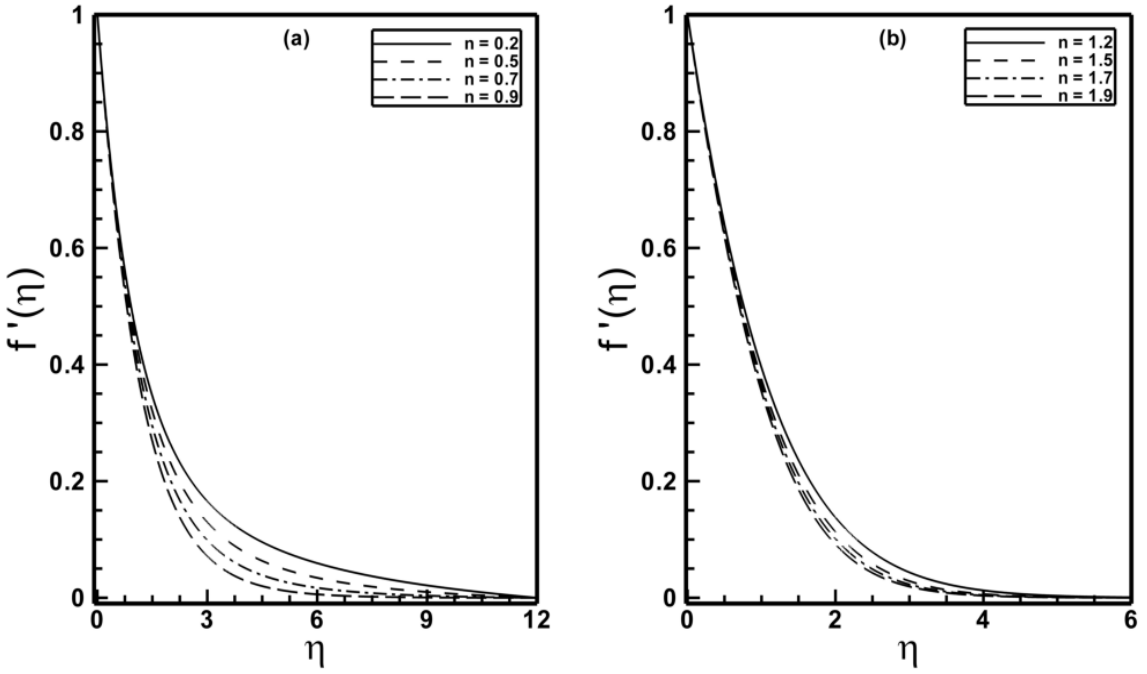

Figure 4.4: The velocity profile $f'(\eta)$ for different values of the power-law index n when $s=1.5$ and $A=1.5$ are fixed.

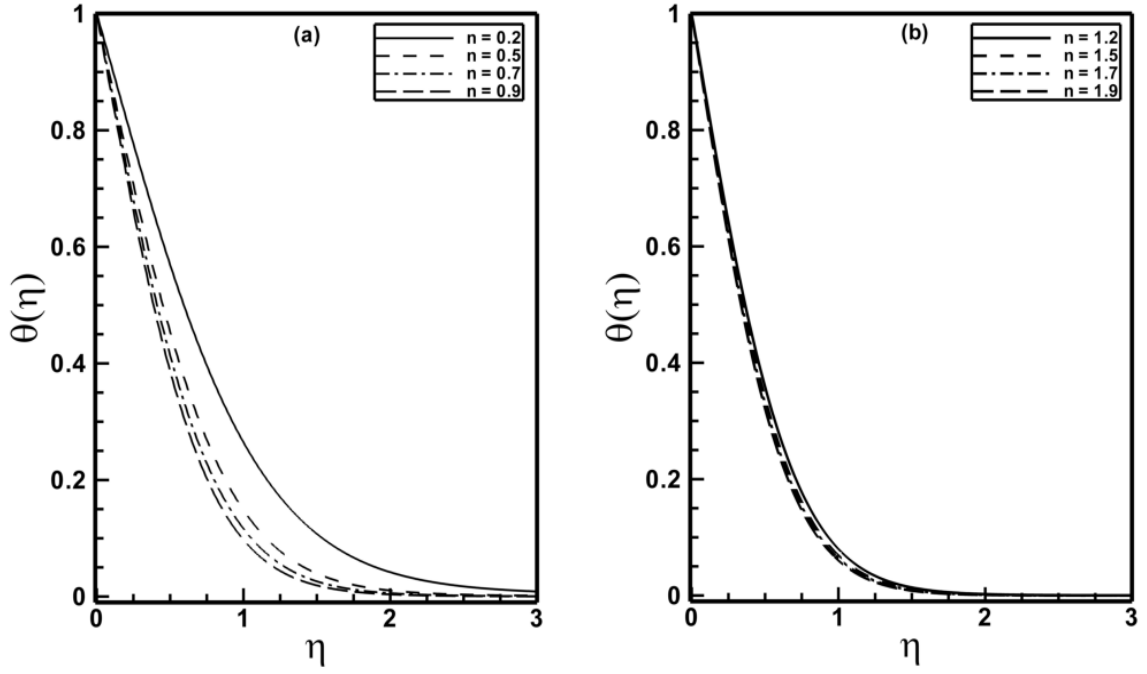

Figure 4.5: The temperature profile $\theta(\eta)$ for different values of the power-law index n when $s=1.5$, $A=1.5$, $\Pr=2.0$, $Ec=0.1$ and $Br=0.1$ are fixed.

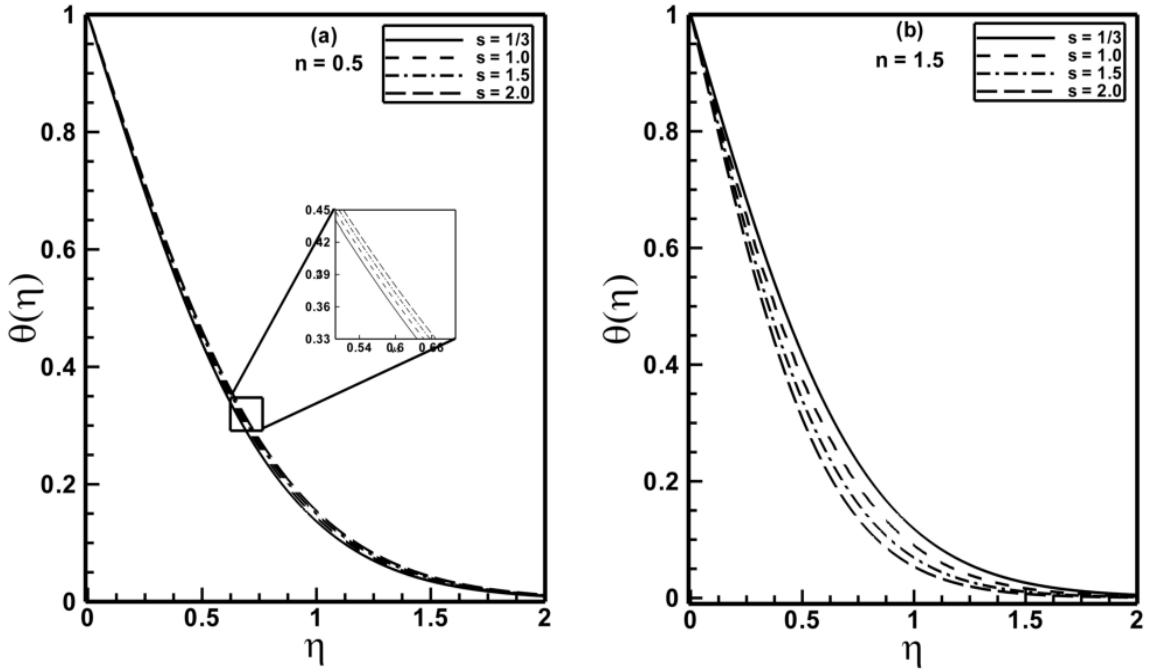

Figure 4.6: The temperature profile $\theta(\eta)$ for different values of the stretching parameter s when $A=1.5,\ \Pr=2.0,\ Ec=0.1$ and $Br=0.1$ are fixed.

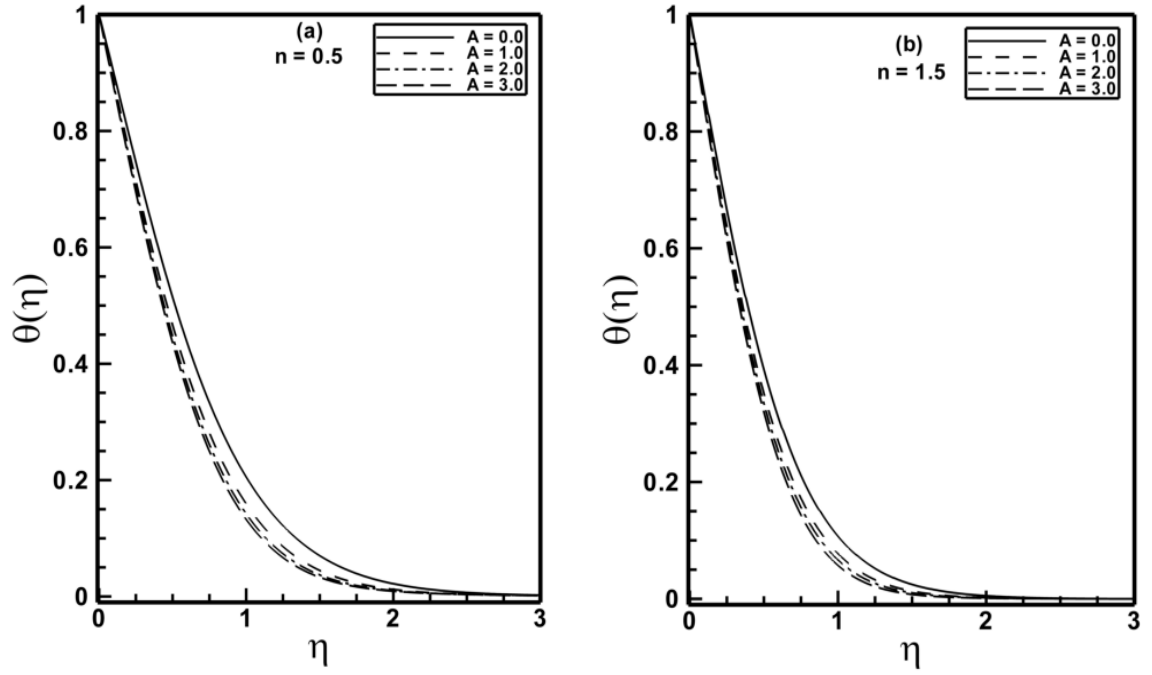

Figure 4.7: The temperature profile $\theta(\eta)$ for different values of the material parameter A when $s=1.5,\ \Pr=2.0,\ Ec=0.1$ and $Br=0.1$ are fixed.

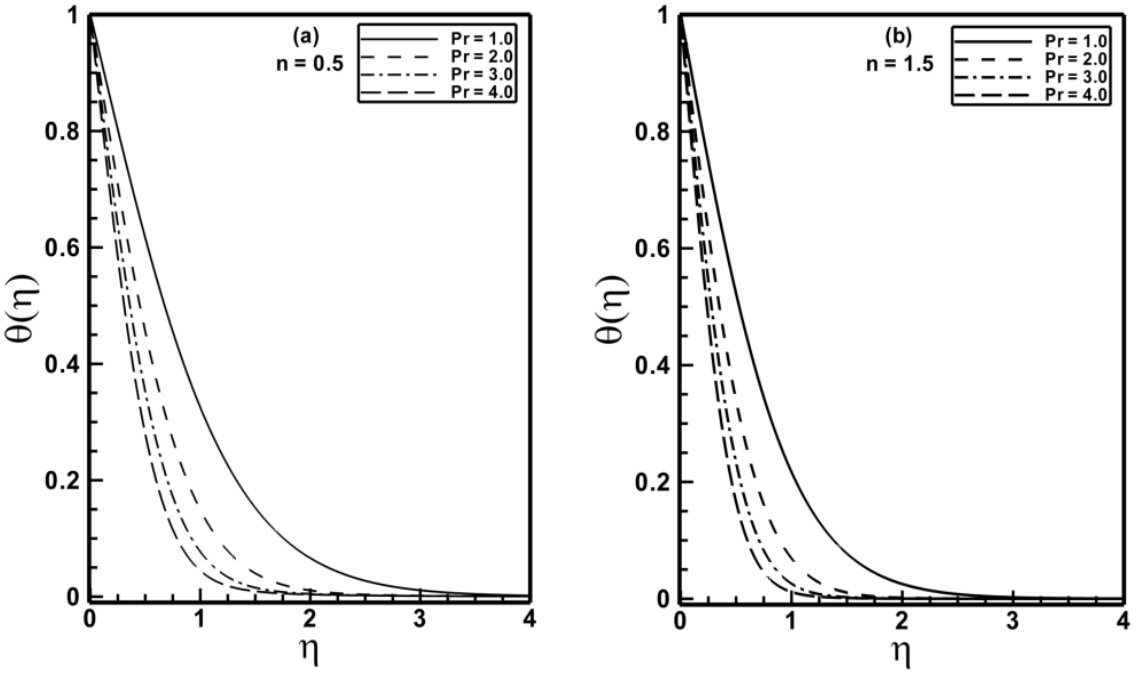

Figure 4.8: Temperature profile $\theta(\eta)$ for different values of the Prandtl number Pr when $s = A = 1.5$ and $Ec = Br = 0.1$ are fixed.

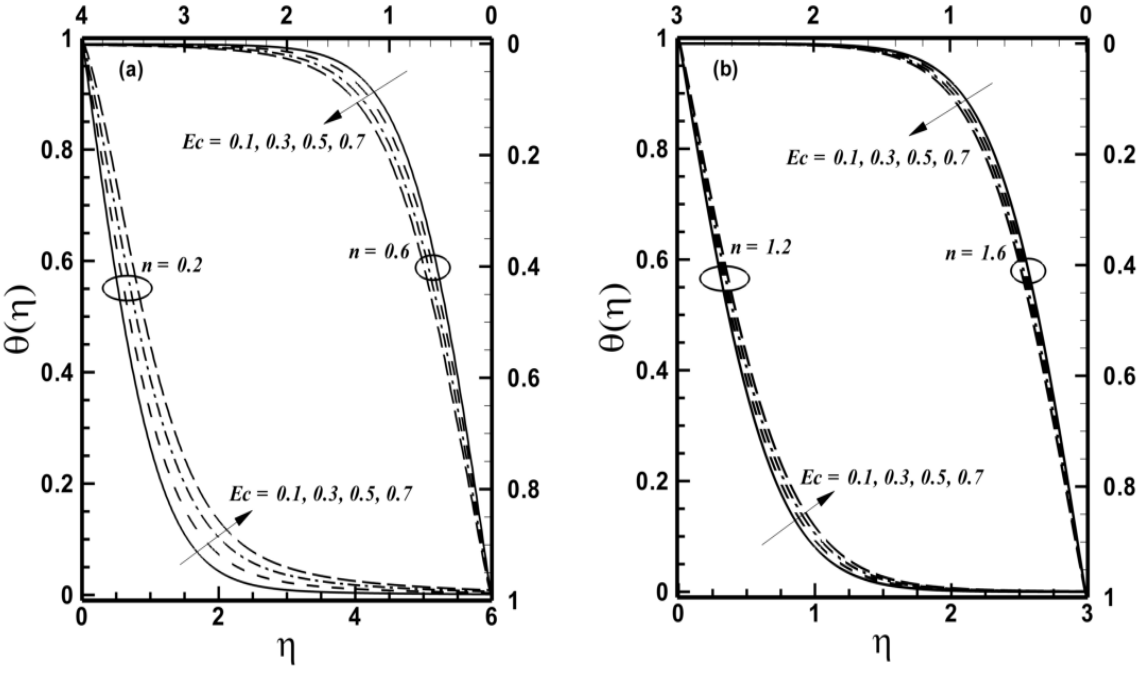

Figure 4.9: Temperature profiles $\theta(\eta)$ for different values of the Eckert number Ec when $s = 1.5$, $A = 1.5$, $Br = 0.1$ and $Pr = 2.0$ are fixed.

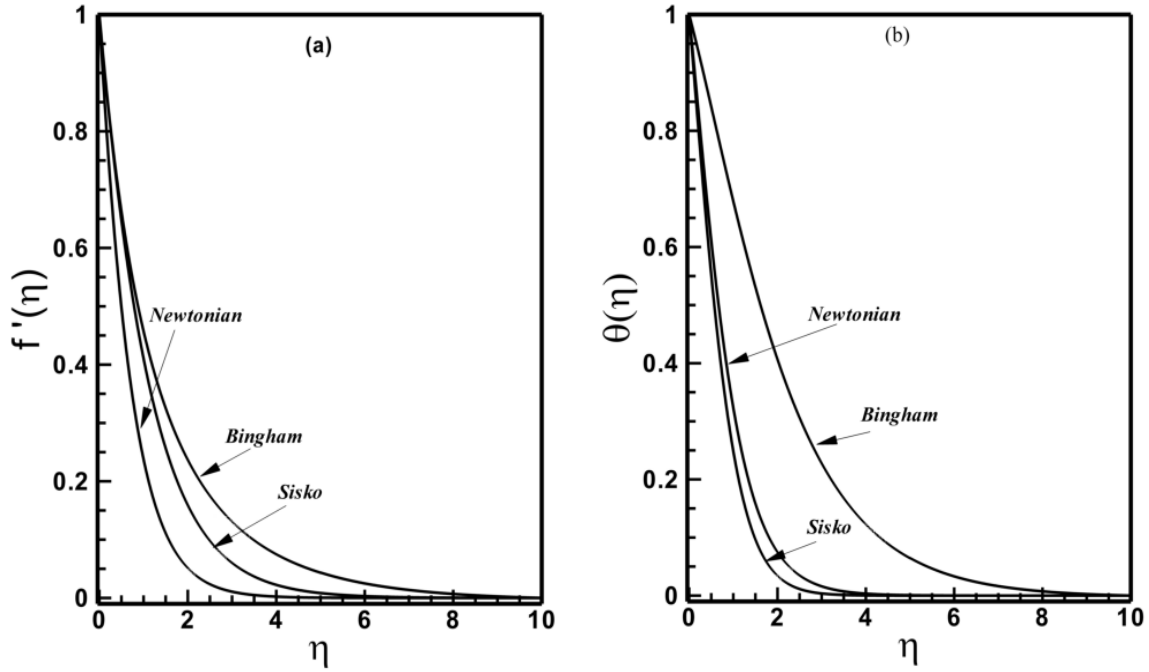

Figure 4.10: A comparison amongst the velocity and temperature profiles for different fluids when $s = 1.5,\ Ec = 0.1,\ Br = 0.1$ and $Pr = 2.0$ are fixed.

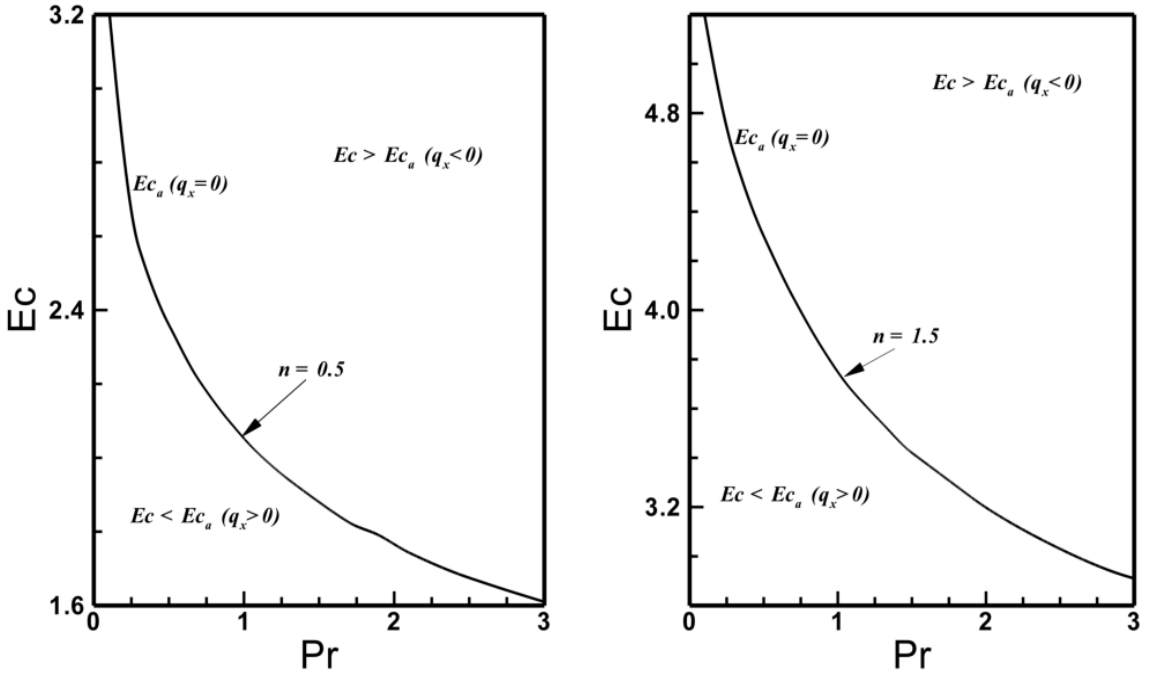

Figure 4.11: Adiabatic Eckert number Ec_a with variation of Prandtl number Pr when $s = 1.5,\ Br = 0.1$ and $A = 1.5$ are fixed.

Table 4.1: A tabulation of the local skin friction coefficient, in terms of the comparison between the present numerical results and the HAM results (Ref. [25])

		$\frac{1}{2}\mathrm{Re}_b^{\frac{1}{n+1}} C_f$			
		$n=1$		$n=2$	
A	s	*Numerical results*	*HAM results*	*Numerical results*	*HAM results*
0	1	-1.173721	-1.173721	-1.189598	-1.189567
1	1	-1.659892	-1.659891	-1.605002	-1.605010
2	1	-2.032953	-2.032945	-1.973087	-1.973092
3	1	-2.347441	-2.347451	-2.297733	-2.297713
1	2	-2.090755	-2.090753	-2.152145	-2.152153
1	3	-2.449490	-2.449491	-2.621176	-2.621182

Table 4.2: A tabulation of the local skin friction and the local Nusselt number when $\mathrm{Pr}=2$.

				$n=0.5$		$n=1.5$	
A	s	Ec	Br	$\frac{1}{2}\mathrm{Re}_b^{\frac{1}{n+1}} C_f$	$\mathrm{Re}_b^{\frac{-1}{n+1}} Nu_r$	$\frac{1}{2}\mathrm{Re}_b^{\frac{1}{n+1}} C_f$	$\mathrm{Re}_b^{\frac{-1}{n+1}} Nu_r$
1.0	1.0	0.1	0.1	-1.73805	-1.17739	-1.62676	-1.39104
2.0	1.0	0.1	0.1	-2.11629	-1.23316	-2.00146	-1.45209
3.0	1.0	0.1	0.1	-2.42731	-1.26482	-2.33186	-1.48665
1.0	2.0	0.1	0.1	-2.07515	-1.12583	-2.12359	-1.60519
2.0	2.0	0.1	0.1	-2.54479	-1.19159	-2.58828	-1.67792
3.0	2.0	0.1	0.1	-2.92852	-1.22886	-2.99557	-1.72052
1.5	1.5	0.1	0.1	-2.14094	-1.18612	-2.10705	-1.54061
1.5	1.5	0.3	0.1	-2.14094	-1.04343	-2.10705	-1.44104
1.5	1.5	0.5	0.1	-2.14094	-0.90074	-2.10705	-1.34148
1.5	1.5	0.5	0.5	-	-0.79979	-	-1.21802
1.5	1.5	0.5	1.0	-	-0.67123	-	-1.06372
1.5	1.5	0.5	2.0	-	-0.41411	-	-0.75508

Table 4.3: A tabulation of the local Nusselt number for different values of Prandtl number when $s = 1.5$, $A = 1.5$, $Ec = 0.1$ and $Br = 0.1$. are fixed.

	$\mathrm{Re}_b^{\frac{-1}{n+1}} Nu_r$	
Pr	$n = 0.5$	$n = 1.5$
1	-0.78918	-1.01961
2	-1.18612	-1.54061
3	-1.48757	-1.93536
4	-1.73972	-2.26569
5	-1.96052	-2.55523

Table 4.4: The numerical values of the Local Nusselt when $s = 1.5$, $Ec = Br = 0$ and $\mathrm{Pr} = 2$ are fixed.

	$\mathrm{Re}_b^{\frac{-1}{n+1}} Nu_r$	
A	$n = 0.5$	$n = 1.5$
1	-1.26056	-1.59810
2	-1.30002	-1.63853
3	-1.32225	-1.66282

Chapter 5

Convective Heat Transfer to Sisko Fluid over a Wedge with Viscous Dissipation

This chapter analyzes the convective flow of Sisko fluid past a wedge under the variable free stream velocity in the presence of viscous dissipation effects. Flow past a wedge yields different pressure profiles for each of the wedge angle, thereby offering insight into boundary layer behavior for number of situations. The effects of shear thinning and shear thickening on flow and heat transfer are explored in depth. The influence of the wedge angle parameter on flow and heat transfer is spanned from stagnation point down through flat plate flow to the separation point. Employing the suitable transformations the governing equations are converted to a system of nonlinear ordinary differential equations. The resulting equations are then solved numerically by implicit finite difference method along with Keller box scheme in the domain $[0,\infty)$. The numerical results for the velocity and temperature fields are graphically presented and effects of the various parameters are discussed in detail. In addition, the displacement thickness, momentum thickness, skin-friction coefficient and local Nusselt number for different values of the pressure gradient parameter are calculated in tabulated form. Also, the present results are compared with the previously published work with an outstanding accuracy.

5.1 Geometry of the Problem

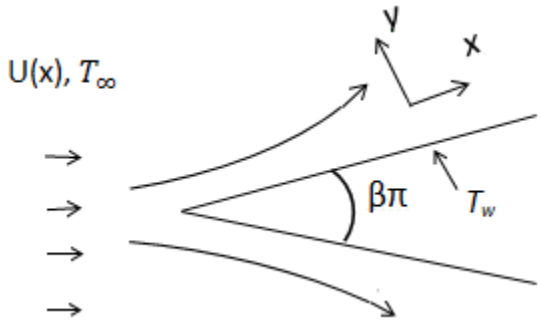

Figure 5.1: Physical model and coordinate system.

5.2 Mathematical Formulation

5.2.1 Flow and Heat Transfer Analysis

Let us consider the steady two-dimensional forced convection boundary layer flow of an incompressible Sisko fluid with temperature T_∞ moving over the surface of a wedge with a velocity $U(x) = cx^s$ (see figure 5.1). Here $c > 0$ is an arbitrary constant and the exponent s, a function of the wedge angle parameter β are related by $\beta = \frac{2s}{s+1}$. The steady motion of the Sisko fluid in Cartesian coordinate system is governed by the conservation laws of momentum and mass, which is presented in Eqs. (3.1) and (3.2). Through Eq. (3.5) the extra stress tensor $\mathbf{S}$ for Sisko fluid is related to the fluid motion. For the steady two-dimensional flow, the velocity, temperature and stress fields are given by Eq. (3.8). The boundary layer governing equations of mass, momentum and energy, neglecting heat generation, for the flow problem are, in the usual notation, (cf. Chapter 3)

$$\frac{\partial u}{\partial x} + \frac{\partial v}{\partial y} = 0, \tag{5.1}$$

$$\rho\left(u\frac{\partial u}{\partial x}+v\frac{\partial u}{\partial y}\right)=U\frac{dU}{dx}+a\frac{\partial^2 u}{\partial y^2}+b\frac{\partial}{\partial y}\left(\frac{\partial u}{\partial y}\right)^n, \tag{5.2}$$

$$u\frac{\partial T}{\partial x}+v\frac{\partial T}{\partial y}=\frac{\kappa}{\rho c_p}\frac{\partial^2 T}{\partial y^2}+\frac{1}{\rho c_p}\left[a\left(\frac{\partial u}{\partial y}\right)^2+b\left(\frac{\partial u}{\partial y}\right)^{n+1}\right]. \tag{5.3}$$

The boundary conditions are

$$u=0,\ v=0 \text{ and } T=T_w \text{ at } y=0, \tag{5.4}$$

$$u=U(x)=cx^s \text{ and } T\to T_\infty \text{ as } y\to+\infty. \tag{5.5}$$

Here x and y are, respectively, the distances along and perpendicular to the surface of the wedge, u and v the velocity components along x - and y - directions, respectively, $T(x,y)$ the temperature field, a, b, n $(n\geq 0)$ the material constants, with c_p as the specific heat of fluid at constant pressure and κ the thermal conductivity.

We look for solutions of Eqs. (5.2) and (5.3) with boundary conditions (5.4) and (5.5) using the transformations of the following form (cf. Chapter 3)

$$\eta=\frac{y}{x}\mathrm{Re}_b^{\frac{1}{n+1}},\ \psi(x,y)=xU\,\mathrm{Re}_b^{\frac{-1}{n+1}}f(\eta) \text{ and } \theta(\eta)=\frac{T-T_\infty}{T_w-T_\infty}. \tag{5.6}$$

On substituting Eq. (5.6) into Eqs. (5.2) to (5.5) we get

$$Af'''+n\left[f''\right]^{n-1}f'''+\frac{2}{n+1}\left[(n-1)\beta+1\right]ff''-\beta\left[(f')^2-1\right]=0, \tag{5.7}$$

$$\theta''+\mathrm{Pr}\frac{\beta(2n-1)+(2-\beta)}{(2-\beta)(n+1)}f\theta'+Br(f'')^2+\mathrm{Pr}\,Ec(f'')^{n+1}=0, \tag{5.8}$$

$$f(0)=0,\ f'(0)=0,\ \theta(0)=1, \tag{5.9}$$

$$f'(\eta)\to 1 \text{ and } \theta(\eta)\to 0 \text{ as } \eta\to\infty, \tag{5.10}$$

where prime denotes the differentiation with respect to η and the dimensionless quantities are defined by

$$\mathrm{Re}_a=\frac{s+1}{2}\frac{\rho xU}{a},\ \mathrm{Re}_b=\frac{s+1}{2}\frac{\rho x^n U^{2-n}}{b},\ A=\frac{\mathrm{Re}_b^{\frac{2}{n+1}}}{\mathrm{Re}_a} \text{ and } \mathrm{Pr}=\frac{xUR_b^{\frac{-2}{n+1}}}{\alpha}. \tag{5.11}$$

5.2.2 Important Physical Parameters

The physical quantities of main interest are the displacement thickness, momentum thickness, skin-friction coefficient and local Nusselt number.

Displacement thickness

The displacement thickness denoted by δ^* is a measure of the distance through which stream lines just outside boundary layer are displaced by action of viscosity inside the boundary layer and mathematically defined as

$$\delta^* = \int_0^\infty \left(1 - \frac{u}{U}\right) dy. \tag{5.12}$$

In non-dimensional form it can be written as

$$\delta_1 = \frac{\delta^*}{x\,\mathrm{Re}_b^{1/n+1}} = \int_0^\infty (1 - f')\, d\eta. \tag{5.13}$$

Momentum thickness

The momentum thickness denoted by θ^* is a measure of the loss of momentum inside the boundary as compared with the potential flow and is defined as

$$\theta^* = \int_0^\infty \left(1 - \frac{u}{U}\right) \frac{u}{U} dy. \tag{5.14}$$

Eq. (5.14) in non-dimensional form can be written as

$$\theta_1 = \frac{\theta^*}{x\,\mathrm{Re}_b^{1/n+1}} = \int_0^\infty (1 - f')\, f' d\eta. \tag{5.15}$$

The skin-friction coefficient

The skin-friction coefficient indicating shear stress at wall and in dimensionless form is

defined by

$$\frac{1}{2}\mathrm{Re}_b^{\frac{1}{n+1}} C_{fx} = \frac{s+1}{2}\left[Af''(0) + \left(f''(0) \right)^n \right]. \tag{5.16}$$

The Nusselt Number

The local Nusselt number denoted by Nu_x giving the rate of heat transfer at the wall and is defined by

$$Nu_x = \left. \frac{xq_w}{\kappa(T_w - T_\infty)} \right|_{y=0}, \tag{5.17}$$

where the wall heat flux is $q_w = -\kappa \left(\frac{\partial T}{\partial y} \right)\Big|_{y=0}$, which by virtue of Eq. (5.17) reduces to

$$\mathrm{Re}_b^{-1/n+1} Nu_x = -\theta'(0). \tag{5.18}$$

5.3 Numerical Method

The coupled Eqs. (5.7) and (5.8) are highly nonlinear ordinary differential equations. These equations are of third order in f and second order in θ, subject to boundary conditions (5.9) and (5.10), constitute a two-point boundary value problem. Although, exact solutions for complete set of equations are not possible, and hence we have solve this set of equations numerically by implicit finite difference scheme with Keller box method. The details of the numerical method are available in [66], only the salient features are recapitulated here. The coupled boundary value problem has been reduced to a system of five first order ordinary differential equations. Consequently, we have

$$f' = p, \tag{5.19}$$

$$p' = q, \tag{5.20}$$

$$Aq' + n(q)^{n-1}q' + \frac{2}{n+1}\left[(n-1)\beta + 1\right] fq - \beta(p^2 - 1) = 0, \tag{5.21}$$

$$\theta' = t, \tag{5.22}$$

$$t' + \Pr Ec(q)^{n+1} + \Pr \frac{\beta(2n-1) + (2-\beta)}{(2-\beta)(n+1)} ft + Brq^2 = 0. \tag{5.23}$$

The boundary conditions in terms new variable are written as

$$f(0) = 0,\ p(0) = 0 \text{ and } \theta(0) = 1, \tag{5.24}$$

$$p \to 1 \text{ and } \theta \to 0 \text{ as } \eta \to \infty. \tag{5.25}$$

The functions and their derivatives are approximated by central difference at the mid-point $\eta_{j-1/2}$ of the segment $\eta_{j-1}\eta_j$, where $j = 1, 2 \ldots N$. The resulting set of nonlinear difference equations are linearized using the Newton's quasi-linearization technique and are solved using a block-tridiagonal algorithm [66]. For the calculations step size of 0.001 was considered. The iterative procedure is stopped when the difference in computing the velocity and the temperature in the next iteration is less than 10^{-5}. The present method is unconditionally stable and has second-order accuracy.

5.4 Numerical Results and Discussion

Before we ensue the presentation and discussion of results obtained in current chapter it is worthy to validate the reliability of the presently computed numerical results by comparing them with the previously published relevant literature. Table 5.1 compares several sets of values of displacement thickness and momentum thickness with those of previous investigations as a special case of the problem. The comparison shows a very good agreement with the results reported by White [74]. This leads confidence in the numerical results reported in this chapter.

The present chapter primarily aims the flow and heat transfer characteristics of a

Sisko fluid past a wedge with a power-law free stream velocity. To comprehend the flow and heat transfer, Eqs. (5.7) and (5.8) with boundary conditions (5.9) and (5.10) are solved numerically for non-integer values of the power-law index n and wedge angle parameter β and results are illustrated graphically. To investigate the flow and heat transfer characteristics within the boundary layer, various parameters like non-dimensional displacement thickness, momentum thickness, local skin friction coefficient and local Nusselt number are also studied.

Figure 5.2 presents the effect of the wedge angle parameter β on velocity profile for shear thinning and shear thickening regimes. It is evident from figure 5.2(a) that the favorable pressure gradient $(\beta > 0)$ produces thin momentum boundary layer as compared to flow over a flat plate $(\beta = 0)$. On the other hand, an adverse pressure gradient $(\beta < 0)$ produces the thicker one. A comparison of these figures reveals that the momentum boundary layer is more sensitive to the value of pressure gradient parameter β for shear thickening regime $(n > 1)$ than that of shear thinning regime $(n < 1)$.

Some temperature profiles for different values of the wedge angle parameter β are sketched in figure 5.3. The temperature and the corresponding thermal boundary layer thickness increase from favorable to adverse pressure gradient. However, for shear thickening fluid the temperature profile is more sensitive to the value of β. Further, the temperature gradient at the wall is much dependent upon the value of β for $n = 1.5$ as compared to $n = 0.5$.

Figure 5.4 displays the non-dimensional tangential stress profile $\frac{\tau_{yx}}{\frac{1}{2}\rho U^2} = Af''(\eta) + [f''(\eta)]^n$, for some values of the wedge angle parameter β for shear

thinning and thickening regimes. Figure 5.4(a) shows that the shear falls away from the wall for positive values of β and it rise from the wall for negative values of β. This is a consequence of momentum equation condition $\partial\tau/\partial y\big|_{y=0}$, that in turn depends upon pressure gradient. A comparison of these figures reveals that the shear is higher near the wall for shear thinning fluid $(n<1)$ as compare to the shear thickening fluid $(n>1)$.

The effects of β on the local skin friction coefficient and local Nusselt number are shown in figure 5.5. The skin-friction coefficient for shear thinning and shear thickening fluids increase as the value of β is incremented progressively. Further, this figure depicts the trend in the value of local Nusselt number for $n=0.5$ and $n=1.5$. For the power law index $n=0.5$, the local Nusselt number is not largely affected by the variation in value of β. However, a sharp rise in local Nusselt number is observed for values of β beyond 1.5 when the power-law index $n=1.5$.

Eckert number (Ec) measures the transformation of kinetic energy into heat by viscous dissipation. The variation of temperature with increasing Ec is given in figures 5.6(a,b). Figure 5.6(a) describes the effect of increasing Ec on highly shear thinning $n=0.2$ and moderately shear thinning $n=0.6$ Sisko fluids. This figure clearly elucidates that the temperature profile increases with increasing Ec. Further the strongly shear thinning fluids are greatly affected by Ec as compared to that of the moderately shear thinning fluids. Figure 5.6(b) describes the same phenomenon for shear thickening regime $(n>1)$, but here the effects of Ec are not dominant as those of the shear thinning regime $(n>1)$.

Table 5.2 summarizes the trend in displacement thickness θ_1 and momentum thickness δ_1. From this table it is noted that both increase with each decrement in the value of the wedge angle parameter β.

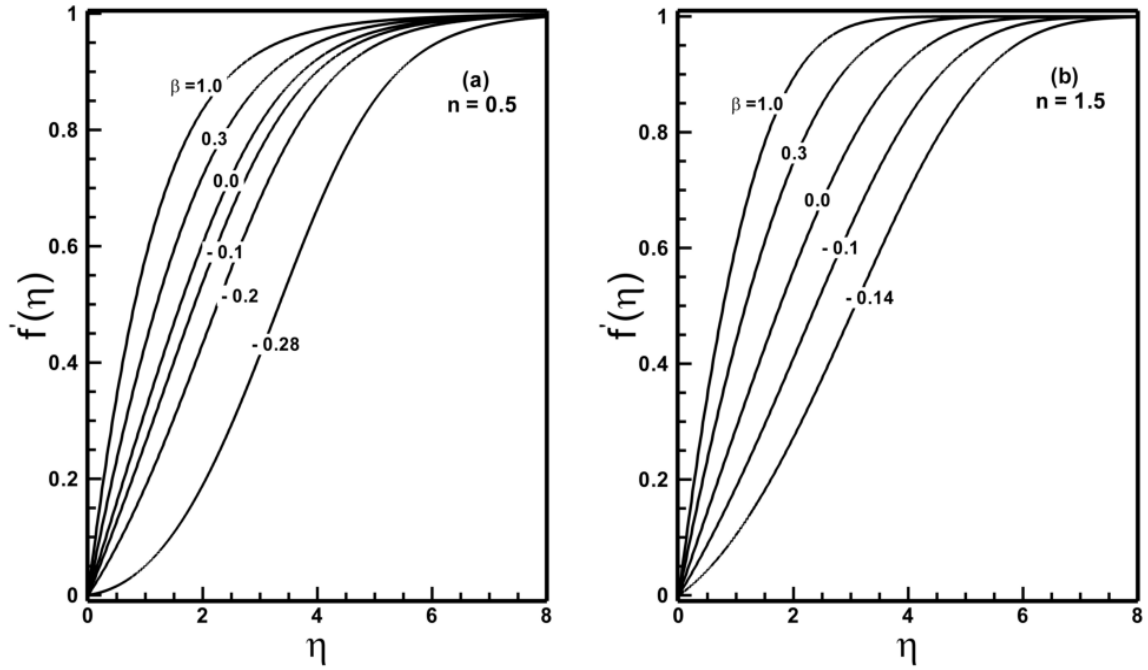

Figure 5.2: Profiles of the velocity $f'(\eta)$ for different values of the wedge angle parameter β when $A=1.5$ is fixed.

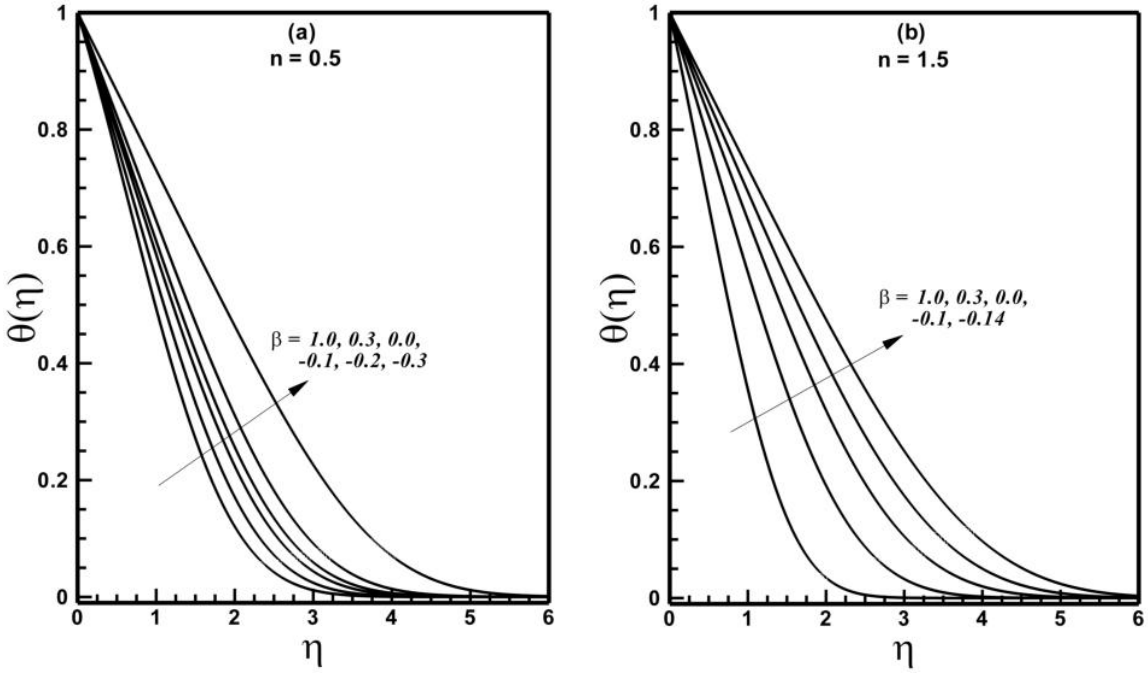

Figure 5.3: Profiles of the temperature $\theta(\eta)$ for different values of the wedge angle parameter β when $Br=0.1$, $Ec=0.1, \Pr=2.0$ and $A=1.5$ are fixed.

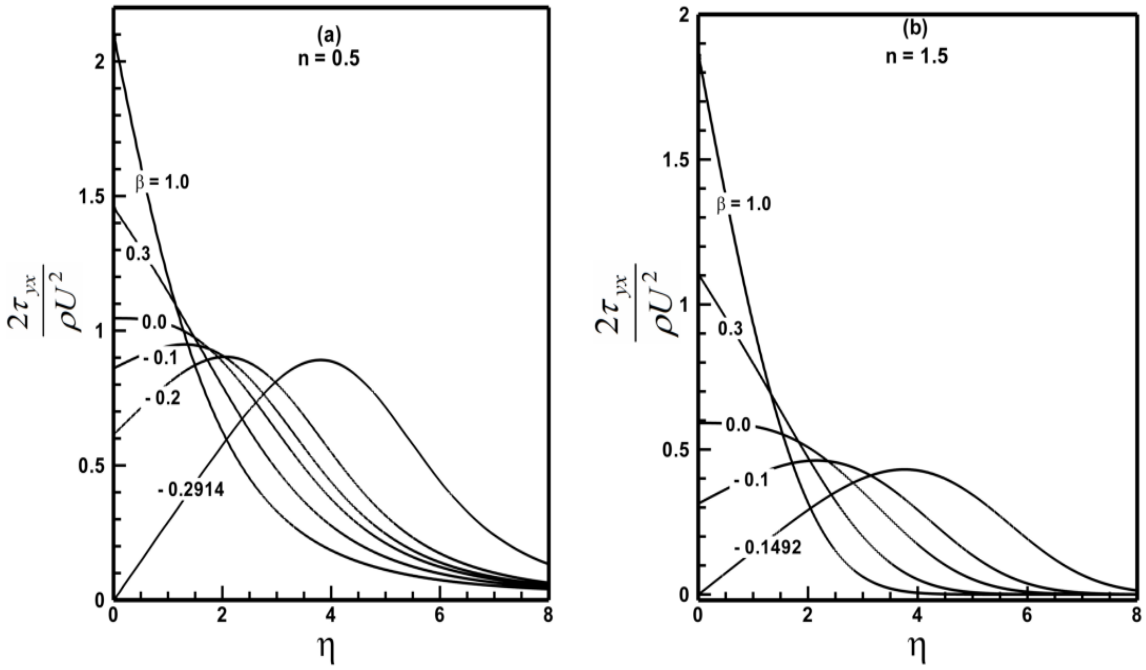

Figure 5.4: Profiles of the non-dimensional tangential stress $\frac{\tau_{yx}}{\frac{1}{2}\rho U^2}$ for different values of the wedge angle parameter β when $A=1.0$ is fixed.

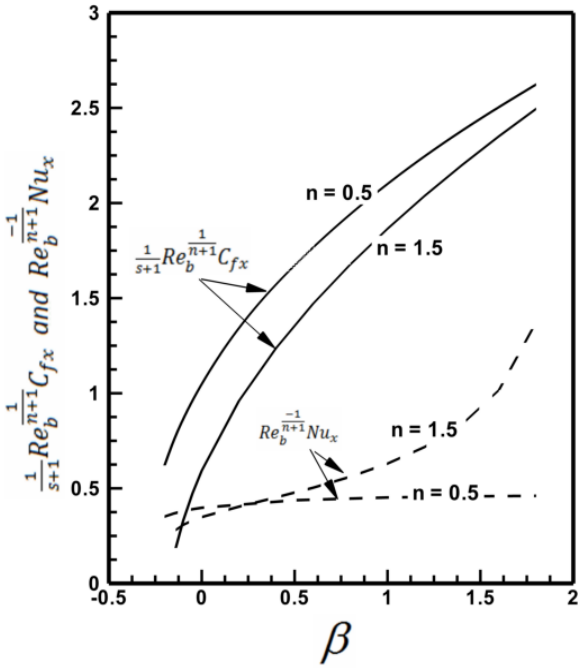

Figure 5.5: Variation of the skin-friction coefficient and local Nusselt number with β for different values of the power-law index when $Ec=0.1$, $Br=0.1$, $\Pr=2.0$ and $A=1.0$ are fixed.

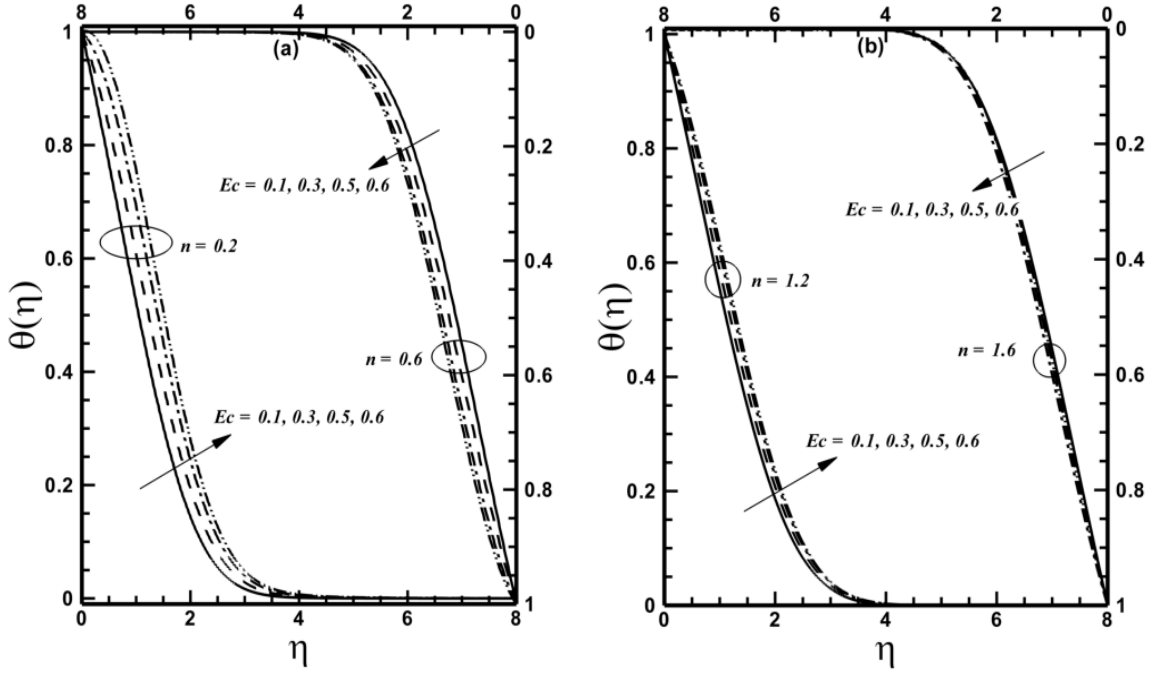

Figure 5.6: Profiles of the temperature $\theta(\eta)$ for different values of the Eckert number Ec when $\beta = 0.3$, $Br = 0.1$, $\Pr = 2.0$ and $A = 1.5$ are fixed.

Table 5.1: A comparison of displacement thickness (δ_1) and momentum thickness (θ_1) when $n=1$ and $A=0.$

Ref. [74]			Present study	
β	δ_1	θ_1	δ_1	θ_1
-0.18	1.87157	0.56771	1.87154	0.56757
0.00	1.21678	0.46960	1.21668	0.46959
0.30	0.91099	0.38574	0.91099	0.38573
1.00	0.64790	0.29235	0.64791	0.29234
10.0	0.24077	0.11523	0.24077	0.11522

Table 5.2: A tabulation of the displacement thickness (δ_1) and momentum thickness (θ_1) when $A=1.5$.

n = 0.5			*n=1.5*	
β	δ_1	θ_1	δ_1	θ_1
1.00	1.12592	0.54514	0.85324	0.36641
0.30	1.51201	0.67182	1.21445	0.49869
0.00	1.86736	0.75194	1.70663	0.64317
-0.10	2.08502	0.79238	2.17926	0.73927
-0.20	2.44345	0.83971	-	-

Chapter 6

Mixed Convection Heat Transfer in Sisko Fluid: Effects of Assisting and Opposing Buoyancy

Steady mixed convection heat transfer in Sisko fluid over a vertically stretching surface is considered in this chapter when the imposed and buoyancy induced flows are in same and opposite directions. The flow is induced due to nonlinear stretching sheet with constant temperature distribution. The governing partial differential equations, under framework of the Boussinesq approximation are transformed into ordinary differential equations using a suitable transformation. These equations are solved numerically using implicit finite difference method with Keller box scheme for the following ranges of parameters: the buoyancy parameter $(-3.0 \le \lambda \le 2.0)$, the power-law index $(0.3 \le n \le 1.9)$, the material parameter of Sisko fluid $(0.2 \le A \le 1.9)$. In particular, the effects of these dimensionless parameters on the velocity and temperature fields, the skin friction coefficient, and the local Nusselt numbers have been graphically sketched. In addition, the numerical results are validated by comparison with analytic results as well as previously published results as a special case of the problem.

6.1 Geometry of the problem

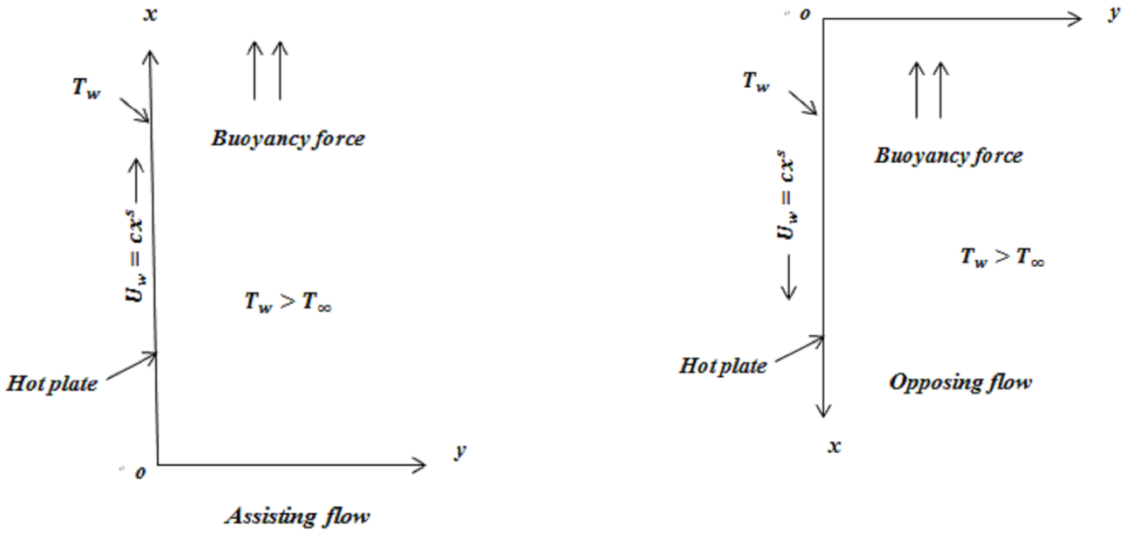

Figure 6.1: Flow geometry and coordinate system.

6.2 Mathematical Formulation of the Problem

Consider the steady two-dimensional flow of an incompressible Sisko fluid over a vertically stretching sheet maintained at a constant temperature T_w, while T_∞ is the constant ambient fluid temperature. The continuous stretching surface is assumed to have velocity $U_w(x) = cx^s$, where c and s are positive real numbers. For homogeneous and incompressible fluid, the continuity equation is expressed by the solenoidal condition given by Eq. (3.1). The motion of fluid governed by conservation law of linear momentum and energy is given by Eqs. (3.2) and (3.3). The extra stress tensor $\mathbf{S}$ for an incompressible Sisko fluid has the form given in Eq. (3.5). On the basis of boundary layer assumptions and the Boussinesq approximation, a mixed convective flow in Cartesian coordinate system can be described by the partial differential equations (cf. Chapter 3)

$$\frac{\partial u}{\partial x} + \frac{\partial v}{\partial y} = 0, \tag{6.1}$$

$$\rho\left(u\frac{\partial u}{\partial x}+v\frac{\partial u}{\partial y}\right)=a\frac{\partial^2 u}{\partial y^2}-b\frac{\partial}{\partial y}\left(-\frac{\partial u}{\partial y}\right)^n\pm g\beta(T-T_\infty), \tag{6.2}$$

$$u\frac{\partial T}{\partial x}+v\frac{\partial T}{\partial y}=\frac{\kappa}{\rho c_p}\frac{\partial^2 T}{\partial y^2}, \tag{6.3}$$

subject to the boundary conditions

$$u=U_w(x)=cx^s,\ v=0 \text{ and } T=T_w \text{ at } y=0, \tag{6.4}$$

$$u\to 0 \text{ and } T\to T_\infty \text{ as } y\to+\infty. \tag{6.5}$$

The x- and y- axes are along and perpendicular to the sheet, respectively, (u,v) the velocity components along x-and y-directions, $T(x,y)$ the temperature field, a, b, n (≥ 0) the material constants, with c_p as the specific heat of fluid at constant pressure and κ the thermal conductivity. The last term on the right-hand sides of Eqs. (6.2) represent the buoyancy force. The plus and minus signs in Eq. (6.2) refer to assisting and opposing flows, respectively.

Introducing stream function $\psi(x,y)$, variable η and dimensionless temperature $\theta(\eta)$ as (cf. Chapter 3)

$$\eta=\frac{y}{x}\mathrm{Re}_b^{\frac{1}{n+1}},\ \psi(x,y)=xU\,\mathrm{Re}_b^{\frac{-1}{n+1}}f(\eta) \text{ and } \theta(\eta)=\frac{T-T_\infty}{T_w-T_\infty}. \tag{6.6}$$

The velocity components are defined as

$$u=\frac{\partial\psi}{\partial y} \text{ and } v=-\frac{\partial\psi}{\partial x}. \tag{6.7}$$

On substituting Eq. (6.6) into Eqs. (6.2) to (6.5), finally the following set of equations results in

$$Af'''+n(-f'')^{n-1}f'''+\frac{s(2n-1)+1}{n+1}ff''-s(f')^2+\lambda\theta=0, \tag{6.8}$$

$$\theta''+\mathrm{Pr}\frac{s(2n-1)+1}{(n+1)}f\theta'=0, \tag{6.9}$$

$$f(0)=0,\ f'(0)=1,\ \theta(0)=1, \tag{6.10}$$

$$f'(\eta)\to 0 \text{ and } \theta(\eta)\to 0 \text{ as } \eta\to\infty, \tag{6.11}$$

where prime denotes the differentiation with respect to η, Re_a, Re_b are the local Reynolds number, A the material parameter of Sisko fluid and Pr the generalized Prandtl number, which are defined by

$$\mathrm{Re}_a=\frac{\rho x U}{a},\ \mathrm{Re}_b=\frac{\rho x^n U^{2-n}}{b},\ A=\frac{\mathrm{Re}_b^{\frac{-2}{n+1}}}{\mathrm{Re}_a} \text{ and } \mathrm{Pr}=\frac{xUR_b^{\frac{-2}{n+1}}}{\alpha}. \tag{6.12}$$

The importance of mixed convection flow is measured by the buoyancy parameter $\lambda=\frac{\mathrm{Gr}}{\mathrm{Re}_a^2}$, where $Gr=\frac{g\beta(T-T_\infty)x^3\rho^2}{a^2}$ is the local Grashof number. The assisting buoyancy arises when $\lambda>0$ and $\lambda<0$ represents the opposing buoyancy flow situation. It is worth mentioning that in the limit $\lambda\to 0$ the heat transfer primarily occurs by forced convection, and when $\lambda\to\infty$ purely by free convection.

The local skin-friction coefficient C_{fx} and the local Nusselt number Nu_x are defined as follows:

$$C_{fx}=\frac{2\tau_w\big|_{y=0}}{\rho U_w^2},\ Nu_x=\frac{x q_w\big|_{y=0}}{\kappa(T_w-T_\infty)}, \tag{6.13}$$

where $\tau_w=\left(a\frac{\partial u}{\partial y}+b\frac{\partial u}{\partial y}\left|\frac{\partial u}{\partial y}\right|^{n-1}\right)$ and $q_w=-\kappa\left(\frac{\partial T}{\partial y}\right)$. In view of Eq. (6.6) the shear stress at wall and the local Nusselt number in dimensionless form are given by

$$\frac{1}{2}\mathrm{Re}_b^{\frac{1}{n+1}}C_{fx}=Af''(0)-\left[-f''(0)\right]^n \text{ and } \mathrm{Re}_b^{-1/n+1}Nu_x=-\theta'(0). \tag{6.14}$$

6.3. Solution Methodologies

6.3.1 Implicit Finite Difference Method

The transformed boundary layer Eqs. (6.8) to (6.11) constituting a two-point boundary value problem are solved numerically using the implicit finite difference method with Keller box scheme. This scheme is implemented by writing Eqs. (6.8) and (6.9) as an equivalent first order system as follows:

$$f' = p, \tag{6.15}$$

$$p' = q, \tag{6.16}$$

$$\theta' = t, \tag{6.17}$$

$$Aq' + n(q)^{n-1}q' + \frac{s(2n-1)+1}{n+1} fq - sp^2 + \lambda\theta = 0, \tag{6.18}$$

$$t' + \Pr\frac{s(2n-1)+1}{n+1} ft = 0. \tag{6.19}$$

The corresponding boundary conditions are

$$f(0) = 0,\ p(0) = 1 \text{ and } \theta(0) = 1, \tag{6.20}$$

$$p \to 0,\ \theta \to 0 \text{ as } \eta \to \infty. \tag{6.21}$$

The details of this method are available in [66]; however, only the main features are precisely enumerated here. The functions and their derivatives are approximated by central difference at the mid-point $\eta_{j-1/2}$ of the segment $\eta_{j-1}\eta_j$, where $j = 1, 2 \ldots N$. The resulting set of nonlinear difference equations are linearized using the Newton's quasi-linearization technique and are solved using a block-tridiagonal algorithm [66]. The iterative procedure is terminated when the difference in computing the velocity and the temperature in the next iteration is less than 10^{-5}. The present method is unconditionally stable, has second-order accuracy, and fast convergence that reduce the computation time and memory usage.

6.3.2 Analytical Method

The system of nonlinear coupled ordinary differential equations (6.8) and (6.9) are also solved analytically with the boundary conditions (6.10) and (6.11) using the homotopy analysis method *(HAM)*. Analytical solutions are sought for certain values of the parameters with a view to check the veracity of our numerical results. To implement the HAM we choose the initial guesses satisfying the boundary values

$$f_0 = 1 - e^{-\eta} \text{ and } \theta_0 = e^{-\eta}, \tag{6.22}$$

and auxiliary linear operators

$$L_f = \frac{d^3}{d\eta^3} - \frac{d}{d\eta} \text{ and } L_\theta = \frac{d^2}{d\eta^2} - \frac{d}{d\eta}, \tag{6.23}$$

for the velocity and temperature fields, respectively.

The proper values of the convergence control parameters $\hbar_f$ and $\hbar_\theta$ assure the convergence of series solutions. The optimal values of these parameters are chosen by minimizing the discrete squared residual error [75].

6.4 Numerical Results and Discussion

To comprehend the flow and heat transfer, the coupled set ordinary differential equations (6.8) and (6.9) with boundary conditions (6.10) and (6.11) have been solved numerically. The results have been computed for values of the power-law index n in the range of $0.3 \le n \le 1.9$, thereby spanning the highly shear thinning and shear thickening regions, the buoyancy parameter λ in the range of $-3.0 \le \lambda \le 2.0$ focusing both assisting and opposing flows, the material parameter of the Sisko fluid ($0.2 \le A \le 1.9$).

Before we undertake the presentation and discussion of the computed results in this

study, it is worthy to validate the reliability and accuracy of the numerical algorithm used herein. It is accomplished by comparison of the present results with the literature values for a limiting case of the problem. Figure 6.2 presents this comparison between the numerical results of Ref. [38] and a special case of our problem, the agreement found perfect. Further, table 6.1 displays few results obtained analytically by the HAM and Keller box scheme, with excellent match. These comparisons inspire the confidence in the veracity of our numerical results.

Figures 6.3 to 6.10 present the graphical sketches of our numerical investigations. The representative velocity profiles for the shear thinning and shear thickening fluids with assisting and opposing buoyancy are shown in figure 6.3. On inspection of figure 6.3(a), it revealed that for shear thinning regime $(n<1)$ the velocity profile decreases with each increment in value of the power-law index n and it approaches the free stream conditions for smaller values of η. Figure 6.3(b) depicts the velocity profiles for the opposing buoyancy case and shows the same qualitative trends as in figure 6.3(a). However, quantitatively the velocity profile is lesser for each corresponding value of n.

It is worthy to delineate the effect of the buoyancy parameter on the temperature field. Some temperature profiles for different values of the power-law index n for assisting and opposing buoyancy forces are sketched in figure 6.4. From figure 6.4(a) it is observed that the temperature and the corresponding thermal boundary layer thickness decrease as the value of n is increased. As the behavior of fluid changes from shear thinning to shear thickening the profiles of temperature become more compact. In case of counterpart opposing buoyancy, the same qualitative trends are observed except the concomitant temperature slopes at the wall are smaller, thereby resulting in the lower heat transfer (figure 6.4b).

The skin friction coefficient C_{fx}, given by expression (6.14), as a function of the power-law index n is shown in figures 6.5, for several values of buoyancy parameter λ. For assisting flow and forced convection regime $(\lambda \geq 0)$ and opposing flow $(\lambda < 0)$, the results are shown in figures 6.5(a) and 6.5(b), respectively. Figure 6.5(a) shows that for forced convective mode the magnitude of C_{fx}, decreases as $n \to 1$ with variation in the power-law index n afterwards it becomes fairly constant. For a weaker buoyant force $\lambda = 0.2$, the same qualitative trend is observed. Whilst, for intermediate values of λ the magnitude of C_{fx} increases monotonically to a constant value. The figure further depicts that for a fixed value of n the magnitude of the skin friction coefficient diminishes as the value of buoyancy parameter is incremented. Figure 6.5(b) portrays that each curve primarily decreases with n, subsequently approaches to some constant value of C_{fx} Moreover, for a fixed value of n the magnitude of C_{fx} increases as the value of λ is traversed from weak opposing buoyant force to intermediately values.

The variation in local Nusselt number Nu_x with the power-law index n for assisting and opposing flow is illustrated in figures 6.6. It is obvious from these figures that the value of Nu_x improves as the value of n is incremented from highly shear thinning to shear thicken values. It is further evident that the effect of buoyancy is more pronounced for shear thinning fluids. It is also worth noting that for a fixed value of the power-law index there is an enhancement in Nu_x for assisting flow and contrary behavior is observed for opposing flow.

The effects of the material parameter A of Sisko fluid on the local skin friction coefficient C_{fx} for shear thinning and shear thickening fluids with assisting and opposing buoyancy effects are shown in figures 6.7 and 6.8. These figures manifest that the

magnitude of C_{fx} increases when A is incremented progressively. Further, for each fixed value of A the skin friction coefficient and hence the drag reduces for increasing assisting buoyancy force, whilst the contrary trends are observed for opposing flow regime. A careful observation of these figures reveal that the effect of the buoyancy parameter λ exerts a stronger influence for shear thinning fluid $(n = 0.5)$.

Lastly, it is useful to see the effects of the material parameter A of Sisko fluid on the local Nusselt number Nu_x for shear thinning and shear thickening fluids with assisting and opposing buoyancy effects (figures 6.9 and 6.10). These figures indicate that the value of Nu_x increases when A is incremented. Moreover, for each fixed value of A the local Nusselt number and hence the heat transfer at the wall increases for increasing assisting buoyancy force, whilst the opposing trends are observed for opposing flow regime. A careful observation of these figures reveals that the effect of the buoyancy parameter λ exerts a stronger influence for the shear thinning fluid $(n = 0.5)$.

Table 6.1: A comparison of the HAM and numerical results when $A=1.5,\ n=1.0,\ s=1.5$ and $\lambda=1$ are fixed.

	HAM results		Numerical results	
Pr	$f''(0)$	$\theta'(0)$	$f''(0)$	$\theta'(0)$
0.7	-0.513181	-0.624361	-0.513182	-0.625535
1.0	-0.541511	-0.763447	-0.541529	-0.764809
1.3	-0.560134	-0.875432	-0.561089	-0.885853

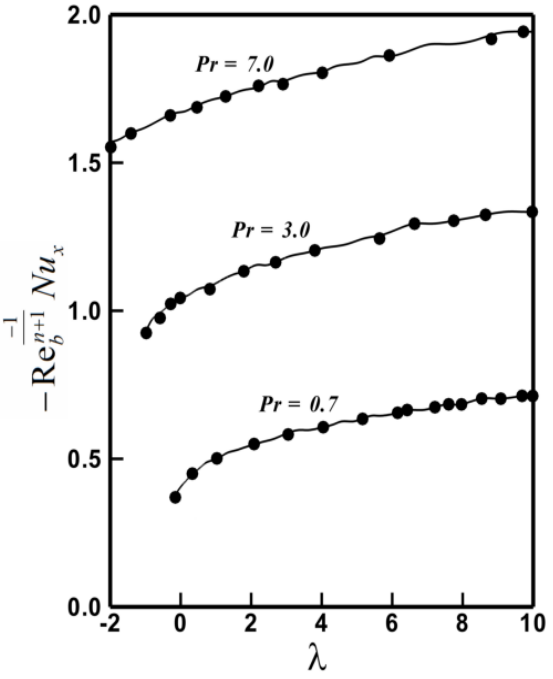

Figure 6.2: A comparison of present results (solid circles) with Ref. [38] (lines) when $s=0.5,\ n=1.0,$ and $A=0$ are fixed.

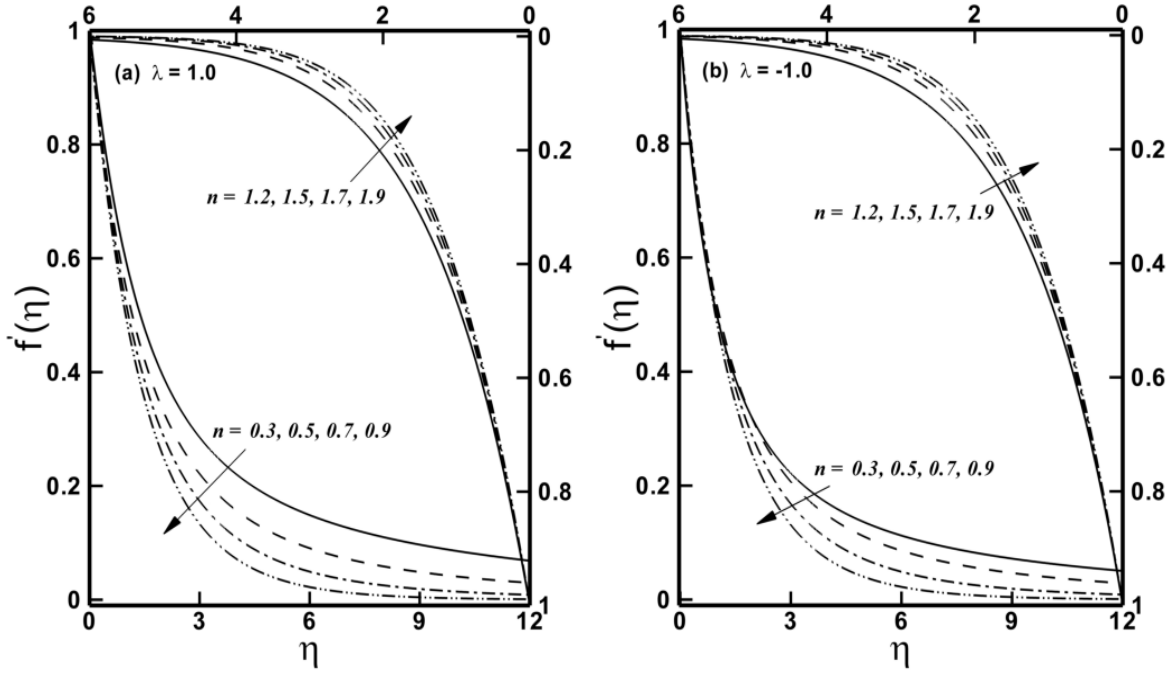

Figure 6.3: Profiles of the velocity $f'(\eta)$ for different values of the power-law index n for assisting and opposing flows when $s = A = 1.5$ and $\Pr = 100$ are fixed.

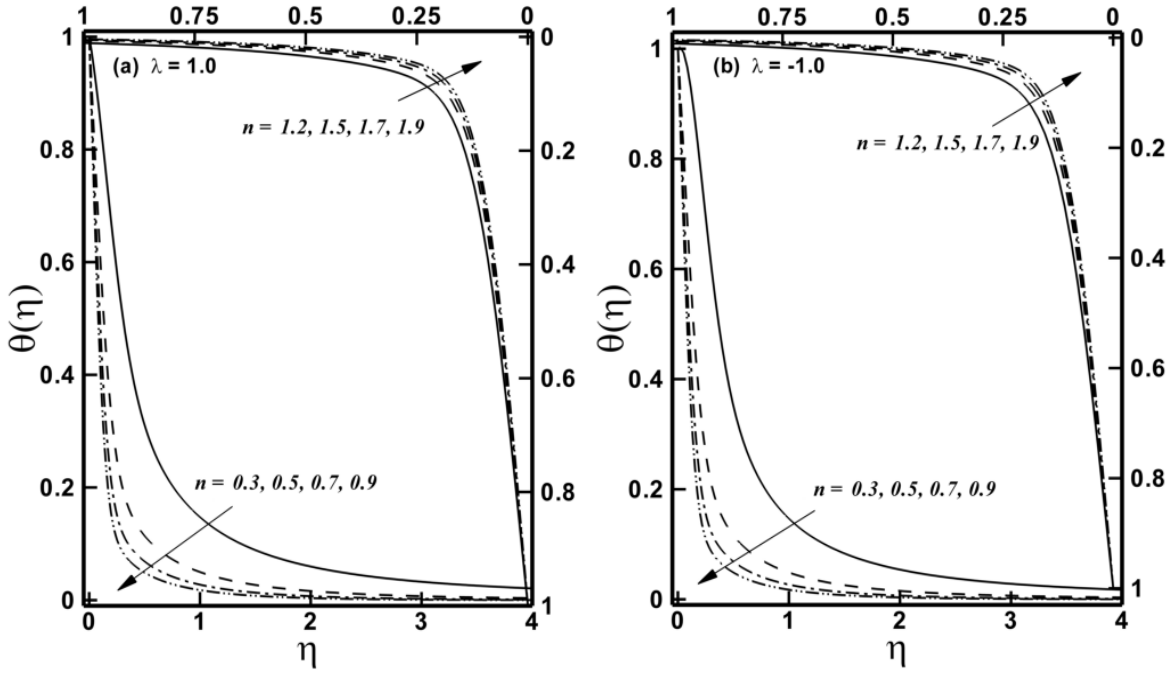

Figure 6.4: Profiles of the temperature $\theta(\eta)$ for different values of the power-law index n for assisting and opposing flows when $s = A = 1.5$ and $\Pr = 100$ are fixed.

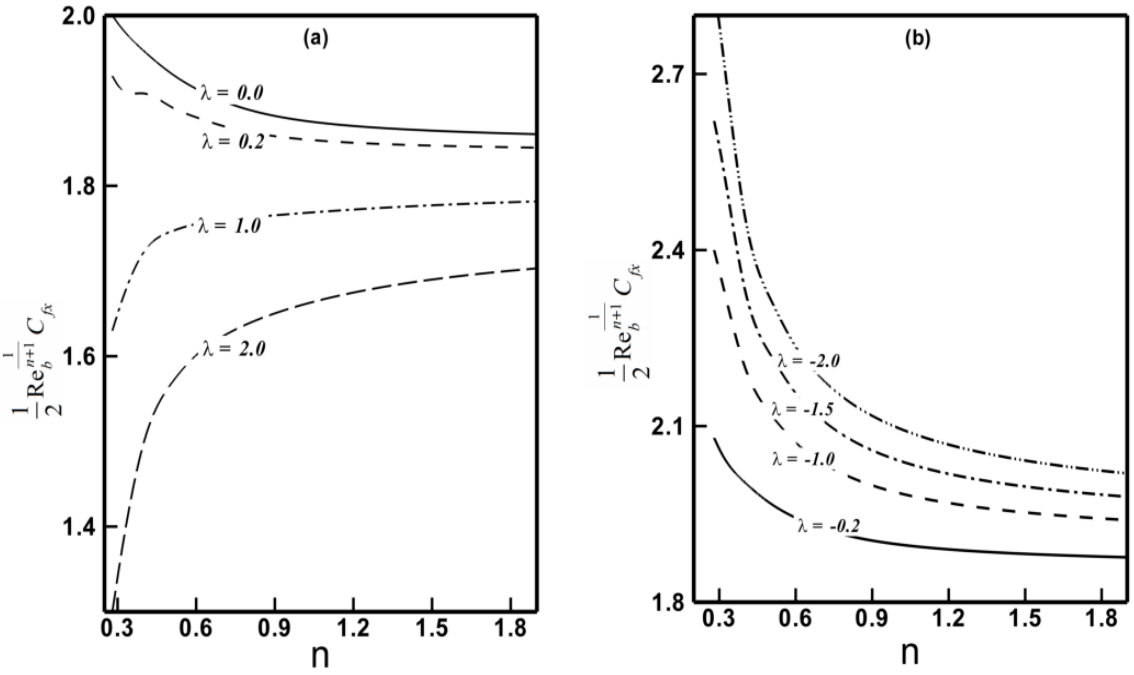

Figure 6.5: Profiles of the skin friction (magnitude) vs. power-law index n for assisting and opposing flows for different values of buoyancy parameter λ, when $s = A = 1.5$ and $\Pr = 100$.

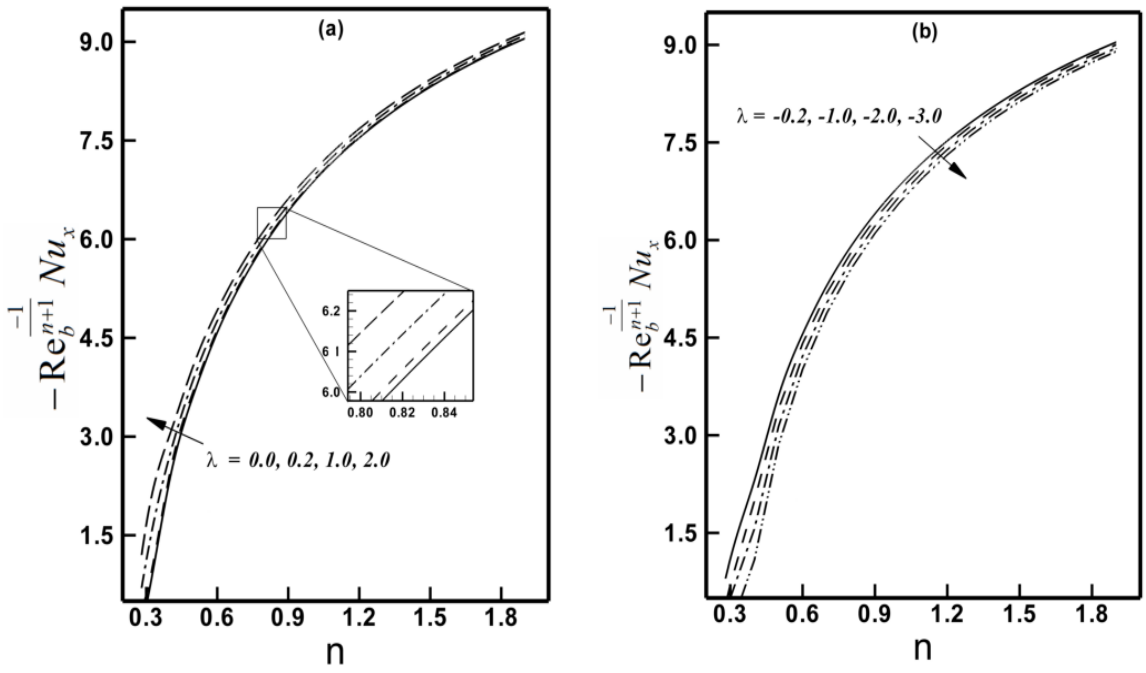

Figure 6.6: Profiles of Nusselt number vs. power-law index n for assisting and opposing flows for different values of buoyancy parameter λ, when $s = A = 1.5$ and $\Pr = 100$.

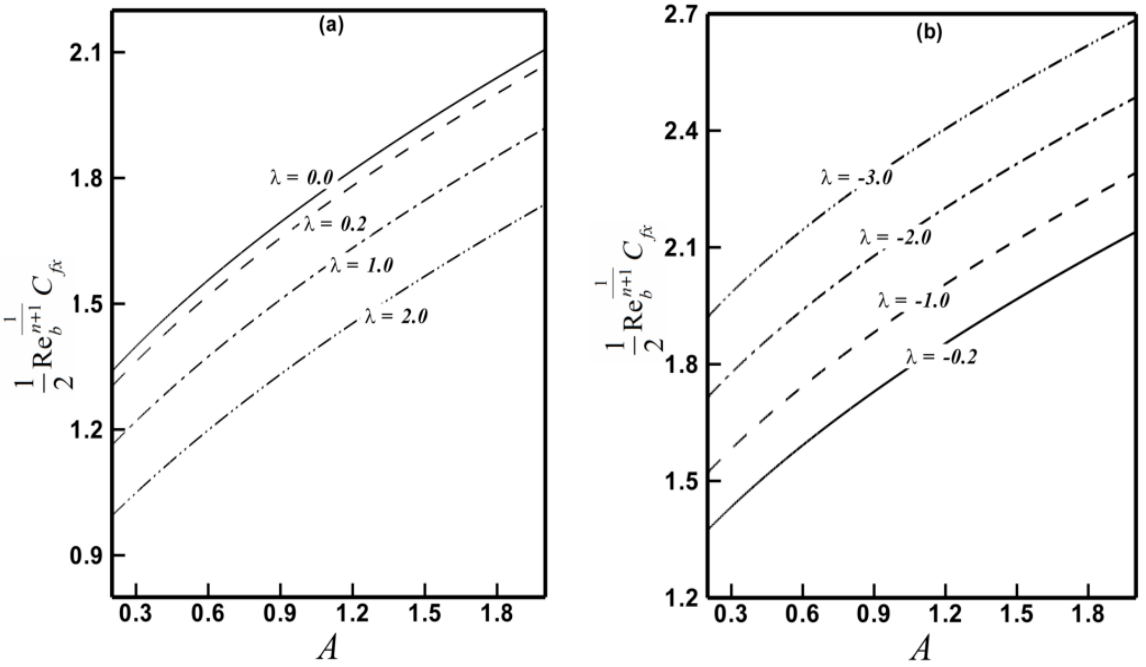

Figure 6.7: Profiles of the skin friction coefficient (magnitude) vs. material parameter A for assisting and opposing flows for different values of buoyancy parameter λ when $s = 1.5$, $\mathrm{Pr} = 100$ and $n = 0.5$ are fixed.

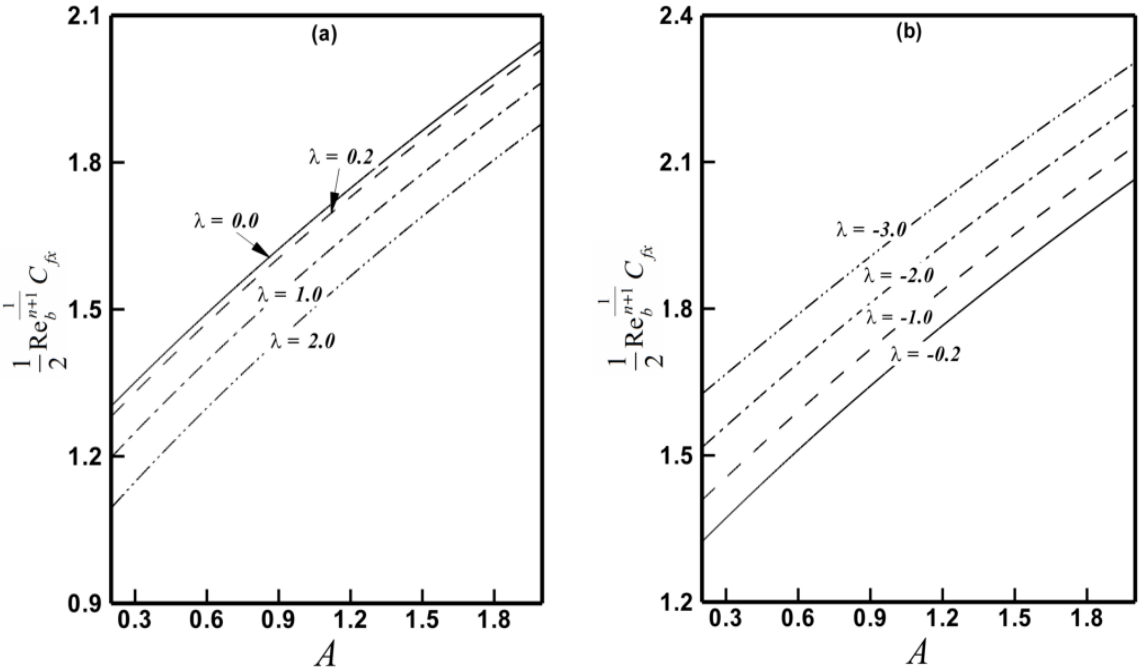

Figure 6.8: Profiles of the skin friction coefficient (magnitude) vs. material parameter A for assisting and opposing flows for different values of buoyancy parameter λ when $s = 1.5$, $\mathrm{Pr} = 100$ and $n = 1.5$ are fixed.

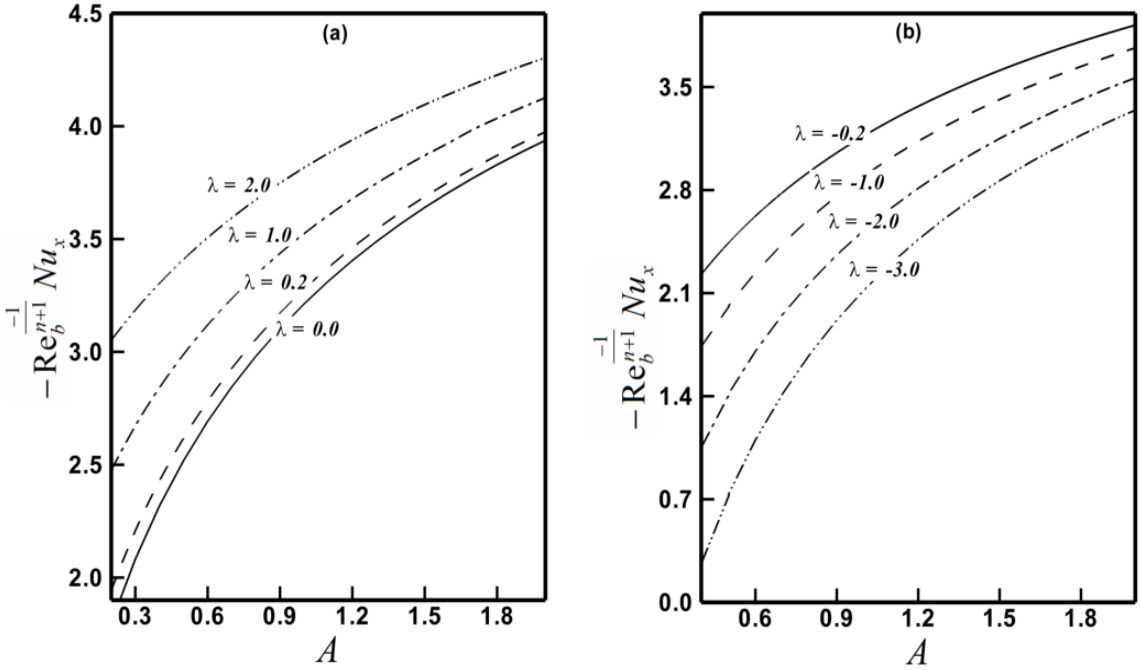

Figure 6.9: Profiles of the Nusselt number vs. material parameter A for assisting and opposing flows for different values of the buoyancy parameter λ when $s=1.5$, $\mathrm{Pr}=100$ and $n=0.5$ is fixed.

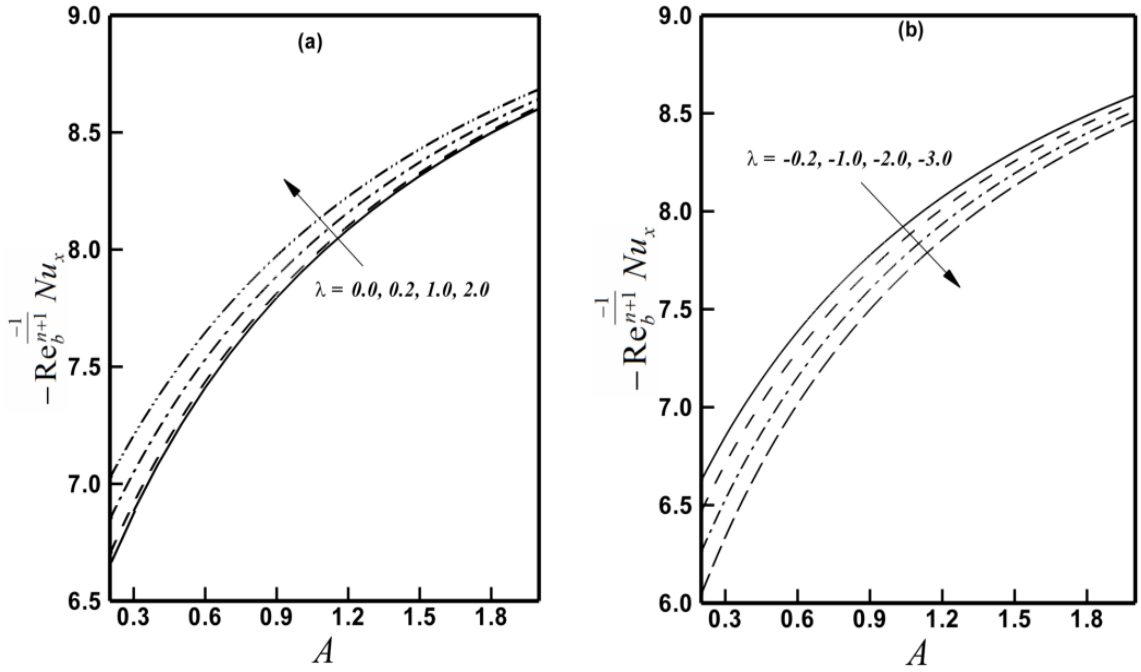

Figure 6.10: Profiles of the Nusselt number vs. material parameter A for assisting and opposing flows for different values of the buoyancy parameter λ when $s=1.5$, $\mathrm{Pr}=100$ and $n=1.5$ are fixed.

Chapter 7

Radiative Nonlinear Heat Transfer in Sisko Fluid near Stagnation Point Flow

In the present chapter, we endeavor to study the two-dimensional stagnation-point flow and heat transfer over a flat deformable sheet stretching in its own plane with a nonlinear stretching and free stream velocities. The effects of thermal radiation are incorporated using the nonlinear Rosseland approximation in the energy equation. The appropriate transformation is employed to transform the governing nonlinear partial differential equations to a couple of nonlinear ordinary differential equations. These equations are solved numerically using implicit finite difference method with Keller box scheme for shear thinning and shear thickening Sisko fluids, encompassing the wider ranges of non-dimensional parameters namely; the material parameter of Sisko fluid, velocity ratio parameter, the radiation parameter, the temperature ratio parameter, and the Prandtl number. The computational results for velocity, temperature and heat transfer characteristics are presented in graphical and tabular forms. The presented results are in excellent agreement with the previous studies in the limiting case.

7.1 Mathematical Description of the Problem

Consider the steady, two-dimensional flow of an incompressible Sisko fluid near a stagnation point towards an isothermal elastic stretching sheet coinciding with the plane $y = 0$ along the horizontal direction. Flow is restricted to the domain $y > 0$. Two equal and opposite forces are exerted along the x - axis, to stretch the surface whilst the origin is kept fixed. The sheet is maintained at constant temperature T_w while T_∞ is the ambient fluid temperature. The sheet is nonlinearly stretched in its own plane with velocity $U_w = cx^s$ and the velocity of the external flow is $U_\infty(x) = dx^s$, where c, d and s are positive real numbers. Making the standard boundary layer assumptions, the equations governing the flow of Sisko fluid and heat transfer in the presence of thermal radiation are expressed as:

$$\frac{\partial u}{\partial x} + \frac{\partial v}{\partial y} = 0, \tag{7.1}$$

$$\rho\left(u\frac{\partial u}{\partial x} + v\frac{\partial u}{\partial y}\right) = U_\infty \frac{dU_\infty}{dx} + a\frac{\partial^2 u}{\partial y^2} - b\frac{\partial}{\partial y}\left(-\frac{\partial u}{\partial y}\right)^n \text{ when } \frac{d}{c} < 1, \tag{7.2}$$

$$\rho\left(u\frac{\partial u}{\partial x} + v\frac{\partial u}{\partial y}\right) = U_\infty \frac{dU_\infty}{dx} + a\frac{\partial^2 u}{\partial y^2} + b\frac{\partial}{\partial y}\left(\frac{\partial u}{\partial y}\right)^n \text{ when } \frac{d}{c} > 1, \tag{7.3}$$

$$u\frac{\partial T}{\partial x} + v\frac{\partial T}{\partial y} = \frac{\kappa}{\rho c_p}\frac{\partial^2 T}{\partial y^2} - \frac{1}{\rho c_p}\frac{\partial q_r}{\partial y}. \tag{7.4}$$

The boundary conditions appropriate to the flow geometry are given as

$$u = U_w(x) = cx^s,\ v = 0 \text{ and } T = T_w \text{ at } y = 0, \tag{7.5}$$

$$u \to U_\infty(x) \text{ and } T \to T_\infty \text{ as } y \to +\infty. \tag{7.6}$$

The x-and y-axes are along and perpendicular to the sheet, respectively, (u,v) the velocity components along x-and y-directions, $T(x,y)$ the temperature field, $a, b, n\ (\geq 0)$ the material constants, with c_p as the specific heat of fluid at constant pressure, κ the thermal conductivity, and q_r the radiative heat flux.

Using the Rosseland approximation for radiation [76] and applying to an optically thick media, the radiative heat flux is simplified as

$$q_r = -\frac{4\sigma^*}{3\kappa^*}\frac{\partial T^4}{\partial y}, \tag{7.7}$$

where σ^* and κ^* are the Stefan-Boltzmann constant and the mean absorption coefficient, respectively. For a plane boundary layer flow over a hot surface the Eq. (7.7) reduces to

$$q_r = -\frac{16\sigma^*}{3\kappa^*}T^3\frac{\partial T}{\partial y}. \tag{7.8}$$

Thus, Eq. (7.4) can be expressed as

$$u\frac{\partial T}{\partial x} + v\frac{\partial T}{\partial y} = \frac{\partial}{\partial y}\left[\left(\frac{\kappa}{\rho c_p} + \frac{16\sigma^* T^3}{3\kappa^*\rho c_p}\right)\frac{\partial T}{\partial y}\right]. \tag{7.9}$$

The last term on right hand side of Eq. (7.9) is the radiative diffusion of energy flux integrated over all the frequencies with Rosseland diffusion approximation. The Rosseland diffusion approximation is not valid near the boundaries as the diffusion theory requires intensity to be isotropic. It can occur in the interior of an optically thick medium. However, the thermal radiations are attenuated prior to reach the interior of optically thick boundary layer, so the effects from the boundary surface can be ignored.

Now we introducing the following non-dimensional variables (cf. Chapter 3):

$$\eta = \frac{y}{x}\mathrm{Re}_b^{\frac{1}{n+1}},\ \psi(x,y) = xU\,\mathrm{Re}_b^{\frac{-1}{n+1}}\,f(\eta) \text{ and } \theta(\eta) = \frac{T-T_\infty}{T_w-T_\infty}, \tag{7.10}$$

with

$$u = \frac{\partial \psi}{\partial y} \text{ and } v = -\frac{\partial \psi}{\partial x}. \tag{7.11}$$

Keeping all the above in mind, the problem lead to the following ordinary differential equations

$$Af''' + n\left[\mathrm{sgn}\left(\frac{d}{c}-1\right)f''\right]^{n-1} f''' + \frac{s(2n-1)+1}{n+1}\,ff'' + s\left[\left(\frac{d}{c}\right)^2 - (f')^2\right] = 0, \tag{7.12}$$

$$\frac{d}{d\eta}\left[\left(1+\frac{4}{3N_R}(1+(\theta_w-1)\theta)^3\right)\theta'\right] + \mathrm{Pr}\frac{s(2n-1)+1}{(n+1)}\,f\theta' = 0, \tag{7.13}$$

where $\theta_w > 1$ and $N_R \to \infty$ implies no thermal radiation effects. Eqs. (7.12) and (7.13) are to be solved subject to the transformed boundary conditions:

$$f(0) = 0,\ f'(0) = 1,\ \theta(0) = 1, \tag{7.14}$$

$$f'(\eta) \to d/c \text{ and } \theta(\eta) \to 0 \text{ as } \eta \to \infty, \tag{7.15}$$

where prime denotes the differentiation with respect to η, Re_a, Re_b are the local Reynolds numbers, and A the material parameter of Sisko fluid, which are defined by

$$\mathrm{Re}_a = \frac{\rho x U}{a},\ \mathrm{Re}_b = \frac{\rho x^n U^{2-n}}{b} \text{ and } A = \frac{\mathrm{Re}_b^{\frac{2}{n+1}}}{\mathrm{Re}_a}. \tag{7.16}$$

Additionally, Pr is the generalized Prandtl number, N_R the radiation parameter, and θ_w the temperature ratio parameter. These parameters are, respectively, given by

$$\mathrm{Pr} = \frac{xUR_b^{\frac{2}{n+1}}}{\alpha},\ N_R = \frac{\kappa^*\kappa}{4\sigma^* T_\infty^3} \text{ and } \theta_w = \frac{T_w}{T_\infty}. \tag{7.17}$$

The shear stress at the wall in terms of the local skin-friction coefficient C_{fx} and the heat transfer coefficient in terms of the local Nusselt number Nu_x for external flow over a flat plate is defined according to

$$C_{fx} = \frac{2\tau_w}{\rho U_w^2}, \quad Nu_x = \frac{xq_w}{\kappa(T_w - T_\infty)}, \tag{7.18}$$

where $\tau_w = \left(a\frac{\partial u}{\partial y} + b\frac{\partial u}{\partial y}\left|\frac{\partial u}{\partial y}\right|^{n-1} \right)_w$.

Taking into account the thermal radiation, we can express the surface heat flux as:

$$q_w = -\kappa\left(\frac{\partial T}{\partial y}\right)_w + (q_r)_w. \tag{7.19}$$

By inserting Eq. (7.10), the shear stress at wall and the local Nusselt number are transformed as

$$\frac{1}{2}\mathrm{Re}_b^{\frac{1}{n+1}} C_{fx} = Af''(0) - \left[-f''(0)\right]^n \text{ when } \frac{d}{c} < 1, \tag{7.20}$$

$$\frac{1}{2}\mathrm{Re}_b^{\frac{1}{n+1}} C_{fx} = Af''(0) + \left[f''(0)\right]^n \text{ when } \frac{d}{c} > 1, \tag{7.21}$$

and

$$\mathrm{Re}_b^{-1/n+1} Nu_x = -\theta'(0)\left[1 + \frac{4\theta_w^3}{3N_R}\right]. \tag{7.22}$$

7.2. Numerical Solution of the Problem

For most of the differential equations arising in non-Newtonian fluid mechanics, closed form solution is not possible in general. One therefore has to seek the numerical solutions of the ordinary differential equations with the associated boundary conditions governing flow and heat transfer. So, Eqs. (7.12) to (7.15) constituting a two-point boundary value

problem are solved by employing implicit finite difference method with Keller box scheme. To employ this method, Eqs. (7.12) and (7.13) are written as an equivalent first order system as follows:

$$f' = p, \tag{7.23}$$

$$p' = q, \tag{7.24}$$

$$\theta' = t, \tag{7.25}$$

$$Aq' + n\left[\operatorname{sgn}\left(\frac{d}{c}-1\right)q\right]^{n-1} q' + \frac{s(2n-1)+1}{n+1} fq - s\left[\left(\frac{d}{c}\right)^2 - p^2\right] = 0, \tag{7.26}$$

$$t'\left[1+\frac{4}{3N_R}\left(1+\left(\theta_w-1\right)\theta\right)^3\right] + \frac{4}{3N_R}(\theta_w-1)(t)^2\left[1+\left(\theta_w-1\right)\theta\right]^2$$

$$+\Pr\frac{s(2n-1)+1}{n+1} tf = 0. \tag{7.27}$$

The corresponding boundary conditions are

$$f(0) = 0,\ p(0) = 1 \text{ and } \theta(0) = 1, \tag{7.28}$$

$$p \to d/c,\ \theta \to 0 \text{ as } \eta \to \infty. \tag{7.29}$$

The details of this method are available in [66]; however, only the main features are precisely enumerated here. The functions and their derivatives are approximated by central difference at the mid-point defined by $\eta_{j-\frac{1}{2}} = \frac{\left(\eta_j + \eta_{j-1}\right)}{2}$ of the segment $\eta_{j-1}\eta_j$, where $j = 1, 2 \ldots N$. The resulting set of nonlinear difference equations are linearized using the Newton's quasi-linearization technique and are solved using a block-tridiagonal algorithm [66]. An initial guess is provided for the five variables. The initial guess satisfying boundary conditions gives the rapid convergence The step size $\Delta\eta = 0.001$ is

taken for this computation. The iterative procedure is terminated when the difference in computing the velocity and the temperature in the next iteration is less than 10^{-5}. The present method is unconditionally stable, has second-order accuracy, and fast convergence that reduce the computation time and memory usage.

7.3 Results and Discussion

To understand the phenomena of the stagnation-point flow of Sisko fluid towards a nonlinear stretching sheet and the cooling of the isothermal sheet by combined radiation and forced convection, the coupled nonlinear ordinary differential equations (7.12) and (7.13) subject to boundary conditions (7.14) and (7.15) have been solved numerically. The effects of relevant non-dimensional parameters influencing the flow and heat transfer in stagnation point flow with their respective ranges focused are: the material parameter of Sisko fluid ($1 \le A \le 4$), velocity ratio ($0.4 \le d/c \le 1.6$), the stretching parameter $s = 1/3$ and 2.0, the Prandtl number ($1 \le \Pr \le 7$), the radiation parameter ($0.5 \le N_R \le 10$), and temperature ratio parameter ($1.1 \le \theta_w \le 1.9$).

Prior to begin the discussion of the results obtained in this study, we check the adequacy of our numerical computations by comparing the present results as a special case of our problem with the previous published relevant literature. Tables 7.1 and 7.2 compare the presently computed results and those results obtained analytically by the homotopy analysis method [63,68]. It is fair to establish that the present results agree excellently with the open literature. The marginal differences of the magnitude of values can be ascribed to the choice of different solution methodology.

In order to show the influence of the parameters entering the problem on velocity and

temperature fields figures 7.1 to 7.6 show the graphical presentations of our numerical results. The representative velocity profiles for the shear thinning ($n<1$) and shear thickening ($n>1$) fluids with the variation of velocity ratio parameter d/c and stretching parameter s are presented in figures 7.1(a,b). These plots show that the velocity is monotonically increasing when $d/c>1$ and it is monotonically decreasing with the boundary layer structure inverted for $d/c<1$. An increase in velocity profile is observed on increasing the velocity ratio parameter due to the increased acceleration in the free stream velocity. Further, both these figures also describe the thinning of the boundary layer for stretching parameter $s=2.0$. A comparison of these figures also reveals that there is a decrease in boundary layer thickness for shear thickening fluids as compared to those of the shear thinning fluids. The representative profiles of the dimensionless temperature $\theta(\eta)$ with the variation velocity ratio parameter d/c and stretching parameter s for shear thinning $(n<1)$ and shear thickening $(n>1)$ fluids are presented in figures 7.2(a,b). Primarily, when d/c is increased progressively, the thermal boundary layer decreases. Further, the larger stretching parameter ($s=2$) has marginal effect on the temperature field for shear thinning fluids in contrast to the shear thickening fluids. Also, a comparison of these figures reveals that for shear thinning Sisko fluids the temperature effects reach far deeper into the fluid as the shear thinning promotes the heat transfer.

Figures 7.3(a-d) depict the effects of the material parameter A on temperature field. These figures show that the material parameter A affects the temperature field marginally. However, a slight reduction in temperature with an increase in the value of A is observed for case $d/c<1$ and vice versa for $d/c>1$. It is also noted that the effects of material parameter A on temperature profiles are found to be more pronounced when

$d/c<1$.

The influence of Prandtl number Pr on temperature profiles for shear thinning and shear thickening Sisko fluids and velocity ratio parameter $d/c<1$ and $d/c>1$ is demonstrated through figures 7.4(a-d). It is seen that the thermal boundary layer thickness decreases rapidly with increasing values of Pr and this trend is true for both shear thinning and shear thickening Sisko fluids. The concomitant increase in the slope at wall shows enhanced heat transfer at the wall. Further, the profiles seem to become more close as the value of Pr is increased, showing a diminishing dependency of temperature field for moderate to higher Prandtl number. It is also noticed that thermal boundary layer is thick for case $d/c<1$ as compared to that of $d/c>1$.

Figures 7.5(a-d) demonstrate the influence of the radiation parameter N_R on temperature profiles of shear thinning and shear thickening Sisko fluids. These figures show the thickening of thermal boundary layer with decreasing N_R. It can be ascribed to the fact that thermal radiation provides an extra mean to diffuse energy. As the effect of radiation is enhanced, the thermal boundary layer thickness increases and the profile becomes *S* shaped and there appears a point of inflexion. These facts can be explained as: the thermal boundary layer thickness depends on the thermal diffusivity. When the thermal diffusivity is large the thermal boundary layer thickness is large. The problems involving nonlinear Rosseland approximation contains two diffusion terms, $\left(\frac{\kappa}{\rho c_p}+\frac{16\sigma^* T^3}{3\kappa^*\rho c_p}\right)$, the first one is constant and second is variable across the boundary layer due to thermal radiation. This means that near the plate, where the fluid temperature is large the thermal diffusivity is large, whereas far away from the plate, where the temperature is low, the thermal diffusivity is low. The large thermal diffusivity near the

plate creates a thick boundary layer which, far away from the plate, is forced to become thin due to low thermal diffusivity. However, as the temperature ratio parameter θ_w increases, it is observed from figures 7.6 (a-d) that the temperature profiles increase and this influence is true for shear thinning and shear thickening Sisko fluids. Consequently, the thermal boundary layer thickness grows.

Finally, it is useful to see the effects of Prandtl number on the local Nusselt number Nu_x, given by expression (7.22), giving the rate of heat transfer at the wall. Figure 7.7 summarizes the trends in Nu_x for shear thinning and shear thickening Sisko fluids, when Prandtl number Pr is varied. It is apparent from this table that there is a rise in the rate of heat transfer at the wall when $\Pr$ is increased.

Table 7.1: A tabulation of the local skin friction coefficient, in terms of the comparison between the present numerical results and the HAM results (Ref [63]) when $\frac{d}{c} = 2.0$, $s = 1.0$ is fixed.

	$\frac{1}{2}\mathrm{Re}_b^{\frac{1}{n+1}} C_{fx}$			
	$n = 1$		$n = 2$	
A	Present results	HAM results	Present results	HAM results
1	2.853174	2.859920	2.919060	2.918177
2	3.494415	3.494500	3.500580	3.499708
3	4.035034	4.034040	4.020395	4.020270

Table 7.2: A tabulation of the local skin friction coefficient, in terms of the comparison between the present numerical results and the HAM results (Ref. [68]) when, $s = 1.0$ and $A = 0.0$ is fixed.

	$f''(0)$			
	$n = 1$		$n = 2$	
$\frac{d}{c}$	Present results	HAM results	Present results	HAM results
0.2	-0.9181	-0.9181	-	-
2.0	2.0174	2.0175	-	-
2.0	-	-	1.5047	1.5049

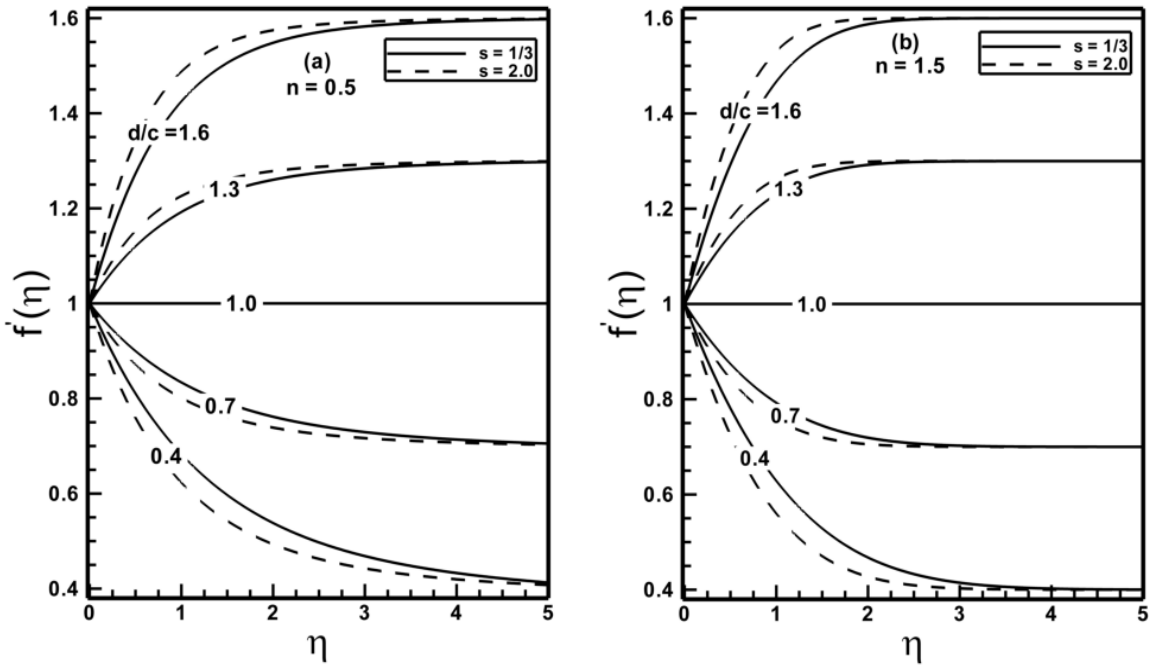

Figure 7.1: Profiles of the velocity $f'(\eta)$ for different values of the velocity ratio parameter d/c for different stretching cases when $A=1.5$ is fixed.

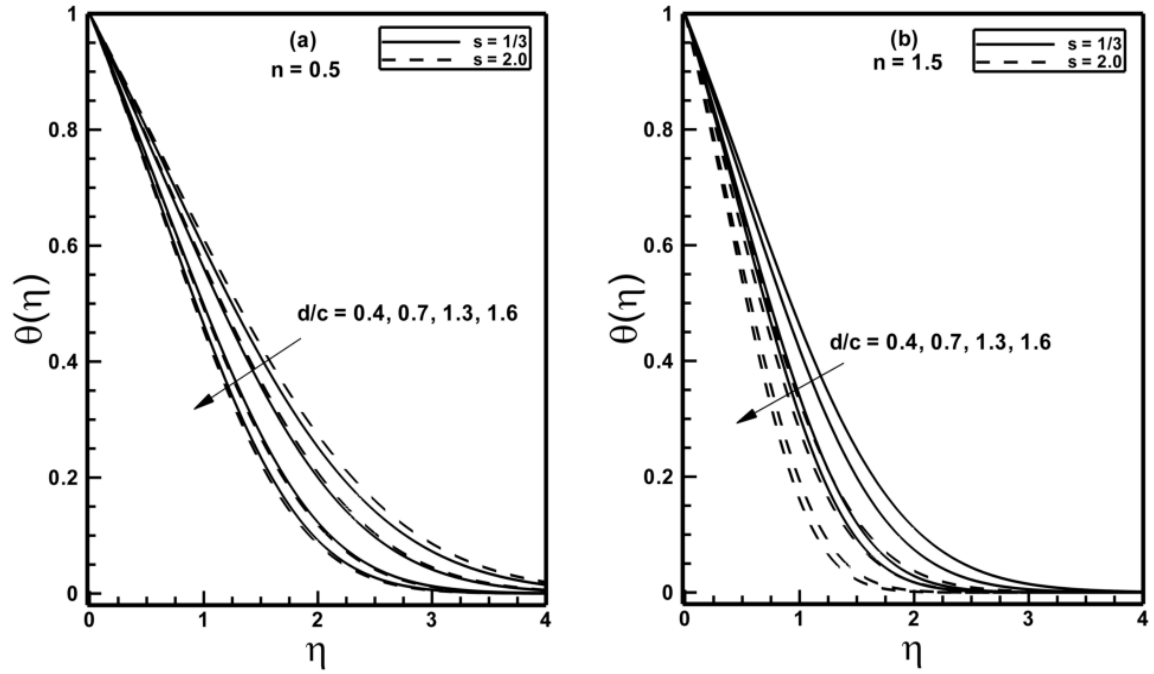

Figure 7.2: Profiles of the temperature $\theta(\eta)$ for different values of the velocity ratio parameter d/c, for different stretching cases when $A=1.5$, $\Pr=1.5$, $N_R=2.0$ and $\theta_w=1.5$ are fixed.

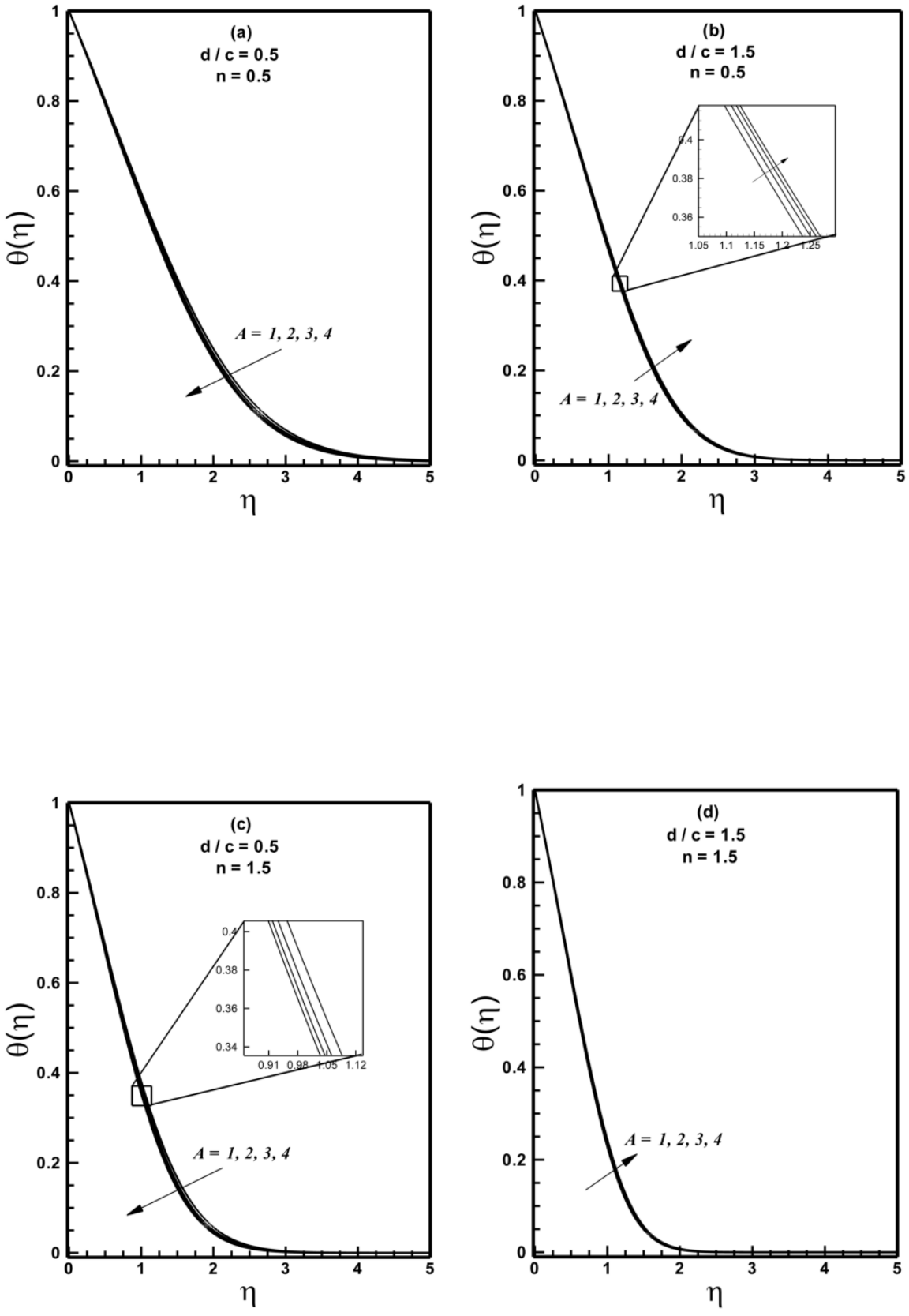

Figure 7.3 : Profiles of the temperature $\theta(\eta)$ for different values of the material parameter A when $s=1.5$, $\Pr=1.5$, $N_R=2.0$, and $\theta_w=1.5$ are fixed.

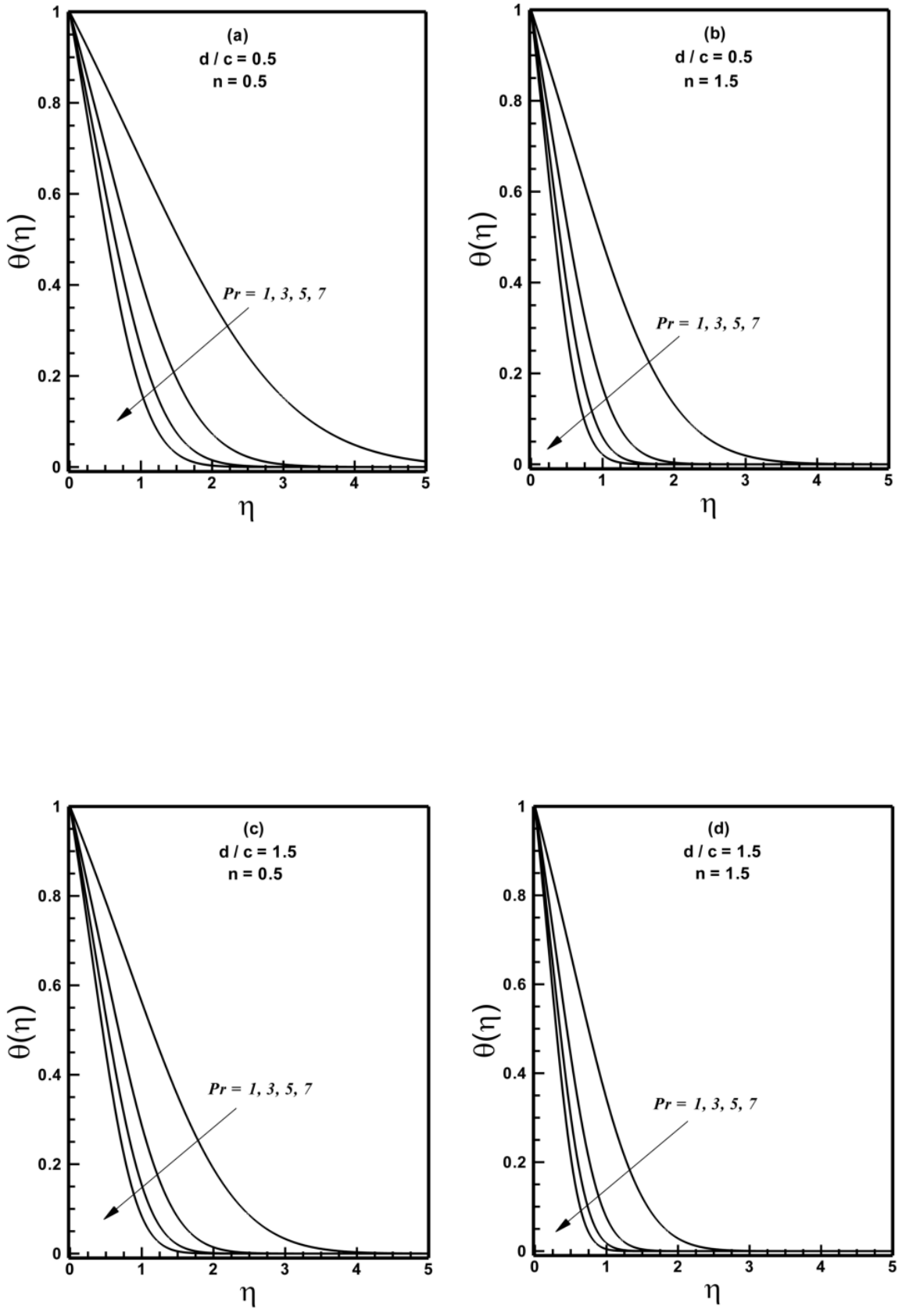

Figure 7.4: Profiles of the temperature $\theta(\eta)$ for different values of Prandtl number Pr when $A=1.5$, $s=1.5$, $N_R=2.0$ and $\theta_w=1.5$ are fixed.

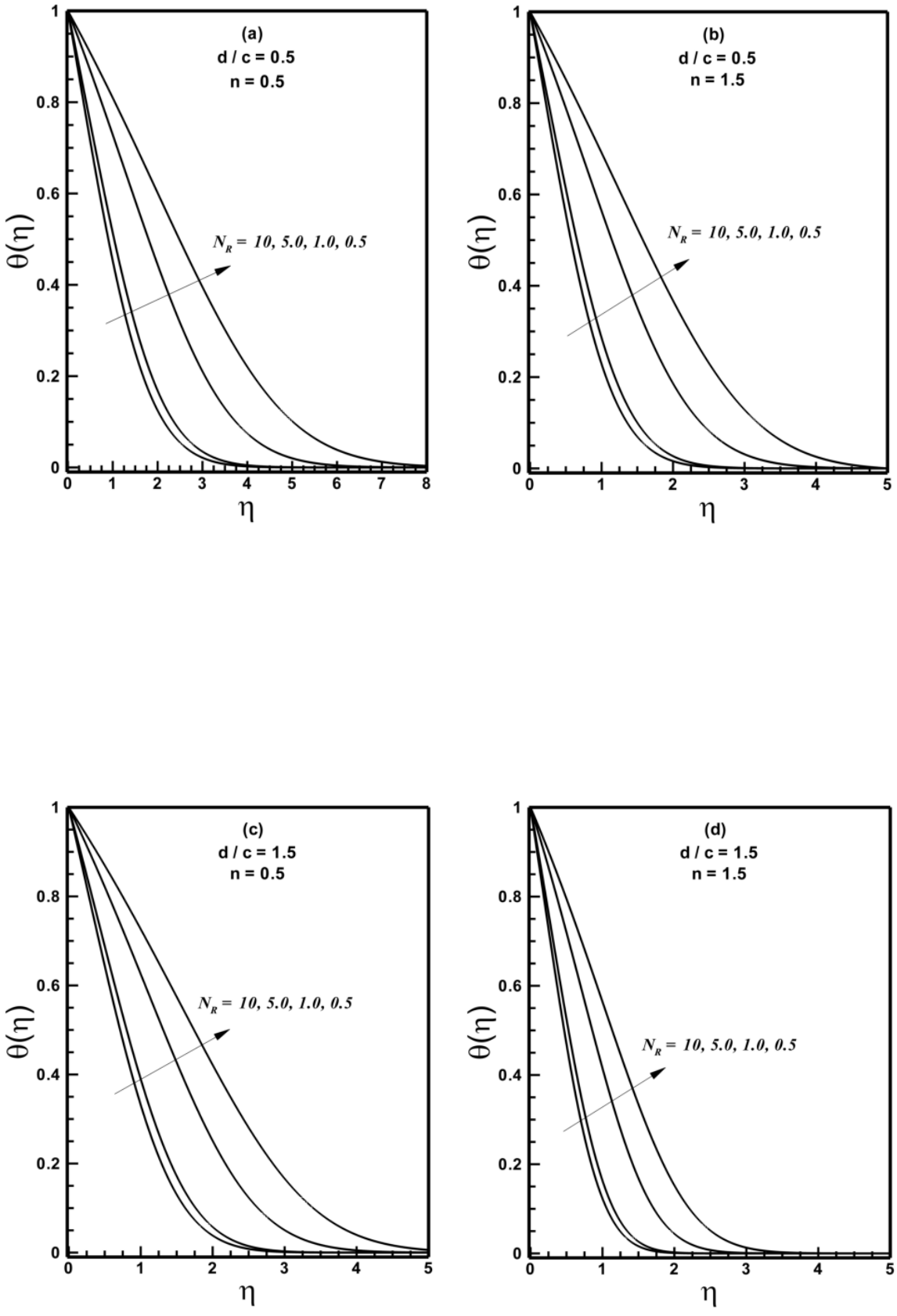

Figure 7.5: Profiles of the temperature $\theta(\eta)$ for different values of the radiation parameter N_R when $s=1.5$, $A=1.5$, $\Pr=1.5$ and $\theta_w=1.5$ are fixed.

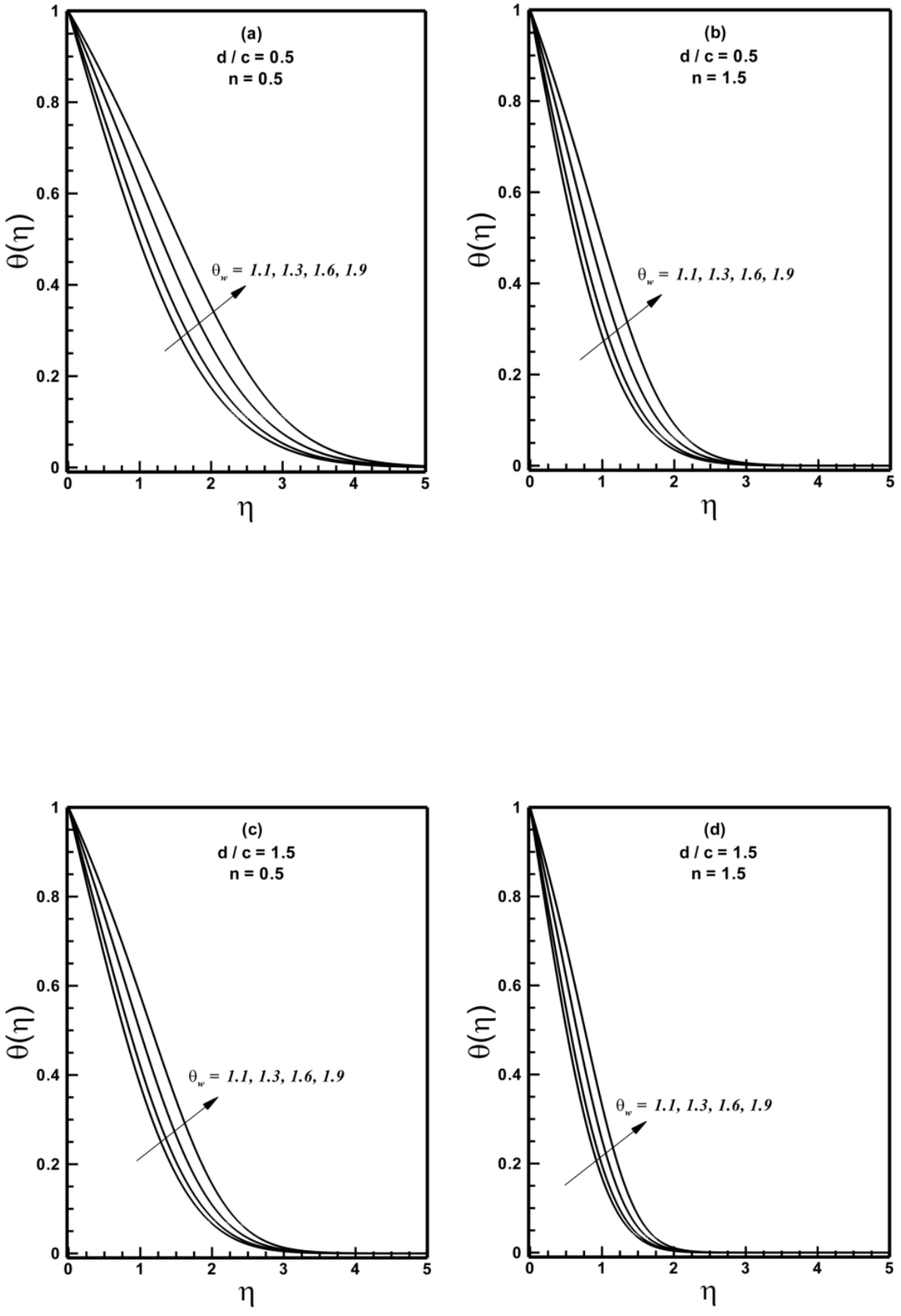

Figure 7.6: Profiles of the temperature $\theta(\eta)$ for different values of the temperature ratio parameter θ_w when $s=1.5$, $A=1.5$, $\Pr=1.5$ and $N_R=2.0$ are fixed.

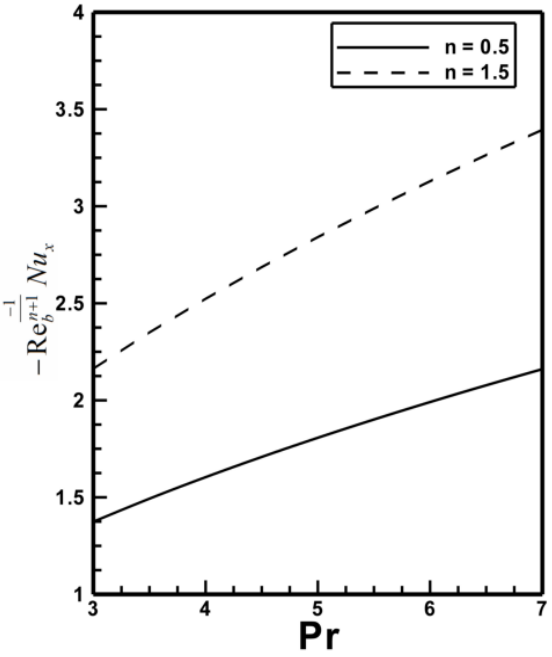

Figure 7.7: Variation in local Nusselt number for different values of Prandtl number when $s = 1.5$, $A = 1.5$, $N_R = 2.0$ and $\frac{d}{c} = 0.5$ are fixed.

Chapter 8

Convective Flow of Sisko Fluid over a Bidirectional Stretching Surface

The investigation in this chapter focuses the flow and heat transfer characteristics of the steady three-dimensional Sisko fluid flow driven by a bidirectional stretching sheet. The governing nonlinear partial differential equations are first modeled and suitable transformation is used to convert them into coupled ordinary differential equations. The resulting equations are solved numerically by the shooting method using adaptive Runge Kutta algorithm in combination with Newton's method in the flow domain. The numerical results for the velocity and temperature fields are graphically presented and effects of the relevant parameters are discussed in detail. Moreover, the skin-friction coefficient and local Nusselt number for different values of the power-law index and stretching ratio parameter are presented through tabulated data.

One of the interesting observations is that the influence of the stretching ratio parameter decreases the horizontal velocity component and temperature for Sisko fluid, for all values of the power-law index. However, quite the opposite is true with the vertical velocity component. It holds good for the Bingham plastic fluid also. The computed results discloses many interesting behaviors that warrant a further study of the shear thinning /thickening phenomenon in non-Newtonian fluids.

The numerical results are also verified with the results obtained analytically by the

homotopy analysis method (HAM). Additionally, to ascertain the accuracy of the computational results, an excellent comparison with the previous studies in limiting case is made.

8.1 Mathematical Model and Formulation

8.1.1 Boundary Layer Equations

In this section, we have an interest in mathematical modeling of governing equations for three-dimensional flow of an incompressible Sisko fluid in Cartesian coordinates. We make the derivation of such equations by employing the law of conservation of mass and linear momentum given by Eqs. (3.1) and (3.2), respectively. The extra stress tensor for an incompressible Sisko fluid has the form given through Eq. (3.5).

For a steady three-dimensional flow, the velocity and stress fields have the form

$$\mathbf{V}=\left[u(x,y,z),v(x,y,z),w(x,y,z)\right],\quad \mathbf{S}=\mathbf{S}(x,y,z), \tag{8.1}$$

where u,v and w are the x -, y - and z - components of the velocity vector.

In view of Eqs. (3.2) and (8.1), ignoring the body forces, one has

$$\rho\left(u\frac{\partial u}{\partial x}+v\frac{\partial u}{\partial y}+w\frac{\partial u}{\partial z}\right)=-\frac{\partial p}{\partial x}+\frac{\partial\left(s_{xx}\right)}{\partial x}+\frac{\partial\left(s_{xy}\right)}{\partial y}+\frac{\partial\left(s_{xz}\right)}{\partial z}, \tag{8.2}$$

$$\rho\left(u\frac{\partial v}{\partial x}+v\frac{\partial v}{\partial y}+w\frac{\partial v}{\partial z}\right)=-\frac{\partial p}{\partial y}+\frac{\partial\left(s_{yx}\right)}{\partial x}+\frac{\partial\left(s_{yy}\right)}{\partial y}+\frac{\partial\left(s_{yz}\right)}{\partial z}, \tag{8.3}$$

$$\rho\left(u\frac{\partial w}{\partial x}+v\frac{\partial w}{\partial y}+w\frac{\partial w}{\partial z}\right)=-\frac{\partial p}{\partial z}+\frac{\partial\left(s_{zx}\right)}{\partial x}+\frac{\partial\left(s_{zy}\right)}{\partial y}+\frac{\partial\left(s_{zz}\right)}{\partial z}, \tag{8.4}$$

where s_{xx}, s_{xy}, s_{xz}, s_{yx}, s_{yy}, s_{yz}, s_{zx}, s_{zy}, and s_{zz} are the components of extra stress tensor, $\mathbf{S}$.

Now, substituting Eq. (8.1) into Eq. (3.5) along with Eq. (3.6) we get

$$s_{xx}=\left(a+b\left|\frac{1}{2}tr\mathbf{A}_1^2\right|^{\frac{n-1}{2}}\right)\left(2\frac{\partial u}{\partial x}\right),\quad s_{yx}=s_{xy}=\left(a+b\left|\frac{1}{2}tr\mathbf{A}_1^2\right|^{\frac{n-1}{2}}\right)\left(\frac{\partial u}{\partial y}+\frac{\partial v}{\partial x}\right),\tag{8.5a}$$

$$s_{xz}=s_{zx}=\left(a+b\left|\frac{1}{2}tr\mathbf{A}_1^2\right|^{\frac{n-1}{2}}\right)\left(\frac{\partial u}{\partial z}+\frac{\partial w}{\partial x}\right),\quad s_{yy}=\left(a+b\left|\frac{1}{2}tr\mathbf{A}_1^2\right|^{\frac{n-1}{2}}\right)\left(2\frac{\partial v}{\partial y}\right),\tag{8.5b}$$

$$s_{zy}=s_{yz}=\left(a+b\left|\frac{1}{2}tr\mathbf{A}_1^2\right|^{\frac{n-1}{2}}\right)\left(\frac{\partial v}{\partial z}+\frac{\partial w}{\partial y}\right),\quad s_{zz}=\left(a+b\left|\frac{1}{2}tr\mathbf{A}_1^2\right|^{\frac{n-1}{2}}\right)\left(2\frac{\partial w}{\partial z}\right),\tag{8.5c}$$

where

$$J=\left|\frac{1}{2}tr\mathbf{A}_1^2\right|^{\frac{n-1}{2}}=\left|2\left(\frac{\partial u}{\partial x}\right)^2+2\left(\frac{\partial v}{\partial y}\right)^2+2\left(\frac{\partial w}{\partial z}\right)^2+\left(\frac{\partial u}{\partial y}+\frac{\partial v}{\partial x}\right)^2\right.$$

$$\left.+\left(\frac{\partial u}{\partial z}+\frac{\partial w}{\partial x}\right)^2+\left(\frac{\partial v}{\partial z}+\frac{\partial w}{\partial y}\right)^2\right|.\tag{8.6}$$

Employing Eqs. 8.5(a-c), momentum Eqs. (8.2) to (8.4) for steady, three dimensional flow of an incompressible Sisko fluid are stated as follows:

$$\rho\left(u\frac{\partial u}{\partial x}+v\frac{\partial u}{\partial y}+w\frac{\partial u}{\partial z}\right)=-\frac{\partial p}{\partial x}+a\left(\frac{\partial^2 u}{\partial x^2}+\frac{\partial^2 u}{\partial y^2}+\frac{\partial^2 u}{\partial z^2}\right)+2b\frac{\partial}{\partial x}\left[\frac{\partial u}{\partial x}J\right]$$

$$+b\frac{\partial}{\partial y}\left[\left(\frac{\partial u}{\partial y}+\frac{\partial v}{\partial x}\right)J\right]+b\frac{\partial}{\partial z}\left[\left(\frac{\partial u}{\partial z}+\frac{\partial w}{\partial x}\right)J\right],\tag{8.7}$$

$$\rho\left(u\frac{\partial v}{\partial x}+v\frac{\partial v}{\partial y}+w\frac{\partial v}{\partial z}\right)=-\frac{\partial p}{\partial y}+a\left(\frac{\partial^2 v}{\partial x^2}+\frac{\partial^2 v}{\partial y^2}+\frac{\partial^2 v}{\partial z^2}\right)+b\frac{\partial}{\partial x}\left[\left(\frac{\partial u}{\partial y}+\frac{\partial v}{\partial x}\right)J\right]$$

$$+2b\frac{\partial}{\partial y}\left[\left(\frac{\partial v}{\partial y}\right)J\right]+b\frac{\partial}{\partial z}\left[\left(\frac{\partial v}{\partial z}+\frac{\partial w}{\partial y}\right)J\right],\tag{8.8}$$

$$\rho\left(u\frac{\partial w}{\partial x}+v\frac{\partial w}{\partial y}+w\frac{\partial w}{\partial z}\right)=-\frac{\partial p}{\partial z}+a\left(\frac{\partial^2 w}{\partial x^2}+\frac{\partial^2 w}{\partial y^2}+\frac{\partial^2 w}{\partial z^2}\right)+b\frac{\partial}{\partial x}\left[\left(\frac{\partial u}{\partial z}+\frac{\partial w}{\partial x}\right)J\right]$$

$$+b\frac{\partial}{\partial y}\left[\left(\frac{\partial v}{\partial z}+\frac{\partial w}{\partial y}\right)J\right]+b\frac{\partial}{\partial z}\left[\frac{\partial w}{\partial z}J\right]. \tag{8.9}$$

To facilitate the boundary layer approximation, the length and velocity scales for the boundary layer analysis are chosen as L and U, then the non-dimensional variables would be:

$$\tilde{u}=\frac{u}{U},\ \tilde{v}=\frac{v}{U},\ \tilde{w}=\frac{wL}{U\delta},\ \tilde{x}=\frac{x}{L},\ \tilde{y}=\frac{y}{L},\ \tilde{z}=\frac{z}{\delta},\ \text{and}\ \tilde{p}=\frac{p-p_\infty}{\rho U^2}. \tag{8.10}$$

With the help of non-dimensionalization given by Eq. (8.10), the boundary layer equations for a non-Newtonian Sisko fluid given as Eqs. (8.7) to (8.9) can be transformed as follows:

$$\tilde{u}\frac{\partial\tilde{u}}{\partial\tilde{x}}+\tilde{v}\frac{\partial\tilde{u}}{\partial\tilde{y}}+\tilde{w}\frac{\partial\tilde{u}}{\partial\tilde{z}}=-\frac{\partial\tilde{p}}{\partial\tilde{x}}+\frac{a/\rho}{UL}\frac{\partial^2\tilde{u}}{\partial\tilde{x}^2}+\frac{a/\rho}{UL}\frac{\partial^2\tilde{u}}{\partial\tilde{y}^2}+\frac{a/\rho}{UL}\left(\frac{L}{\delta}\right)^2\frac{\partial^2\tilde{u}}{\partial\tilde{z}^2}$$

$$+2\frac{b/\rho}{U^{2-n}L^n}\left(\frac{L}{\delta}\right)^{n+1}\frac{1}{\left(L/\delta\right)^2}\frac{\partial}{\partial\tilde{x}}\left[\left(\frac{\partial\tilde{u}}{\partial\tilde{x}}\right)\tilde{J}\right]+\frac{b/\rho}{U^{2-n}L^n}\left(\frac{L}{\delta}\right)^{n+1}\frac{1}{\left(L/\delta\right)^2}\frac{\partial}{\partial\tilde{y}}\left[\left(\frac{\partial\tilde{u}}{\partial\tilde{y}}+\frac{\partial\tilde{v}}{\partial\tilde{x}}\right)\tilde{J}\right]$$

$$+\frac{b/\rho}{U^{2-n}L^n}\left(\frac{L}{\delta}\right)^{n+1}\frac{\partial}{\partial\tilde{z}}\left[\left(\frac{\partial\tilde{u}}{\partial\tilde{z}}+\frac{1}{\left(L/\delta\right)^2}\frac{\partial\tilde{u}}{\partial\tilde{x}}\right)\tilde{J}\right], \tag{8.11}$$

$$\tilde{u}\frac{\partial\tilde{v}}{\partial\tilde{x}}+\tilde{v}\frac{\partial\tilde{v}}{\partial\tilde{y}}+\tilde{w}\frac{\partial\tilde{v}}{\partial\tilde{z}}=-\frac{\partial\tilde{p}}{\partial\tilde{y}}+\frac{a/\rho}{UL}\frac{\partial^2\tilde{v}}{\partial\tilde{x}^2}+\frac{a/\rho}{UL}\frac{\partial^2\tilde{v}}{\partial\tilde{y}^2}+\frac{a/\rho}{UL}\left(\frac{L}{\delta}\right)^2\frac{\partial^2\tilde{v}}{\partial\tilde{z}^2}$$

$$+\frac{b/\rho}{U^{2-n}L^n}\left(\frac{L}{\delta}\right)^{n+1}\frac{1}{\left(L/\delta\right)^2}\frac{\partial}{\partial\tilde{x}}\left[\left(\frac{\partial\tilde{v}}{\partial\tilde{x}}+\frac{\partial\tilde{u}}{\partial\tilde{y}}\right)\tilde{J}\right]+2\frac{b/\rho}{U^{2-n}L^n}\left(\frac{L}{\delta}\right)^{n+1}\frac{1}{\left(L/\delta\right)^2}\frac{\partial}{\partial\tilde{y}}\left[\left(\frac{\partial\tilde{v}}{\partial\tilde{y}}\right)\tilde{J}\right]$$

$$+\frac{b/\rho}{U^{2-n}L^n}\left(\frac{L}{\delta}\right)^{n+1}\frac{\partial}{\partial\tilde{z}}\left[\left(\frac{\partial\tilde{v}}{\partial\tilde{z}}+\frac{1}{\left(L/\delta\right)^2}\frac{\partial\tilde{w}}{\partial\tilde{y}}\right)\tilde{J}\right], \tag{8.12}$$

$$\frac{1}{\left(L/\delta\right)^2}\left(\tilde{u}\frac{\partial\tilde{w}}{\partial\tilde{x}}+\tilde{v}\frac{\partial\tilde{w}}{\partial\tilde{y}}+\tilde{w}\frac{\partial\tilde{w}}{\partial\tilde{z}}\right)=-\frac{\partial\tilde{p}}{\partial\tilde{z}}+\frac{1}{\left(L/\delta\right)^2}\left(\frac{a/\rho}{UL}\frac{\partial^2\tilde{w}}{\partial\tilde{x}^2}+\frac{a/\rho}{UL}\frac{\partial^2\tilde{w}}{\partial\tilde{y}^2}\right)$$

$$+\frac{1}{(L/\delta)^2}\left[\frac{a/\rho}{UL}\left(\frac{L}{\delta}\right)^2\frac{\partial^2\tilde{w}}{\partial\tilde{z}^2}+\frac{b/\rho}{U^{2-n}L^n}\left(\frac{L}{\delta}\right)^{n+1}\frac{\partial}{\partial\tilde{x}}\left[\left(\frac{\partial\tilde{u}}{\partial\tilde{z}}+\frac{1}{(L/\delta)^2}\frac{\partial\tilde{w}}{\partial\tilde{x}}\right)\tilde{J}\right]\right]$$

$$+\frac{1}{(L/\delta)^2}\frac{b/\rho}{U^{2-n}L^n}\left(\frac{L}{\delta}\right)^{n+1}\frac{\partial}{\partial\tilde{y}}\left[\left(\frac{\partial\tilde{v}}{\partial\tilde{z}}+\frac{1}{(L/\delta)^2}\frac{\partial\tilde{w}}{\partial\tilde{y}}\right)\tilde{J}\right]$$

$$+2\frac{1}{(L/\delta)^2}\frac{b/\rho}{U^{2-n}L^n}\left(\frac{L}{\delta}\right)^{n+1}\frac{\partial}{\partial\tilde{z}}\left[\left(\frac{\partial\tilde{w}}{\partial\tilde{y}}\right)\tilde{J}\right], \tag{8.13}$$

$$\tilde{J}=\left(\frac{U}{\delta}\right)^{n-1}\left|\frac{1}{(L/\delta)^2}\left[\left(\frac{\partial\tilde{u}}{\partial\tilde{y}}\right)^2+\left(\frac{\partial\tilde{v}}{\partial\tilde{x}}\right)^2+\left(\frac{\partial\tilde{u}}{\partial\tilde{x}}\right)^2+\left(\frac{\partial\tilde{v}}{\partial\tilde{y}}\right)^2+2\frac{\partial\tilde{u}}{\partial\tilde{y}}\frac{\partial\tilde{v}}{\partial\tilde{x}}\right]\right.$$

$$+\left(\frac{\partial\tilde{u}}{\partial\tilde{z}}\right)^2+\frac{1}{(L/\delta)^2}\left[\frac{1}{(L/\delta)^2}\left(\frac{\partial\tilde{w}}{\partial\tilde{x}}\right)^2+\left(\frac{\partial\tilde{u}}{\partial\tilde{x}}\right)^2+\left(\frac{\partial\tilde{w}}{\partial\tilde{z}}\right)^2+2\frac{\partial\tilde{u}}{\partial\tilde{z}}\frac{\partial\tilde{w}}{\partial\tilde{x}}\right]$$

$$\left.+\frac{1}{(L/\delta)^2}\left[\left(\frac{\partial\tilde{v}}{\partial\tilde{z}}\right)^2+\frac{1}{(L/\delta)^2}\left(\frac{\partial\tilde{w}}{\partial\tilde{y}}\right)^2+\left(\frac{\partial\tilde{w}}{\partial\tilde{z}}\right)^2+\left(\frac{\partial\tilde{v}}{\partial\tilde{y}}\right)^2+2\frac{\partial\tilde{w}}{\partial\tilde{y}}\frac{\partial\tilde{v}}{\partial\tilde{z}}\right]\right|^{\frac{n-1}{2}}. \tag{8.14}$$

Within the boundary layer, the inertial and viscous terms are of the same order of magnitude, gives us

$$\frac{a/\rho}{LU}\left(\frac{L}{\delta}\right)^2\sim 1,\ \left(\frac{\delta}{L}\right)^2\sim\frac{1}{\mathrm{Re}_a}\ \text{and}\ \frac{b/\rho}{L^nU^{2-n}}\left(\frac{L}{\delta}\right)^{n+1}\sim 1, \tag{8.15}$$

where $\mathrm{Re}_a=\dfrac{LU}{a/\rho}$. In the limit $\mathrm{Re}_a\to\infty$, Eqs. (8.11) to (8.14) asymptotically become

$$\tilde{u}\frac{\partial\tilde{u}}{\partial\tilde{x}}+\tilde{v}\frac{\partial\tilde{u}}{\partial\tilde{y}}+\tilde{w}\frac{\partial\tilde{u}}{\partial\tilde{z}}=-\frac{\partial\tilde{p}}{\partial\tilde{x}}+\frac{\partial^2\tilde{u}}{\partial\tilde{z}^2}+\frac{\partial}{\partial\tilde{z}}\left[\frac{\partial\tilde{u}}{\partial\tilde{z}}\left|\frac{\partial\tilde{u}}{\partial\tilde{z}}\right|^{n-1}\right], \tag{8.16}$$

$$\tilde{u}\frac{\partial\tilde{v}}{\partial\tilde{x}}+\tilde{v}\frac{\partial\tilde{v}}{\partial\tilde{y}}+\tilde{w}\frac{\partial\tilde{v}}{\partial\tilde{z}}=-\frac{\partial\tilde{p}}{\partial\tilde{y}}+\frac{\partial^2\tilde{v}}{\partial\tilde{z}^2}+\frac{\partial}{\partial\tilde{z}}\left[\frac{\partial\tilde{v}}{\partial\tilde{z}}\left|\frac{\partial\tilde{u}}{\partial\tilde{z}}\right|^{n-1}\right], \tag{8.17}$$

$$0=-\frac{\partial\tilde{p}}{\partial\tilde{z}}. \tag{8.18}$$

Eqs. (8.16) to (8.18) in dimensional form simplify to

$$u\frac{\partial u}{\partial x}+v\frac{\partial u}{\partial y}+w\frac{\partial u}{\partial z}=-\frac{\partial p}{\partial x}+a\frac{\partial^2 u}{\partial z^2}+b\frac{\partial}{\partial z}\left[\frac{\partial u}{\partial z}\left|\frac{\partial u}{\partial z}\right|^{n-1}\right], \tag{8.19}$$

$$u\frac{\partial v}{\partial x}+v\frac{\partial v}{\partial y}+w\frac{\partial v}{\partial z}=-\frac{\partial p}{\partial y}+a\frac{\partial^2 v}{\partial z^2}+b\frac{\partial}{\partial z}\left[\frac{\partial v}{\partial z}\left|\frac{\partial u}{\partial z}\right|^{n-1}\right], \tag{8.20}$$

$$0=-\frac{\partial p}{\partial z}. \tag{8.21}$$

8.1.2 Physical Model

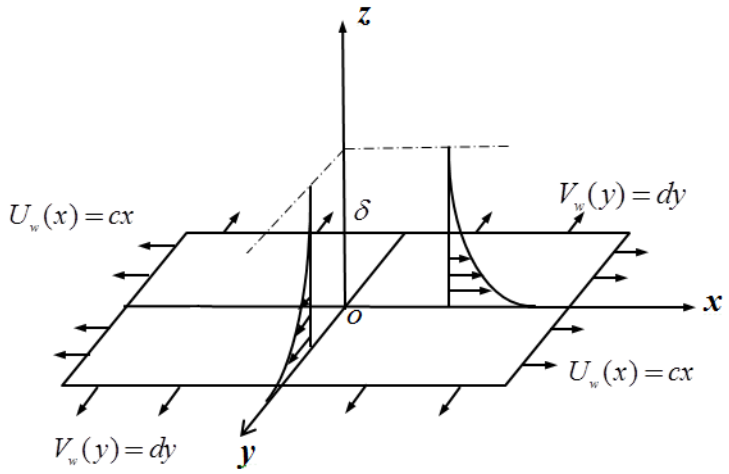

Figure 8.1: Physical model and coordinate system.

8.1.3 Governing Problem

Considering the three-dimensional steady, laminar and incompressible flow of fluid obeying the Sisko model which occupy space $z > 0$. The fluid is set into motion by an elastic flat sheet in the plane $z = 0$ kept at a constant temperature T_w, which is being continuously stretched with linear velocities *cx* and *dy* in the *x*-and *y*-directions, respectively. The constants c and d are positive real numbers relating to stretching of the sheet. The temperature far away from the sheet is uniform and taken as T_∞. In the present problem we have $\frac{\partial u}{\partial z} < 0$ as indicated by Mahapatra *et al.* [68]. The continuity, momentum and energy equations governing the steady three-dimensional flow of an incompressible Sisko fluid, approximated by boundary-layer theory are

$$\frac{\partial u}{\partial x} + \frac{\partial v}{\partial y} + \frac{\partial w}{\partial z} = 0, \tag{8.22}$$

$$\rho\left(u\frac{\partial u}{\partial x}+v\frac{\partial u}{\partial y}+w\frac{\partial u}{\partial z}\right)=a\frac{\partial^2 u}{\partial z^2}+b\frac{\partial}{\partial z}\left[\left(-\frac{\partial u}{\partial z}\right)^{n-1}\left(\frac{\partial u}{\partial z}\right)\right], \tag{8.23}$$

$$\rho\left(u\frac{\partial v}{\partial x}+v\frac{\partial v}{\partial y}+w\frac{\partial v}{\partial z}\right)=a\frac{\partial^2 v}{\partial z^2}+b\frac{\partial}{\partial z}\left[\left(-\frac{\partial u}{\partial z}\right)^{n-1}\frac{\partial v}{\partial z}\right], \tag{8.24}$$

$$u\frac{\partial T}{\partial x}+v\frac{\partial T}{\partial y}+w\frac{\partial T}{\partial z}=\frac{\kappa}{\rho c_p}\frac{\partial^2 T}{\partial z^2}. \tag{8.25}$$

Here (u,v,w) are velocity components, T the temperature, ρ the fluid density, c_p the specific heat of fluid at constant pressure and κ the thermal conductivity.

The boundary conditions associated to the present problem are given by

$$u=U_w(x)=cx,\ v=V_w(y)=dy,\ w=0,\ T=T_w \text{ at } z=0, \tag{8.26}$$

$$u\to 0, v\to 0, T\to T_\infty \text{ as } z\to\infty. \tag{8.27}$$

The momentum equations (8.23), (8.24) and energy equation (8.25) can be transformed into the corresponding ordinary differential equations by the following transformations

$$u=cxf'(\eta),\ v=cyg'(\eta),\ w=-c\left(\frac{c^{n-2}}{\rho/b}\right)^{1/(n+1)}\left(\frac{2n}{n+1}f+\frac{1-n}{1+n}\eta f'+g\right)x^{(n-1)/(n+1)},$$

$$\theta(\eta)=\frac{T(x,y,z)-T_\infty}{T_w-T_\infty},\ \eta=z\left(\frac{c^{2-n}}{b/\rho}\right)^{1/n+1}x^{(1-n)/(1+n)}. \tag{8.28}$$

Using transformations (8.28), we obtain

$$Af'''+n(-f'')^{n-1}f'''+\frac{2n}{n+1}ff''-(f')^2+gf''=0, \tag{8.29}$$

$$Ag'''+(-f'')^{n-1}g'''-(n-1)g''f'''(-f'')^{n-2}+\frac{2n}{n+1}fg''-(g')^2+gg''=0, \tag{8.30}$$

$$\theta'' + \Pr\left(\frac{2n}{n+1}\right) f\theta' + \Pr g\theta' = 0, \tag{8.31}$$

$$f(0) + g(0) = 0,\ f'(0) = 1,\ \mathrm{g}'(0) = d/c = \alpha,\ \theta(0) = 1, \tag{8.32}$$

$$f'(\eta) \to 0,\ \mathrm{g}'(\eta) \to 0 \text{ and } \theta(\eta) \to 0 \text{ as } \eta \to \infty, \tag{8.33}$$

with no loss of generality we can set

$$f(0) = 0 \text{ and } g(0) = 0. \tag{8.34}$$

Where the prime stands for differentiation with respect η and α is the stretching ratio parameter. We are considering the range $0 \le \alpha \le 1$, since for $\alpha > 1$, the x and y axes are interchanged [45]. Further, Re_a, Re_b are the local Reynolds numbers, A the material parameter of the Sisko fluid and Pr the generalized Prandtl number, which are defined as

$$\mathrm{Re}_a = \frac{\rho x U}{a},\ \mathrm{Re}_b = \frac{\rho x^n U^{2-n}}{b},\ A = \frac{\mathrm{Re}_b^{\frac{2}{n+1}}}{\mathrm{Re}_a} \text{ and } \Pr = \frac{xUR_b^{\frac{-2}{n+1}}}{\kappa/\rho c_p}. \tag{8.35}$$

Note that in the limit $\alpha \to 0$ the unidirectional stretching case is obtained and motion of fluid is merely in xz plane, i.e. g and g' in Eq. (8.28) both are zero. When $\alpha = 1$, the stretching rate is same in the *x*- and *y*- directions and the flow is axisymmetric.

8.2 Important Physical Parameters

From engineering point of view, the important characteristics of flow and heat transfer are, the local skin friction coefficients and the local Nusselt number, which are defined in the following paragraphs.

8.2.1 The Skin-friction Coefficients

The skin coefficient is an important boundary layer characteristic, which is the dimensionless shear stress at the wall $(z=0)$. Thus the dimensionless skin friction coefficients along the *x*- and *y*- directions, respectively, are given by

$$C_{fx}=\frac{\tau_{xz}\big|_{z=0}}{\frac{1}{2}\rho U_w^2} \text{ and } C_{fy}=\frac{\tau_{yz}\big|_{z=0}}{\frac{1}{2}\rho U_w^2}, \tag{8.36}$$

where τ_{xz} and τ_{yz} are shear stresses along the *x*- and *y*- directions, respectively.

These quantities in dimensionless form can be expressed as

$$\frac{1}{2}\mathrm{Re}_b^{1/(n+1)}C_{fx}=Af''(0)-[-f''(0)]^n, \tag{8.37}$$

and

$$\frac{1}{2}\mathrm{Re}_b^{1/(n+1)}C_{fy}=\frac{V_w}{U_w}\left[Ag''(0)+[-f''(0)]^{n-1}g''(0)\right]. \tag{8.38}$$

8.2.2 The Local Nusselt Number

The local Nusselt number denoted by Nu_x, giving the rate of heat transfer at the wall, is defined by

$$Nu_x=\left.\frac{xq_w}{\kappa\left(T_w-T_\infty\right)}\right|_{z=0}, \tag{8.39}$$

where the wall heat flux defined by $q_w=-\kappa\left(\frac{\partial T}{\partial y}\right)\Big|_{z=0}$ resulting in

$$\mathrm{Re}_b^{-1/n+1}Nu_x=-\theta'(0). \tag{8.40}$$

8.3 Methods of Solution

8.3.1 Method of Numerical Solution

Eqs. (8.29) to (8.31), along with boundary conditions given by Eqs. (8.32) and (8.33) constitute the nonlinear two-point boundary value problem and the exact solution does not seem to be possible for the complete set of equations. This fact forces us to obtain the solution of the problem numerically. Consequently, the resulting boundary value problem is solved numerically using adaptive Runge-Kutta method along with the shooting technique.

The system of nonlinear differential equations is solved as an initial value problem by writing it as a system of eight first order ordinary differential equations. Then a suitable finite value of the numerical infinity η_∞ is chosen for the particular set of the governing parameters to determine the velocity and temperature fields. To solve this initial value problem, the values of $f''(0)$, $g''(0)$ and $\theta'(0)$ are initially guessed and Runge–Kutta integration scheme is applied to get a solution. Then we compare the calculated values of $f'(\eta_\infty)$, $g'(\eta_\infty)$ and $\theta(\eta_\infty)$ with the given boundary conditions at infinity and adjust these values using Newton's method to get the better approximation for the result. The process is repeated till the solution correct up to the desired accuracy of 10^{-5} is obtained.

8.3.2 Method of Analytical Solution

The analytical results are sought using the homotopy analysis method (HAM) for certain values of parameters with a view to check the veracity of our numerical results. To apply the HAM, we selected the initial guesses agreeing the boundary data as

$$f_0 = 1 - e^{-\eta},\ g_0 = 1 - e^{-\eta} \text{ and } \theta_0 = e^{-\eta}, \tag{8.41}$$

and auxiliary linear operators

$$\mathrm{L}_f = f''' - f',\ L_g = g''' - g' \text{ and } L_\theta = \theta'' - \theta, \tag{8.42}$$

for the velocity and temperature fields, respectively.

The proper values of these convergence control parameters $\hbar_f, \hbar_g$ and $\hbar_\theta$ assure the convergence of the series solution. The optimal values of these parameters are chosen by minimizing the discrete squared residual error [75].

8.4 Validation of the Numerical Results

The validation of obtained results is essential to check the credibility of the numerical solution methodology. The presently computed results are compared with the analytical results obtained by the HAM. These comparison shows a very good agreement between the results obtained by the HAM and numerically (figure 8.2). Additionally, to verify the validity and accuracy of the present analysis a comparison between our numerical results and the results obtained through other techniques in the open literature is also presented through table 8.1 as a special case of the problem with an excellent agreement.

8.5 Graphical Results and Discussion

This chapter predominantly focuses the flow and heat transfer characteristics of Sisko fluid past a uniformly heated and bidirectional stretching surface. To grasp both the phenomena, Eqs. (8.29) to (8.31) with the boundary conditions (8.32) and (8.33) are solved numerically for non-integer values of the power-law index *n* and results are presented graphically. The effects of various parameters like the power-law index *n*,

material parameter A and stretching ratio parameter α are investigated for non-dimensional velocity components $f'(\eta), g'(\eta)$ and temperature $\theta(\eta)$. Variation of the local skin friction coefficients and local Nusselt number are also observed for different values of n and α.

Figures 8.3(a-d) present the effect of the stretching ratio parameter α on the velocity components $f'(\eta)$ and $g'(\eta)$ for Sisko fluid with shear thinning $(n=0.5)$ and shear thickening $(n=1.5)$ properties. It is evident from figure 8.3(a) that $f'(\eta)$ decreases with an increase in α, however, opposite behavior is observed for the $g'(\eta)$ component of the velocity (figure 8.3(b)). A comparison of figures 8.3(a,b) reveals that the stretching ratio parameter affects $g'(\eta)$ component more pronouncedly. Figures 8.3(c,d) show the same qualitative trends but there is noticeable decrease in boundary layer thickness for shear thickening fluid as compared to that of shear thinning fluid.

Figures 8.4(a-d) depict how the material parameter A affects the velocity profiles $f'(\eta)$ and $g'(\eta)$ for Sisko fluid with shear thinning and shear thickening properties. Figures 8.4(a,b) show that the velocities profiles increases monotonically with each increment of A. The rest of the figures show the same qualitative behavior. Again, figures 8.4(c,d) reveal that there is marked decrease in the boundary layer thickness for shear thickening fluids.

The influence of the stretching ratio parameter α on dimensionless temperature $\theta(\eta)$. From these figures a decrease in $\theta(\eta)$ is depicted through figures 8.5(a,b) is noticed for each increment in value of α. The effect is more noticeable for shear thinning fluid (figure 8.5(a)). Further, it is observed that the thermal boundary layer thickness is thin for shear thickening ($n=1.5$) fluid.

The following figures of temperature field are plotted and discussed for selected values of the Prandtl number Pr and the material parameter *A* of Sisko fluid as well as the stretching ratio parameter α. Figures 8.6(a-d) elucidate the effect of the Prandtl number Pr on temperature profile $\theta(\eta)$ for fixed values of the power-law index *n* and the stretching ratio parameter α. These figures reveal that the temperature profile decreases when Pr is increased. Further, figures 8.6(b,d) exhibit that there is a decrease in thermal boundary layer thickness at higher value of the stretching ratio parameter α.

To exhibit the effects of the material parameter *A* of Sisko fluid on non-dimensional temperature profile, we have plotted figures 8.7(a,b). These plots clearly show that the temperature profile decreases monotonically with increasing values of *A* for the shear thinning and shear thickening fluids. Again, it is noticed that the thermal boundary layer thickness is markedly reduced for shear-thickening (*n=1.5*) fluid. These figures also provide a comparison between the profiles of the power-law fluid (*A=0*) with those of the Sisko fluid ($A \neq 0$). From these figures, it is clear that the temperature profiles for the power law fluid is higher when compared with those of Sisko fluid.

Figure 8.8 graphs the relation between stretching ratio parameter α and total entrainment rate, which is proportional to $\mathrm{f}(\infty)+\mathrm{g}(\infty)$. This figure depicts that the quantity $\mathrm{f}(\infty)+\mathrm{g}(\infty)$ tends to increase monotonically, when α is varied from 0 to 1, both for the shear thinning and shear thickening Sisko fluids. The ambient flow rate entrained perpendicular to the stretching sheet is about 43% for shear thinning Sisko fluids, with axis symmetric stretching $(\alpha = 1)$ than with unidirectional stretching $(\alpha = 0)$. This quantity, however, is 63% higher for shear thickening Sisko fluids.

It is important to notice that Bingham plastic fluid model can be deduced when $n = 0$

in Eq. (8.5). Figures 8.9(a-c) show the velocity and temperature profiles of the Bingham plastic fluid for some values of the stretching ratio parameter. Whilst sketching these figures, the value of material parameter A is adjusted at 1.5. These figures clearly manifest that for the particular value of α, the velocity profile $f'(\eta)$ and temperature profile $\theta(\eta)$ attains the ambient values much deeper into the fluid as compared to those of the Sisko fluid.

The numerical values of the skin friction coefficients in the *x* and *y* directions are given in table 8.2. It is clear from this table that the skin friction drag is higher to some extent for the power-law index less than one. Moreover, it increases with an increase in value of the stretching ratio parameter α. Further, it is apparent that the increase is more rapid for the power-law index $n>1$. Table 8.3 presents the variation in wall temperature gradient $-\theta'(\eta)$ with the stretching ratio parameter α. It is observed that the value of $-\theta'(\eta)$ increases with each increment of α. This table depicts that the wall temperature gradient is higher for fluid with shear thickening properties and hence results in a higher heat transfer coefficient.

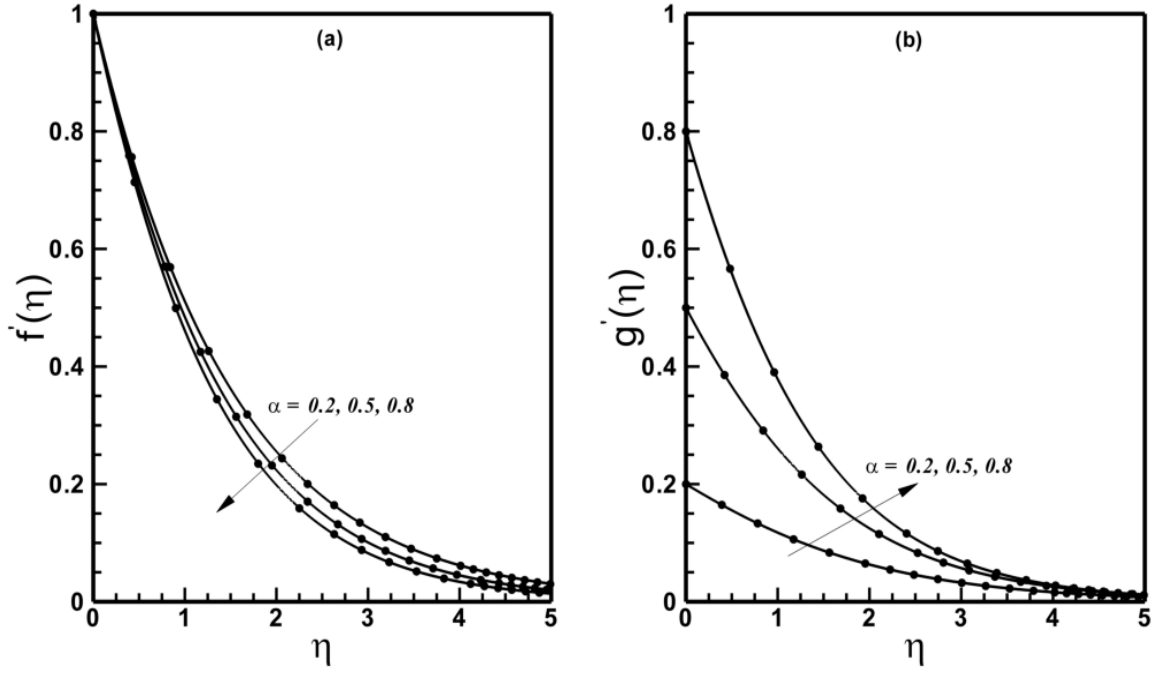

Figure 8.2: A comparison between the numerical and HAM results (solid lines numerical and solid circles HAM results) when $n = 1.0$ and $A = 1.5$ are fixed.

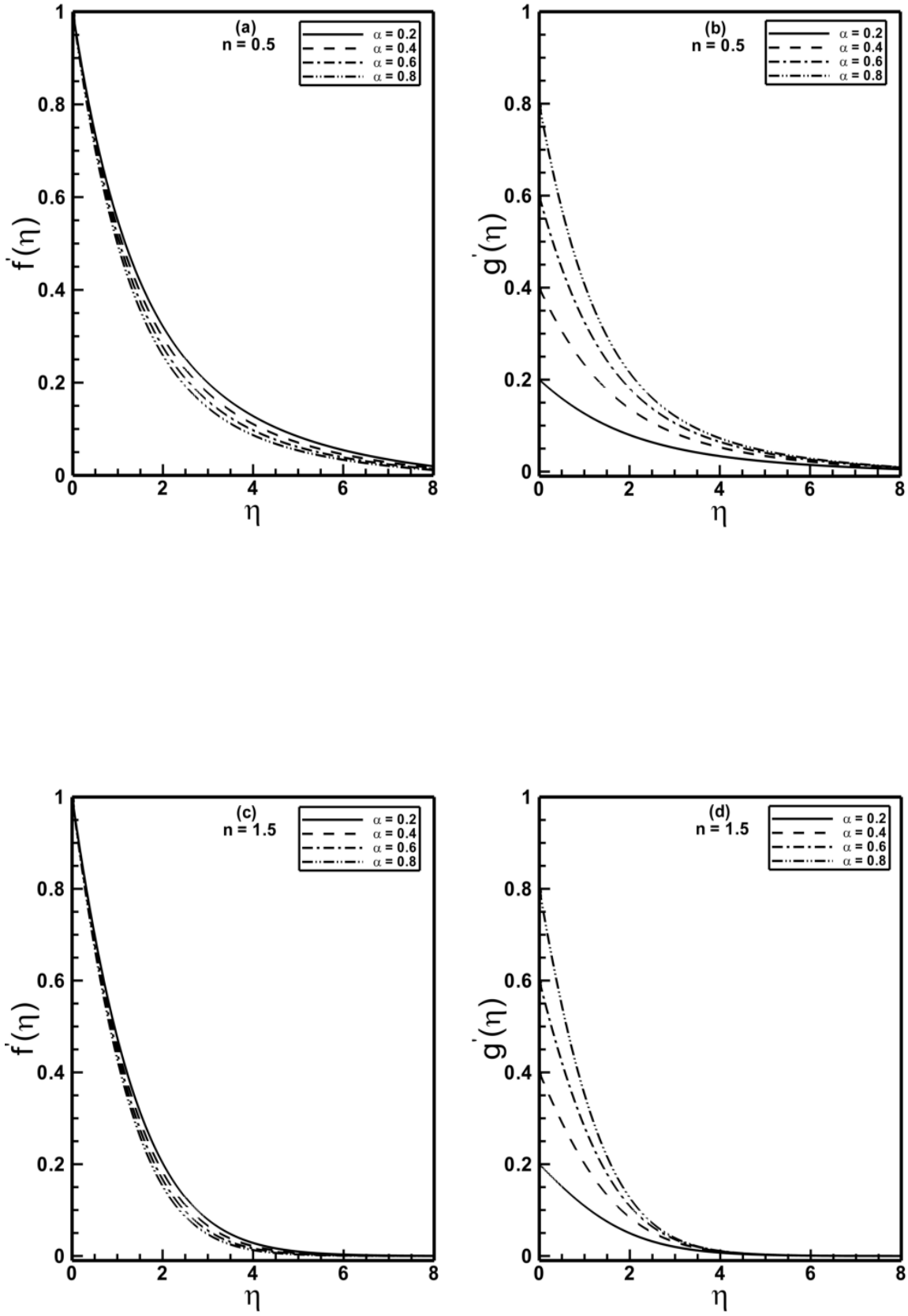

Figure 8.3: Profiles of the velocities $f'(\eta)$ and $g'(\eta)$ for different values of the stretching ratio parameter α when $A=1.5$ is fixed.

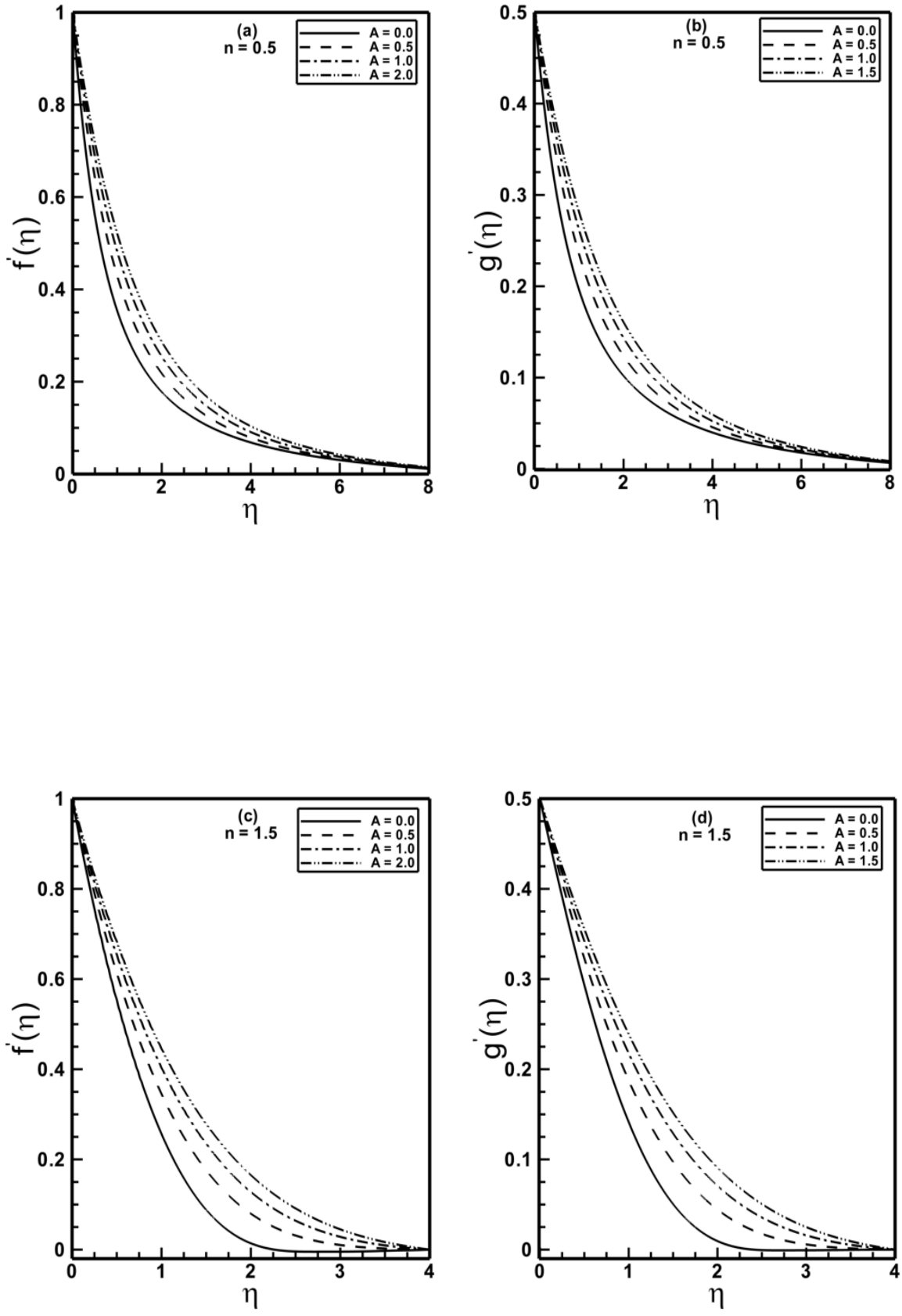

Figure 8.4: Profiles of the velocities $f'(\eta)$ and $g'(\eta)$ for different values of the material parameter A when $\alpha = 0.5$ is fixed.

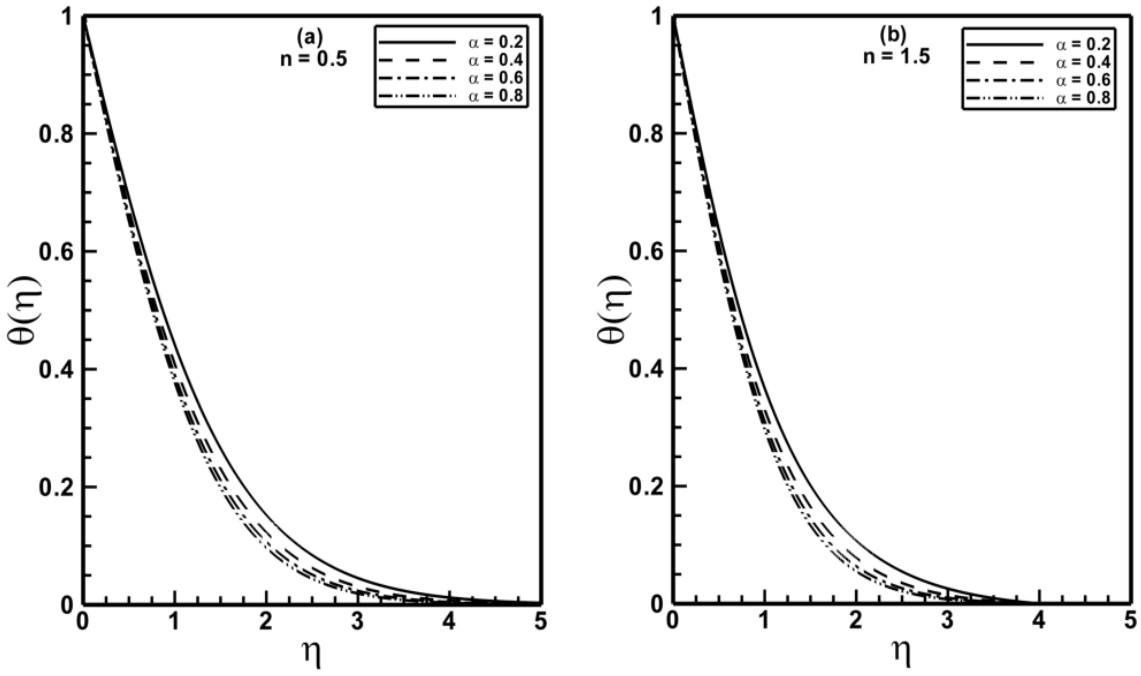

Figure 8.5: Profiles of the temperature $\theta(\eta)$ for different values of the stretching ratio parameter α when $A = 1.5$ and $\Pr = 2.0$ are fixed.

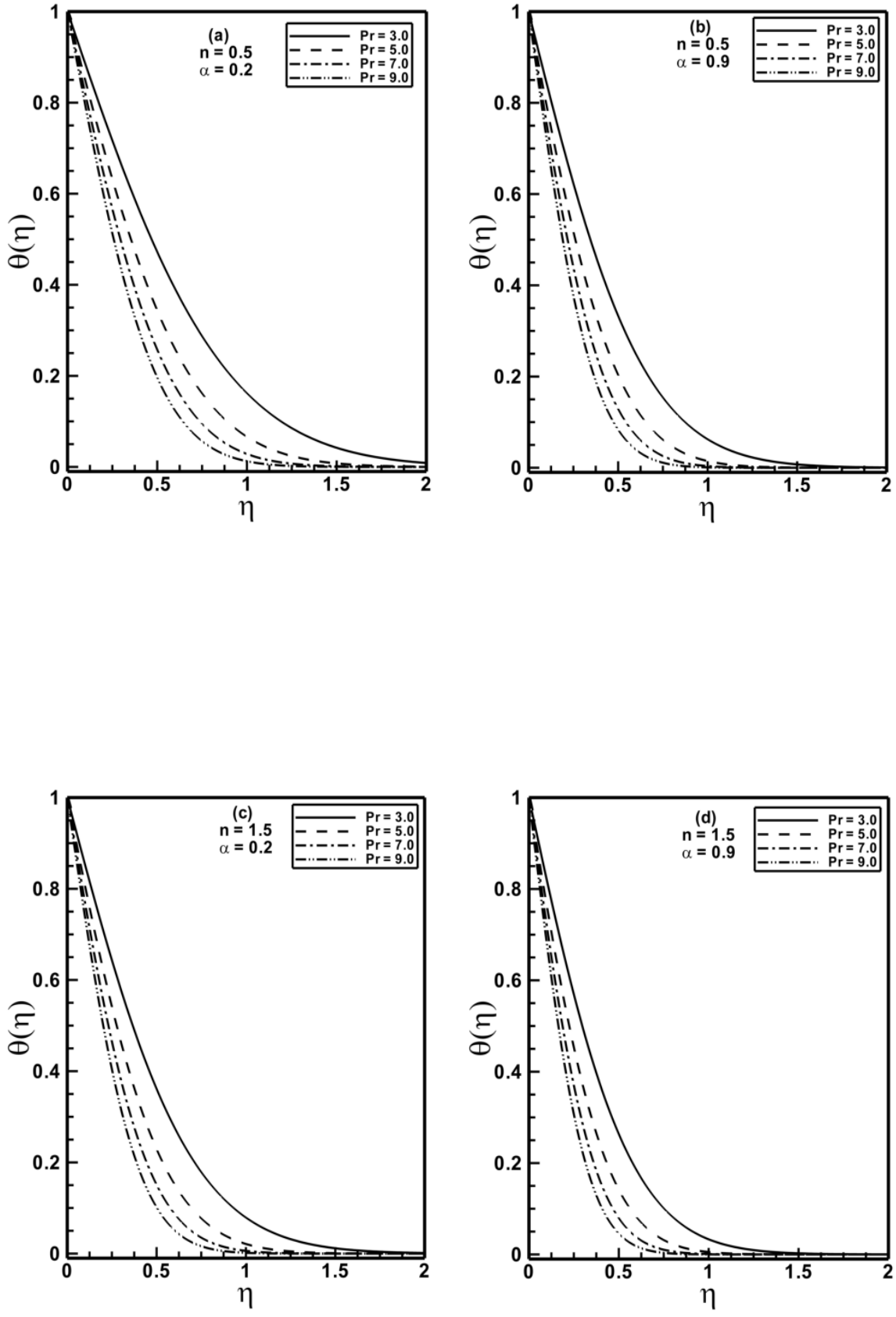

Figure 8.6: Profiles of the temperature $\theta(\eta)$ for different values of the Prandtl number Pr when $A=1.5$ is fixed.

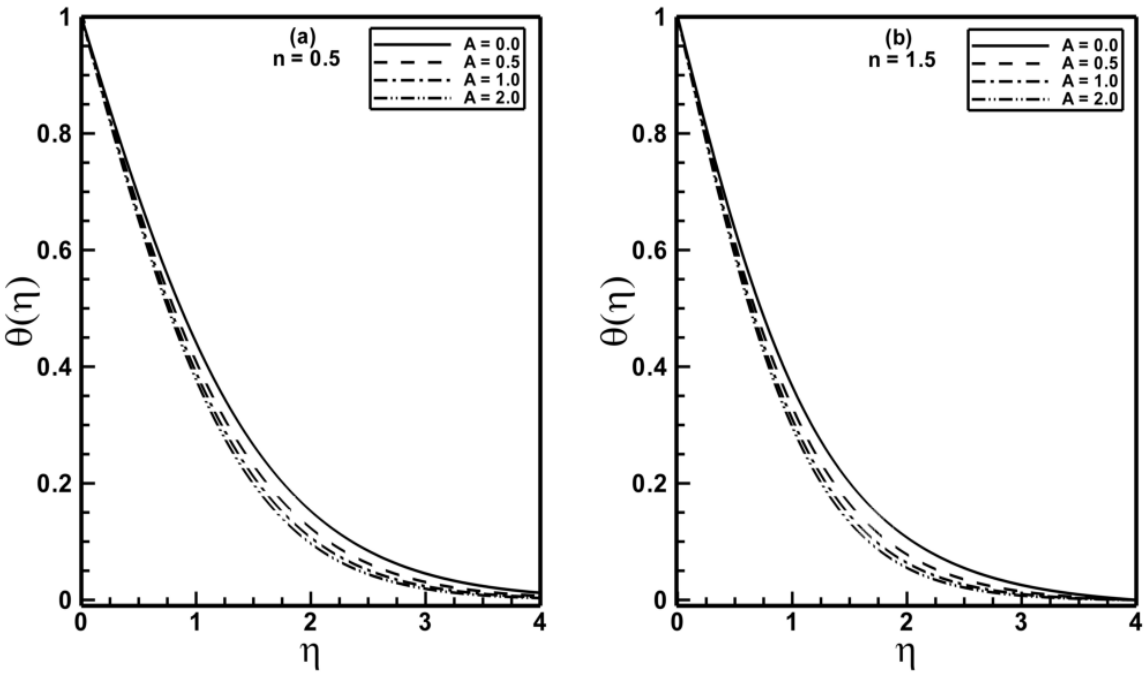

Figure 8.7: Profiles of the temperature $\theta(\eta)$ for different values of the material parameter A when $\alpha = 0.5$ and $\Pr = 2.0$ are fixed.

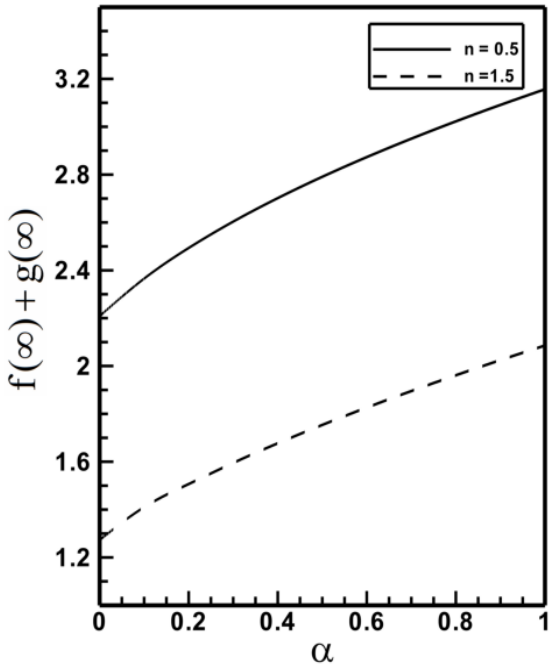

Figure. 8.8: Profiles of the entrainment velocity for different values of the power-law index n when $A = 1.5$ is fixed.

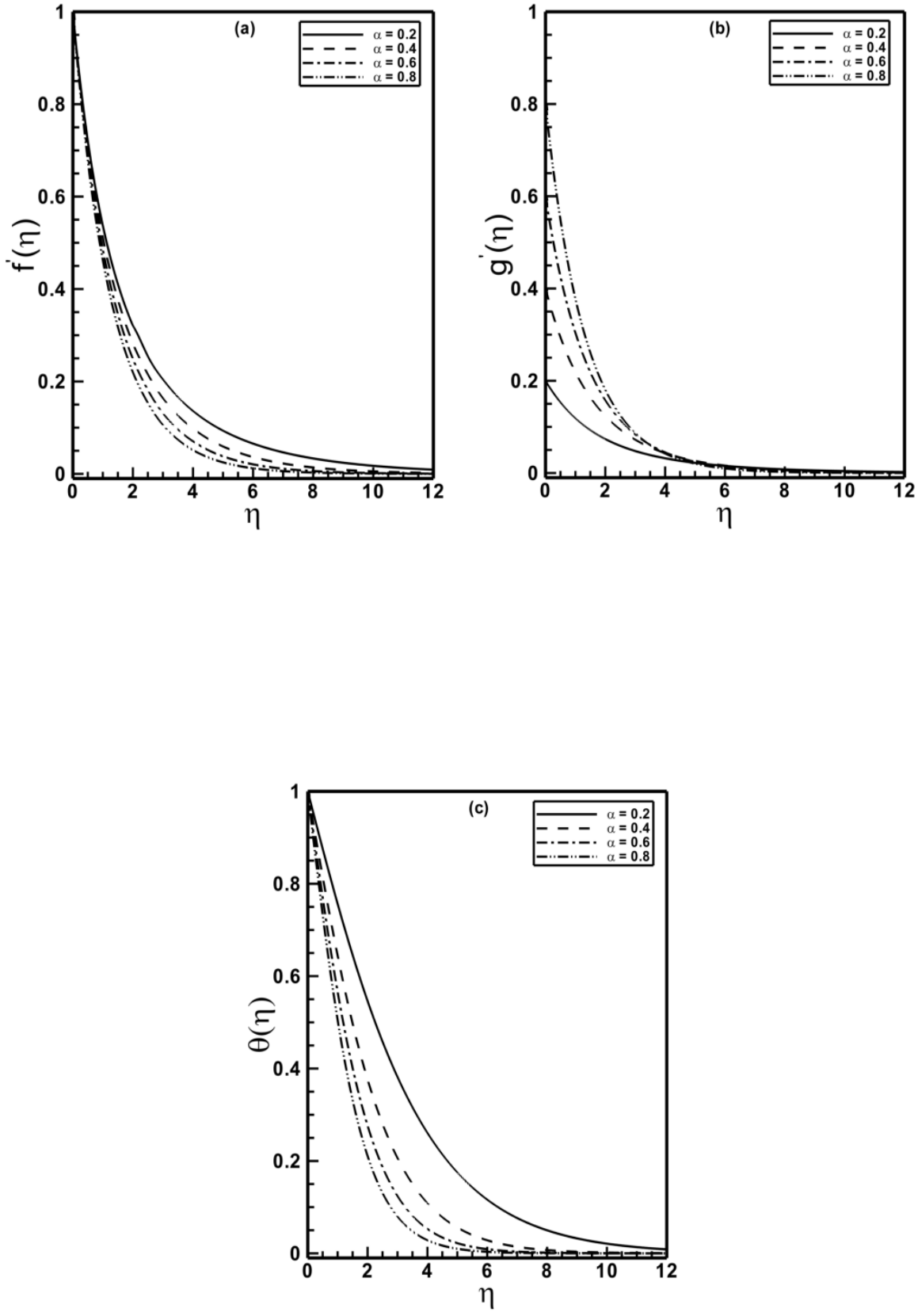

Figure 8.9: Profiles of the velocity $f'(\eta)$, $g'(\eta)$, and temperature $\theta(\eta)$ for Bingham plastic fluid for different stretching ratio parameter α when $n=0$, $A=1.5$ and $\Pr=2$ are fixed.

Table 8.1: A comparison of the local skin friction coefficient and local Nusselt number when $n=1$ and $A=0$ are fixed.

		$f''(0)$	$g''(0)$	$\theta'(0)$
Ref. [45]	$\alpha=0.0$	-1.00000	0	-
Ref. [47]		-1.00000	0	-
Present study		-1.00000	0	-
Ref. [45]	$\alpha=0.25$	-1.048813	-0.194564	-
Ref. [47]		-1.048813	-0.194565	-0.665933
Present study		-1.048818	-0.194567	-0.665939
Ref. [45]	$\alpha=0.50$	-1.093097	-0.465205	-
Ref. [47]		-1.093096	-0.465206	-0.735334
Present study		-1.093098	-0.465207	-0.735336
Ref. [45]	$\alpha=0.75$	-1.134485	-0.794622	-
Ref. [47]		-1.134486	-0.794619	-0.796472
Present study		-1.134487	-0.794619	-0.796472
Ref. [45]	$\alpha=1.0$	-1.173720	-1.173720	-
Ref. [47]		-1.173721	-1.173721	-
Present study		-1.173721	-1.173721	-

Table 8.2: A tabulation of the local skin friction coefficients along the *x*- and *y*-directions.

	$n=0.5$		$n=1.5$	
α	$\frac{1}{2}\mathrm{Re}_b^{1/(n+1)}C_{fx}$	$\frac{1}{2}\mathrm{Re}_b^{1/(n+1)}C_{fy}\left(\frac{U_w}{V_w}\right)$	$\frac{1}{2}\mathrm{Re}_b^{1/(n+1)}C_{fx}$	$\frac{1}{2}\mathrm{Re}_b^{1/(n+1)}C_{fy}\left(\frac{U_w}{V_w}\right)$
0.2	-1.74610	-0.24536	-1.60218	-0.23549
0.4	-1.79819	-0.57842	-1.66050	-0.55234
0.6	-1.84739	-0.97856	-1.71569	-0.93386
0.8	-1.89434	-1.43463	-1.76846	-1.37047

Table 8.3: A tabulation of the local Nusselt number when Pr=2 is fixed.

$\mathrm{Re}_b^{-1/(n+1)}\, Nu_x$		
α	$n=0.5$	$n=1.5$
0.2	-0.62074	-0.78919
0.4	-0.69468	-0.84864
0.6	-0.75957	-0.90287
0.8	-0.81827	-0.95324

Chapter 9

Flow and Heat Transfer to Sisko Fluid over a Rotating Disk

This chapter deals with study of the steady flow and heat transfer characteristics of Sisko fluid over a rotating infinite disk. The flow and heat transfer aspects are thoroughly investigated encompassing highly shear thinning/thickening Sisko fluids. The modeled boundary layer equations are reduced to a system of nonlinear ordinary differential equations using the appropriate transformation. The resulting equations are then solved numerically by single shooting method for shear thickening and multiple shooting method for shear thinning Sisko fluids in the domain $[0,\infty)$. The numerical data for the velocity and temperature fields are graphically sketched and effects of the relevant parameters are discussed in detail. In addition, the velocity gradients at the disk surface and the local Nusselt number for different values of the pertaining parameters are given in tabulated form. Moreover, a comparison with previously published work, as a special case of the problem, has been provided and the results are found to be in excellent agreement.

9.1 Mathematical Model and Formulation

9.1.1 Boundary Layer Equations

In this section, we have detailed the development of boundary layer equations for Sisko fluid over an infinite rotating disk. For mathematical modeling we take the cylindrical polar coordinate system (r,ϕ,z). For a three dimensional axisymmetric flow the velocity, stress and temperature fields have the form

$$\mathbf{V}=\left[u(r,\phi,z),v(r,\phi,z),w(r,\phi,z)\right],\ \mathbf{S}=\mathbf{S}(r,\phi,z),\ T=T(r,\phi,z), \tag{9.1}$$

where u, v and w are the radial, azimuthal and axial components of the velocity vector, respectively.

Now substituting Eq. (9.1) into Eqs. (3.1) to (3.3) along with Eq. (3.5) we get

$$\frac{\partial u}{\partial r}+\frac{u}{r}+\frac{\partial w}{\partial z}=0, \tag{9.2}$$

$$\rho\left(u\frac{\partial u}{\partial r}-\frac{v^2}{r}+w\frac{\partial u}{\partial z}\right)=-\frac{\partial p}{\partial r}+\frac{1}{r}\frac{\partial\left(rs_{rr}\right)}{\partial r}+\frac{\partial\left(s_{zr}\right)}{\partial z}-\frac{s_{\phi\phi}}{r}, \tag{9.3}$$

$$\rho\left(u\frac{\partial v}{\partial r}+\frac{uv}{r}+w\frac{\partial v}{\partial z}\right)=-\frac{\partial p}{\partial \phi}+\frac{1}{r^2}\frac{\partial\left(r^2s_{r\phi}\right)}{\partial r}+\frac{\partial\left(s_{z\phi}\right)}{\partial z}+\frac{s_{\phi r}-s_{r\phi}}{r}, \tag{9.4}$$

$$\rho\left(u\frac{\partial w}{\partial r}+w\frac{\partial w}{\partial z}\right)=-\frac{\partial p}{\partial z}+\frac{1}{r}\frac{\partial\left(rs_{rz}\right)}{\partial r}+\frac{\partial\left(s_{zz}\right)}{\partial z}, \tag{9.5}$$

$$\rho c_p\left(u\frac{\partial T}{\partial r}+w\frac{\partial T}{\partial z}\right)=\kappa\frac{\partial^2 T}{\partial z^2}+\frac{1}{r}\frac{\partial T}{\partial r}+\frac{\partial^2 T}{\partial r^2}, \tag{9.6}$$

$$\left.\begin{aligned}
&s_{\phi r}=s_{r\phi}=\left(a+b\left|\frac{1}{2}tr\mathbf{A}_1^2\right|^{\frac{n-1}{2}}\right)\left(\frac{\partial v}{\partial r}-\frac{v}{r}\right),\ s_{rr}=\left(a+b\left|\frac{1}{2}tr\mathbf{A}_1^2\right|^{\frac{n-1}{2}}\right)\left(2\frac{\partial u}{\partial r}\right),\\
&s_{zr}=s_{rz}=\left(a+b\left|\frac{1}{2}tr\mathbf{A}_1^2\right|^{\frac{n-1}{2}}\right)\left(\frac{\partial u}{\partial z}+\frac{\partial w}{\partial r}\right),\ s_{\phi\phi}=\left(a+b\left|\frac{1}{2}tr\mathbf{A}_1^2\right|^{\frac{n-1}{2}}\right)\left(2\frac{u}{r}\right),\\
&s_{z\phi}=s_{\phi z}=\left(a+b\left|\frac{1}{2}tr\mathbf{A}_1^2\right|^{\frac{n-1}{2}}\right)\left(\frac{\partial v}{\partial z}\right),\qquad s_{zz}=\left(a+b\left|\frac{1}{2}tr\mathbf{A}_1^2\right|^{\frac{n-1}{2}}\right)\left(2\frac{\partial w}{\partial z}\right),
\end{aligned}\right\} \tag{9.7}$$

$$\left|\frac{1}{2}tr\mathbf{A}_1^2\right|^{\frac{n-1}{2}} = \left|2\left(\frac{\partial u}{\partial r}\right)^2 + \left(\frac{\partial v}{\partial r} - \frac{v}{r}\right)^2 + \left(\frac{\partial u}{\partial z} - \frac{\partial w}{\partial r}\right)^2 + \left(\frac{\partial v}{\partial z}\right)^2 + 2\left(\frac{u}{r}\right)^2 + 2\left(\frac{\partial w}{\partial z}\right)^2\right|^{\frac{n-1}{2}}. \quad (9.8)$$

By assuming the symmetry about the axis of rotation $\left(\frac{\partial}{\partial \phi}(\cdot) = 0\right)$ [59] and introducing non-dimensional variables to deduce the boundary layer equations as

$$\tilde{u} = \frac{u}{R\Omega},\ \tilde{v} = \frac{v}{R\Omega},\ \tilde{w} = \frac{w}{\Omega\delta},\ \tilde{r} = \frac{r}{R},\ \tilde{z} = \frac{z}{\delta},\ \tilde{T} = \frac{T - T_\infty}{T_\infty},\ \tilde{p} = \frac{p - p_\infty}{\rho(R\Omega)^2}, \quad (9.9)$$

where Ω is the constant angular velocity about z- axis and R the appropriate length scale in (r, ϕ) plane.

Accordingly non-dimensional form of the above equations can be written as

$$\frac{\partial \tilde{u}}{\partial \tilde{r}} + \frac{\tilde{u}}{\tilde{r}} + \frac{\partial \tilde{w}}{\partial \tilde{z}} = 0, \quad (9.10)$$

$$\tilde{u}\frac{\partial \tilde{u}}{\partial \tilde{r}} + \tilde{w}\frac{\partial \tilde{u}}{\partial \tilde{z}} - \frac{\tilde{v}^2}{\tilde{r}} = -\frac{\partial \tilde{p}}{\partial \tilde{r}} + \frac{a/\rho}{\Omega R^2}\frac{\partial^2 \tilde{u}}{\partial \tilde{r}^2} + \frac{a/\rho}{\Omega R^2}\left(\frac{R}{\delta}\right)^2\frac{\partial^2 \tilde{u}}{\partial \tilde{z}^2} - \frac{a/\rho}{\Omega R^2}\frac{\tilde{u}}{\tilde{r}^2} + 2\frac{a/\rho}{\Omega R^2}\frac{\partial \tilde{u}}{\partial \tilde{r}}$$

$$+2\frac{b/\rho}{(\Omega R)^{2-n}R^n}\left(\frac{R}{\delta}\right)^{n+1}\frac{1}{(R/\delta)^2}\left[\frac{\partial}{\partial \tilde{r}}\left(\left(\frac{\partial \tilde{u}}{\partial \tilde{r}}\right)\tilde{J}\right) + \frac{1}{\tilde{r}}\left(\frac{\partial \tilde{u}}{\partial \tilde{r}}\right)\tilde{J} - \frac{\tilde{u}}{\tilde{r}^2}\tilde{J}\right]$$

$$+\frac{b/\rho}{(\Omega R)^{2-n}R^n}\left(\frac{R}{\delta}\right)^{n+1}\frac{\partial}{\partial \tilde{z}}\left[\left(\frac{\partial \tilde{u}}{\partial \tilde{z}} + \frac{1}{(R/\delta)^2}\frac{\partial \tilde{w}}{\partial \tilde{r}}\right)\tilde{J}\right], \quad (9.11)$$

$$\tilde{u}\frac{\partial \tilde{v}}{\partial \tilde{r}} + \tilde{w}\frac{\partial \tilde{v}}{\partial \tilde{z}} + \frac{\tilde{u}\tilde{v}}{\tilde{r}} = \frac{a/\rho}{\Omega R^2}\frac{\partial^2 \tilde{v}}{\partial \tilde{r}^2} + \frac{a/\rho}{\Omega R^2}\left(\frac{R}{\delta}\right)^2\frac{\partial^2 \tilde{v}}{\partial \tilde{z}^2} - \frac{a/\rho}{\Omega R^2}\frac{\tilde{v}}{\tilde{r}^2} + 2\frac{a/\rho}{\Omega R^2}\frac{1}{\tilde{r}}\frac{\partial \tilde{v}}{\partial \tilde{r}}$$

$$+2\frac{b/\rho}{(\Omega R)^{2-n}R^n}\left(\frac{R}{\delta}\right)^{n+1}\frac{1}{(R/\delta)^2}\left[\frac{\partial}{\partial \tilde{r}}\left(\left(\frac{\partial \tilde{v}}{\partial \tilde{r}} - \frac{\tilde{v}}{\tilde{r}}\right)\tilde{J}\right) + \frac{1}{\tilde{r}}\left(\frac{\partial \tilde{v}}{\partial \tilde{r}} - \frac{\tilde{v}}{\tilde{r}}\right)\tilde{J}\right]$$

$$+\frac{b/\rho}{(\Omega R)^{2-n}R^n}\left(\frac{R}{\delta}\right)^{n+1}\frac{\partial}{\partial \tilde{z}}\left[\left(\frac{\partial \tilde{v}}{\partial \tilde{z}}\right)\tilde{J}\right], \quad (9.12)$$

$$\frac{1}{(R/\delta)^2}\left(\tilde{u}\frac{\partial \tilde{w}}{\partial \tilde{r}} + \tilde{w}\frac{\partial \tilde{w}}{\partial \tilde{z}}\right) = -\frac{\partial \tilde{p}}{\partial \tilde{z}} + \frac{a/\rho}{\Omega R^2}\frac{\partial^2 \tilde{w}}{\partial \tilde{z}^2} + \frac{a/\rho}{\Omega R^2}\left(\frac{1}{R/\delta}\right)^2\frac{\partial^2 \tilde{w}}{\partial \tilde{r}^2} + \frac{a/\rho}{\Omega R^2}\frac{1}{\tilde{r}}\frac{\partial \tilde{u}}{\partial \tilde{z}}$$

$$+\frac{a/\rho}{\Omega R^2}\frac{1}{(R/\delta)^2}\frac{1}{\tilde{r}}\frac{\partial \tilde{w}}{\partial \tilde{r}} + \frac{b/\rho}{(\Omega R)^{2-n}R^n}\left(\frac{R}{\delta}\right)^{n+1}\frac{1}{(R/\delta)^2}\left[\frac{\partial}{\partial \tilde{r}}\left(\left(\frac{\partial \tilde{u}}{\partial \tilde{z}} + \frac{1}{(R/\delta)^2}\frac{\partial \tilde{w}}{\partial \tilde{r}}\right)\tilde{J}\right)\right.$$

$$+2\frac{\partial}{\partial\tilde{z}}\left(\left(\frac{\partial\tilde{w}}{\partial\tilde{z}}\right)\tilde{J}\right)+\left(\frac{\partial\tilde{u}}{\partial\tilde{z}}+\frac{1}{(R/\delta)^2}\frac{\partial\tilde{w}}{\partial\tilde{r}}\right)\tilde{J}\Bigg], \tag{9.13}$$

where

$$\tilde{J}=\left(\frac{R\Omega}{\delta}\right)^{n-1}\Bigg|\frac{1}{(R/\delta)^2}\Bigg[2\left(\frac{\partial\tilde{u}}{\partial\tilde{r}}\right)^2+\left(\frac{\partial\tilde{v}}{\partial\tilde{r}}\right)^2+\frac{1}{(R/\delta)^2}\left(\frac{\partial\tilde{w}}{\partial\tilde{r}}\right)^2+2\left(\frac{\partial\tilde{w}}{\partial\tilde{z}}\right)^2$$

$$+2\left(\frac{\partial\tilde{w}}{\partial\tilde{r}}\right)\left(\frac{\partial\tilde{u}}{\partial\tilde{z}}\right)-2\frac{\tilde{v}}{\tilde{r}}\frac{\partial\tilde{v}}{\partial\tilde{r}}+\left(\frac{\tilde{v}}{\tilde{r}}\right)^2+\left(\frac{\tilde{u}}{\tilde{r}}\right)^2\Bigg]+\left(\frac{\partial\tilde{u}}{\partial\tilde{z}}\right)^2+\left(\frac{\partial\tilde{v}}{\partial\tilde{z}}\right)^2\Bigg|^{\frac{n-1}{2}} \tag{9.14}$$

$$\tilde{u}\frac{\partial\tilde{T}}{\partial\tilde{r}}+\tilde{w}\frac{\partial\tilde{T}}{\partial\tilde{z}}=\frac{1}{\Omega R^2}\left(\frac{\kappa}{\rho c_p}\right)\left[\frac{\partial^2\tilde{T}}{\partial\tilde{z}^2}+\frac{1}{\tilde{r}}\frac{\partial\tilde{T}}{\partial\tilde{r}}+\left(\frac{R}{\delta}\right)^2\frac{\partial^2\tilde{T}}{\partial\tilde{r}^2}\right]. \tag{9.15}$$

Within the boundary layer the inertial and viscous terms have the same order of magnitude and these terms gives us

$$\frac{a/\rho}{\Omega R^2}\left(\frac{R}{\delta}\right)^2\sim 1,\ \left(\frac{\delta}{R}\right)^2\sim\frac{1}{\mathrm{Re}_a}\ \text{and}\ \frac{b/\rho}{R^n(\Omega R)^{2-n}}\left(\frac{R}{\delta}\right)^{n+1}\sim 1, \tag{9.16}$$

where $\mathrm{Re}_a=\dfrac{\Omega R^2}{a/\rho}$. In the limit $\mathrm{Re}_a\to\infty$, Eqs.(9.10) to (9.15) asymptotically become

$$\tilde{u}\frac{\partial\tilde{u}}{\partial\tilde{r}}+\tilde{w}\frac{\partial\tilde{u}}{\partial\tilde{z}}-\frac{\tilde{v}^2}{\tilde{r}}=-\frac{\partial\tilde{p}}{\partial\tilde{r}}+\frac{\partial^2\tilde{u}}{\partial\tilde{z}^2}+\frac{\partial}{\partial\tilde{z}}\left[\left(\frac{\partial\tilde{u}}{\partial\tilde{z}}\right)\Bigg|\left(\frac{\partial\tilde{u}}{\partial\tilde{z}}\right)^2+\left(\frac{\partial\tilde{v}}{\partial\tilde{z}}\right)^2\Bigg|^{\frac{n-1}{2}}\right], \tag{9.17}$$

$$\tilde{u}\frac{\partial\tilde{v}}{\partial\tilde{r}}+\tilde{w}\frac{\partial\tilde{v}}{\partial\tilde{z}}+\frac{\tilde{u}\tilde{v}}{\tilde{r}}=\frac{\partial^2\tilde{v}}{\partial\tilde{z}^2}+\frac{\partial}{\partial\tilde{z}}\left[\left(\frac{\partial\tilde{v}}{\partial\tilde{z}}\right)\Bigg|\left(\frac{\partial\tilde{u}}{\partial\tilde{z}}\right)^2+\left(\frac{\partial\tilde{v}}{\partial\tilde{z}}\right)^2\Bigg|^{\frac{n-1}{2}}\right], \tag{9.18}$$

$$0=-\frac{\partial\tilde{p}}{\partial\tilde{z}}, \tag{9.19}$$

and

$$\tilde{u}\frac{\partial\tilde{T}}{\partial\tilde{r}}+\tilde{w}\frac{\partial\tilde{T}}{\partial\tilde{z}}=\frac{\kappa}{\rho c_p}\frac{\partial^2\tilde{T}}{\partial\tilde{z}^2}. \tag{9.20}$$

The above equations in dimensional form turn out to be the following:

$$\frac{\partial u}{\partial r}+\frac{u}{r}+\frac{\partial w}{\partial z}=0, \tag{9.21}$$

$$u\frac{\partial u}{\partial r}+w\frac{\partial u}{\partial z}-\frac{v^2}{r}=-\frac{\partial p}{\partial r}+a\frac{\partial^2 u}{\partial z^2}+b\frac{\partial}{\partial z}\left[\left(\frac{\partial u}{\partial z}\right)\left|\left(\frac{\partial u}{\partial z}\right)^2+\left(\frac{\partial v}{\partial z}\right)^2\right|^{\frac{n-1}{2}}\right], \tag{9.22}$$

$$u\frac{\partial v}{\partial r}+w\frac{\partial v}{\partial z}+\frac{uv}{r}=a\frac{\partial^2 v}{\partial z^2}+b\frac{\partial}{\partial z}\left[\left(\frac{\partial v}{\partial z}\right)\left|\left(\frac{\partial u}{\partial z}\right)^2+\left(\frac{\partial v}{\partial z}\right)^2\right|^{\frac{n-1}{2}}\right], \tag{9.23}$$

$$0=-\frac{\partial p}{\partial z}, \tag{9.24}$$

$$u\frac{\partial T}{\partial r}+w\frac{\partial T}{\partial z}=\frac{\kappa}{\rho c_p}\frac{\partial^2 T}{\partial z^2}. \tag{9.25}$$

9.1.2 Physical Model

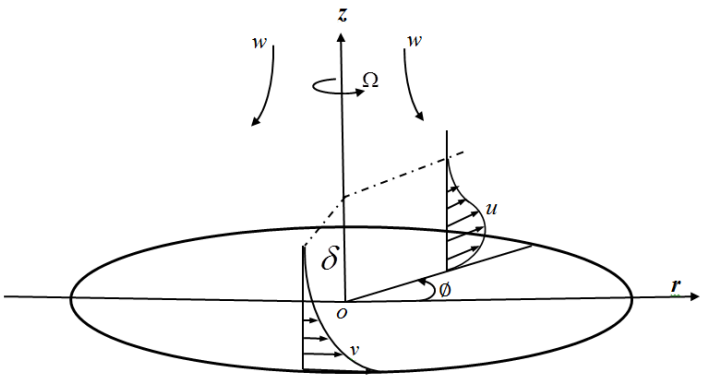

Figure 9.1: Physical model and coordinate system.

9.1.3 Governing Problem

Here we will consider the steady axisymmetric flow of a Sisko fluid over an infinite disk rotating with a sufficiently high constant angular velocity Ω, so that effects of gravitational force on momentum transfer are rather low. The disk coincides with the plane $z=0$ and the motion of the fluid is confined in the half space $z>0$. In a cylindrical coordinates system, the disk rotates around its axis of symmetry coinciding with the z-

axis. The disk is kept at a constant temperature T_w and the fluid outside the boundary layer is maintained at a uniform temperature T_∞. The physical model in cylindrical polar coordinate system is shown in figure 9.1 while the governing boundary layer equations take the form

$$u\frac{\partial u}{\partial r}+w\frac{\partial u}{\partial z}-\frac{v^2}{r}=-\frac{\partial p}{\partial r}+a\frac{\partial^2 u}{\partial z^2}+b\frac{\partial}{\partial z}\left[\left(\frac{\partial u}{\partial z}\right)\left\{\left(\frac{\partial u}{\partial z}\right)^2+\left(\frac{\partial v}{\partial z}\right)^2\right\}^{\frac{n-1}{2}}\right], \tag{9.26}$$

$$u\frac{\partial v}{\partial r}+w\frac{\partial v}{\partial z}+\frac{uv}{r}=a\frac{\partial^2 v}{\partial z^2}+b\frac{\partial}{\partial z}\left[\left(\frac{\partial v}{\partial z}\right)\left\{\left(\frac{\partial u}{\partial z}\right)^2+\left(\frac{\partial v}{\partial z}\right)^2\right\}^{\frac{n-1}{2}}\right], \tag{9.27}$$

$$u\frac{\partial T}{\partial r}+w\frac{\partial T}{\partial z}=\frac{\kappa}{\rho c_p}\frac{\partial^2 T}{\partial z^2}. \tag{9.28}$$

The boundary conditions relating to the flow and temperature fields are

$$u=w=0,\ v=\Omega r \text{ and } T=T_w \text{ at } z=0, \tag{9.29}$$

$$u,\ v\to 0 \text{ and } T\to T_\infty \text{ as } z\to+\infty. \tag{9.30}$$

Now employing Von Ka′rma′n type of the velocity field and using the dimensionless variables defined by

$$\left.\begin{aligned}\eta&=z\left(\frac{\Omega^{2-n}}{b/\rho}\right)^{1/(n+1)}r^{(1-n)/(1+n)},\ u=r\Omega f(\eta),\ v=r\Omega g(\eta),\\ w&=\left(\frac{\Omega^{1-2n}}{b/\rho}\right)^{-1/(n+1)}r^{(n-1)/(n+1)}h(\eta),\text{ and }\theta(\eta)=\frac{T-T_\infty}{T_w-T_\infty}.\end{aligned}\right\} \tag{9.31}$$

Utilizing the variables defined in Eq. (9.31), the boundary layer Eqs. (9.26) to (9.30), in the absence of radial pressure gradient [59] can be written as

$$h'=-2f-\frac{1-n}{1+n}\eta f', \tag{9.32}$$

$$Af'' + \left[f'\left(f'^2 + g'^2 \right)^{\frac{n-1}{2}} \right]' = f^2 - g^2 + \left[\eta\left(\frac{1-n}{1+n} \right) f + h \right] f', \tag{9.33}$$

$$Ag'' + \left[g'\left(f'^2 + g'^2 \right)^{\frac{n-1}{2}} \right]' = 2fg + \left[\eta\left(\frac{1-n}{1+n} \right) f + h \right] g', \tag{9.34}$$

$$\theta''\left(f'^2 + g'^2 \right)^{\frac{n-1}{2}} + (n-1)\theta'\left(ff'' + g'g'' \right)\left(f'^2 + g'^2 \right)^{\frac{n-3}{2}} = \Pr\left(\frac{1-n}{1+n}\eta f + h \right)\theta'. \tag{9.35}$$

The transformed boundary conditions are

$$f = h = 0,\ g = \theta = 1 \text{ at } \eta = 0, \tag{9.36}$$

$$f = 0,\ g = 0 \text{ and } \theta = 0 \text{ as } \eta \to \infty. \tag{9.37}$$

9.2 Numerical Solution of the Problem

The exact and/or closed form solution of nonlinear ordinary differential equations is not always straightforward to obtain. So, one has to recourse to the numerical solution of transformed ordinary differential equations, with the associated boundary conditions. Eqs. (9.32) to (9.35), alongside the boundary conditions (9.36) and (9.37) constitute a two-point boundary value problem and are solved by employing shooting method using adaptive Runge Kutta quadrature with Newton's method in the domain $[0,\infty)$. These equations are written as an equivalent first order system in η as follows:

$$f' = p, \tag{9.38}$$

$$p' = q, \tag{9.39}$$

$$\theta' = t, \tag{9.40}$$

$$N_1 = (n-1)pq\left(p^2+q^2\right)^{\frac{n-3}{2}}\left[2fg+\left\{h+\eta\left(\frac{1-n}{1+n}\right)f\right\}q\right]$$

$$+\left(f^2-g^2\right)\left[A+\left(p^2+q^2\right)^{\frac{n-1}{2}}+(n-1)q^2\left(p^2+q^2\right)^{\frac{n-3}{2}}\right]$$

$$+p\left[\eta\left(\frac{1-n}{1+n}\right)f+h\right]\left[A+\left(p^2+q^2\right)^{\frac{n-1}{2}}+(n-1)\left(p^2+q^2\right)^{\frac{n-3}{2}}\right], \tag{9.41}$$

$$N_2 = (n-1)pq\left(p^2+q^2\right)^{\frac{n-3}{2}}\left[\left(f^2-g^2\right)+\left\{h+\eta\left(\frac{1-n}{1+n}\right)f\right\}p\right]$$

$$+2fg\left[A+\left(p^2+q^2\right)^{\frac{n-1}{2}}+(n-1)p^2\left(p^2+q^2\right)^{\frac{n-3}{2}}\right]$$

$$+q\left[\eta\left(\frac{1-n}{1+n}\right)f+h\right]\left[A+\left(p^2+q^2\right)^{\frac{n-1}{2}}+(n-1)p^2\left(p^2+q^2\right)^{\frac{n-3}{2}}\right], \tag{9.42}$$

$$D=\left[A+\left(p^2+q^2\right)^{\frac{n-1}{2}}\right]^2-\left[(n-1)pq\left(p^2+q^2\right)^{\frac{n-3}{2}}\right]^2$$

$$+(n-1)^2\left(pq\right)^2\left(p^2+q^2\right)^{n-3}+\left[A+\left(p^2+q^2\right)^{\frac{n-1}{2}}\right]\left[(n-1)\left(p^2+q^2\right)^{\frac{n-1}{2}}\right], \tag{9.43}$$

$$p'=\frac{N_1}{D}, \tag{9.44}$$

$$q'=\frac{N_2}{D}, \tag{9.45}$$

$$t'=\left(p^2+q^2\right)^{\frac{1-n}{2}}\left[(1-n)t\left(p^2+q^2\right)^{\frac{n-3}{2}}\left(pp'+qq'\right)+\Pr\left\{\left(\frac{1-n}{1+n}\right)\eta f+h\right\}t\right]. \tag{9.46}$$

The corresponding boundary conditions are

$$f(0)=0,\ g(0)=1,\ h(0)=0 \text{ and } \theta(0)=1, \tag{9.47}$$

$$f\to 0,\ g\to 0,\ \theta\to 0 \text{ as } \eta\to\infty. \tag{9.48}$$

The simple shooting method failed due to instability problem for the value of the power-law index $n < 0.8$. We have to recourse to a better approach, such as multiple shooting method. In the multiple shooting method, one can circumvent the difficulty of instability by introducing intermediate shooting nodes

$$0 < \eta_1 < \ldots < \eta_{N-1} < \eta_N = \eta_\infty, \tag{9.49}$$

and solving the initial value problem on each sub-intervals $\left[\eta_j, \eta_{j+1}\right]$, $j = 0,1,\ldots,N-1$. A step size of $\Delta\eta = 0.001$ is found to be satisfactory in obtaining accuracy within a tolerance of less than 10^{-6}. One has to adopt larger number of nodes for smaller values of the power-law index $(n \leq 0.3)$.

9.3 Validation of Numerical Results

Checking the credibility of our numerical predictions is strongly recommended in any case. The present results are compared with the previously published literature as a special case of our problem. Tables 9.1(a-c) present the gradient of radial and azimuthal velocity at the wall, as computed in present special case, predicted by Andersson *et al.* [59] and obtained by Mitschka and Ulbrecht (M&U) [77]. A good agreement in these results enhances the veracity of our results. Further, Table 9.1(c) shows the axial velocity field far from the rotating disk as depicted by our computations and demonstrated in [59]. An encouraging comparison is observed in this case too.

9.4 Numerical Results and Discussion

To get the physical insight of the problem, the coupled nonlinear ordinary differential equations (9.32) to (9.35) subject to boundary conditions (9.36) and (9.37) have been

solved numerically. The effects of pertinent non-dimensional parameters influencing the flow and temperature fields to Sisko fluid over a rotating infinite disk with their respective ranges focused are: the power-law index ($0.3 \le n \le 1.9$), the material parameter of Sisko fluid ($0.5 \le A \le 2$), and Prandtl number ($1 \le \mathrm{Pr} \le 4$).

Figures (9.2) to (9.12) display the numerical data generated for the flow and temperature fields; the flow field include the radial $f(\eta)$, azimuthal $g(\eta)$ and axial $h(\eta)$ components of velocity field. The entire velocity field for the shear thinning ($n<1$) and shear thickening ($n>1$) Sisko fluids are presented in figures (9.2) to (9.4). On inspection of figures 9.2 (a,b) it is obvious that the radial velocity decreases as the value of the power-law index incremented progressively. A peak near the disk is observed due to the presence of centrifugal force; a slight variation in peak is observed for shear thinning and shear thickening fluids; however, the velocity profile is unaffected in the vicinity of the disk. Figures 9.3(a,b) show the profiles of azimuthal component $g(\eta)$ of the velocity field for different values of the power-law index n. The velocity approaches the asymptotic value, monotonically for each value of n. The velocity also decreases with each increment of n due to increase in viscous forces. Further, the velocity profiles become closer as the value of the power-law index is extended beyond $n>1$. The variation in axial flow $h(\eta)$ is sketched in figures 9.4(a,b) for different values of the power-law index n. The axial flow decreases as the value of n is incremented due to the fact that the radial velocity component decreases as the value of n is increased. Further, this figure also depicts that for highly shear thinning fluid the value of $h(\eta)$ fails to approach an asymptotic limit as attained by other two components $f(\eta)$ and $g(\eta)$ for large value of η. It can be attributed to the deterioration of numerical accuracy caused by the thickening of boundary layer.

The heat transfer aspects of the Sisko fluid over a rotating constant surface temperature disk possessing constant surface temperature for shear thinning and thickening fluids for different values of the power-law index n is illustrated in figures 9.5(a,b). Figure 9.5(a) depicts that the temperature profile and thermal boundary layer reduce with incrementing value of the power-law index $n<1$. The effect on the temperature profile diminishes when the power-law index approaches unity. Figure 9.5(b) reveals that the power-law index n does not affect the temperature profile as strongly as for shear thinning fluids. However, a decrease in the thermal boundary layer thickness is observed and temperature profiles become closer as the value of n is incremented.

To exhibit the effects of variation in the material parameter A of Sisko fluid on non-dimensional velocities $f(\eta)$, $g(\eta)$ and $h(\eta)$ profiles, we have plotted figures 9.6 to 9.8. These figures show that the velocity increases as the value of A is augmented. For shear thickening Sisko fluid (panel b), the material parameter A of Sisko fluid affects more strongly in contrast to the shear thinning fluid (panel a). Figure 9.8(a) shows that for increasing values of A, the axial velocity fails to approach the asymptotic value. In contrast, this velocity component fairly approaches its asymptotic value for shear thickening Sisko fluids (figure 9.8b). Figures 9.9(a,b) illustrate the effect of the material parameter A of Sisko fluid on temperature field. These figures show that temperature profile is not considerably affected by the variation in A; nevertheless, the temperature is slightly lowered when value of A is increased progressively.

The Prandtl number Pr of a fluid plays a vital role in forced convective heat transfer. Figures 9.10(a,b) present its effect on heat transfer to Sisko fluid for shear thinning and shear thickening regimes. These figures depict that increasing value of Pr, affects the heat transfer process strongly by thinning the thermal boundary layer thickness. It in turn

augments the heat transfer at the wall. The augmentation can be ascribed to the enhanced momentum diffusivity for larger Prandtl number. The temperature profile is slightly lower for fluids with shear thickening behavior than that of the shear thinning for same Prandtl number.

Lastly, figures 9.11 and 9.12 make a comparison amongst the velocities and temperature profiles of the Newtonian fluid $(A=0$ and $n=1)$ and the power-law fluid $(A=0$ and $n\neq 1)$ with those of the Sisko fluid $(A\neq 0)$. Figures 9.11(a-c) reveal that the velocity distribution for the Newtonian and the power-law $(n=1.2)$ fluids are close to each other, but that of Sisko fluid has a thick boundary layer. One can deduce that the material parameter A of Sisko fluid has a decisive influence on the boundary layer thickness. The thermal boundary layer thickness for the Sisko and the power-law fluids is thin as compare to that of the Newtonian fluid. But thermal boundary layer thickness in not much altered by the material parameter of Sisko fluid.

Table 9.2 summarizes the overall trends in the radial and azimuthal velocity gradients at the disk, based on the variation in the power-law index n. This table shows that the velocity gradients at the disk increases, but that is not a strong function of n. Further, this table also depicts that axial velocity is heavily dependent on n, and decreases as the value of the power-law index n is augmented due to decrease in the radial component of velocity. The effect of variation in the Prandtl number Pr on the temperature gradient at the disk surface is outlined in table 9.3. It can be noted that the temperature gradient increases with rise in Pr; thereby increasing the heat transfer at the surface of the disk.

Table 9.1(a): A comparison of the radial velocity gradient at wall when $A=0$ is fixed.

Power-law index	$f'(0)$		
n	Present result	Andersson *et al.* [59]	M&U [77]
0.2	0.529	0.532	0.528
0.4	0.504	-	0.504
0.5	0.501	0.501	0.501
0.6	0.501	0.501	0.500
0.8	0.504	0.504	0.504
0.9	0.507	0.507	0.507
1.0	0.510	0.510	0.510
1.3	0.521	0.522	0.521
1.5	0.529	0.529	0.529
1.7	0.537	0.537	-

Table 9.1(b): A comparison of the azimuthal velocity gradient at wall when $A=0$ is fixed.

Power law index	$-g'(0)$		
n	Present results	Andersson *et al.*[59]	M&U [77]
0.2	1.034	1.032	1.037
0.4	0.769	-	0.769
0.5	0.713	0.712	0.713
0.6	0.678	0.676	0.677
0.8	0.636	0.636	0.636
0.9	0.624	0.624	0.624
1.0	0.616	0.616	0.616
1.3	0.603	0.603	0.603
1.5	0.601	0.601	0.601
1.7	0.601	0.600	-

Table 9.1(c): A comparison of the axial velocity when $A = 0$ is fixed.

Power law index	$-h(\infty)$		
n	Present results	Andersson *et al.* [59]	M&U [77]
0.2	-	-	-
0.4	-	-	-
0.5	1.543	1.539	1.513
0.6	1.430	1.364	1.351
0.8	1.089	1.089	1.052
0.9	0.970	0.969	0.958
1.0	0.884	0.883	-
1.3	0.736	0.735	0.735
1.5	0.678	0.676	0.678
1.7	0.637	0.633	-

Table 9.2: A tabulation of some characteristics of flow when $A = 1.5$ is fixed.

n	$f'(0)$	$-g'(0)$	$-h(\infty)$
0.4	0.29599	0.38973	2.57607
0.6	0.30717	0.38534	1.92475
0.8	0.31559	0.38605	1.54620
1.2	0.32895	0.39443	1.32478
1.4	0.33452	0.39995	1.28217
1.6	0.33951	0.40570	1.25597
1.8	0.34395	0.41146	1.23178

Table 9.3: A tabulation of the temperature gradient at wall, when $A=1.5$ fixed.

	$-\theta'(0)$	
Pr	$n=0.5$	$n=1.5$
3.0	0.57042	0.71071
5.0	0.68979	0.87693
7.0	0.77976	1.00293
9.0	0.85363	1.10669

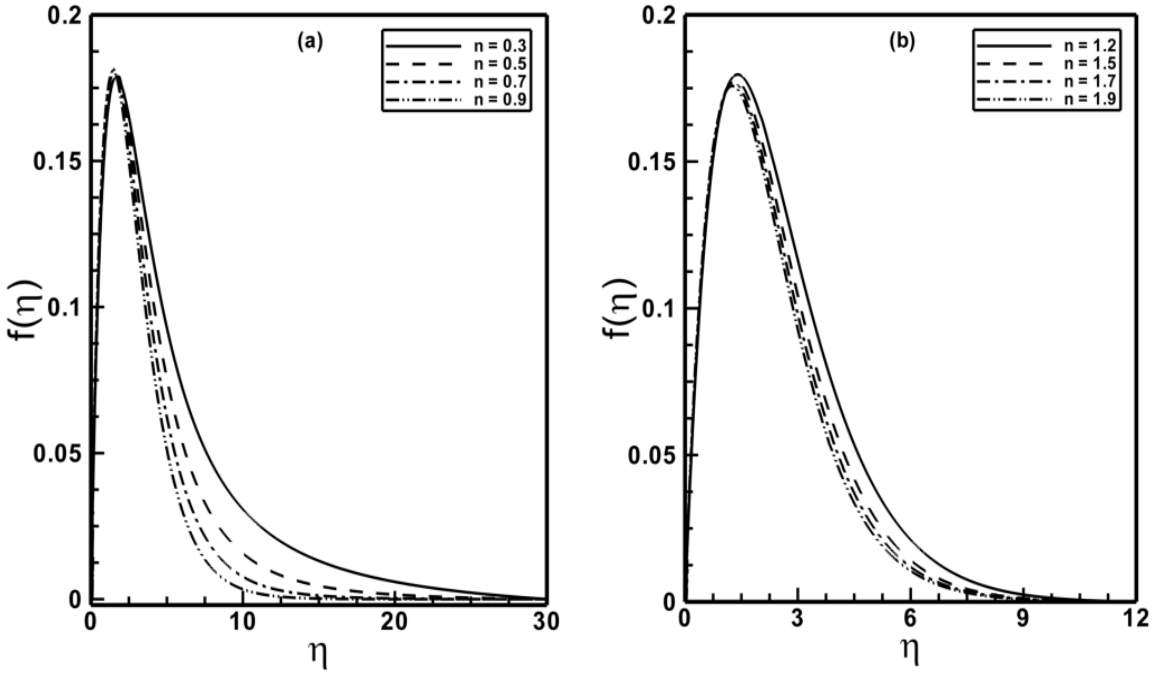

Figure 9.2: Profiles of the radial velocity component $f(\eta)$ for different values of the power-law index when $A=1.5$ is fixed.

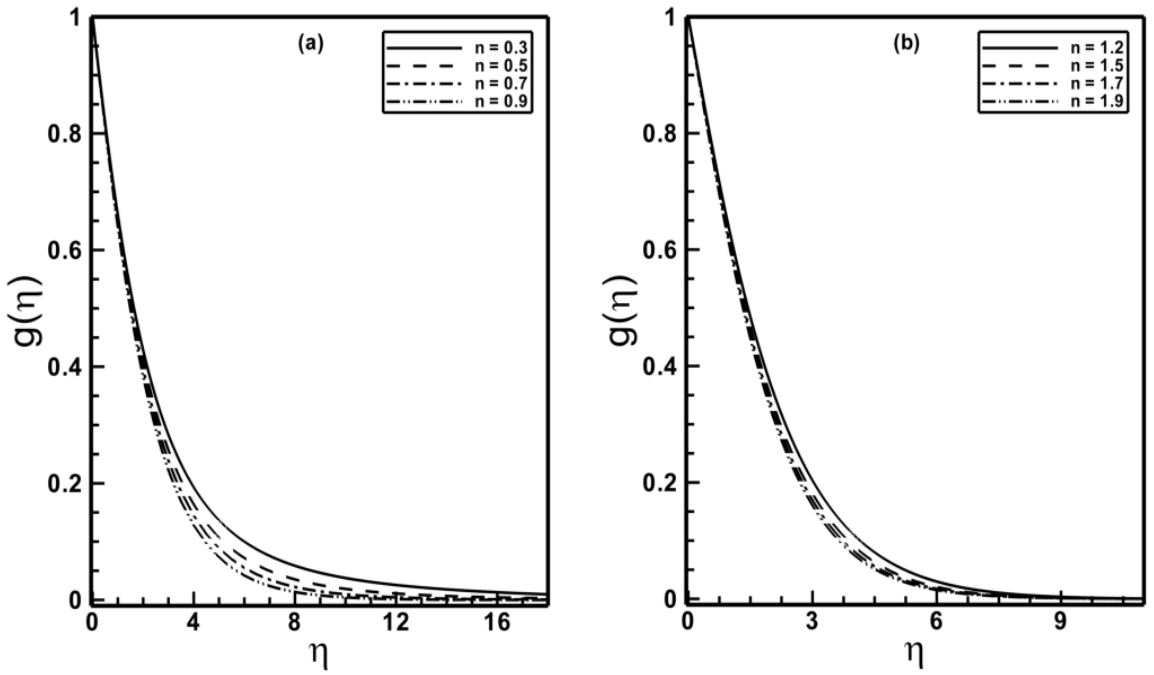

Figure 9.3: Profiles of the azimuthal velocity component $g(\eta)$ for different values of the power-law index when $A=1.5$ is fixed.

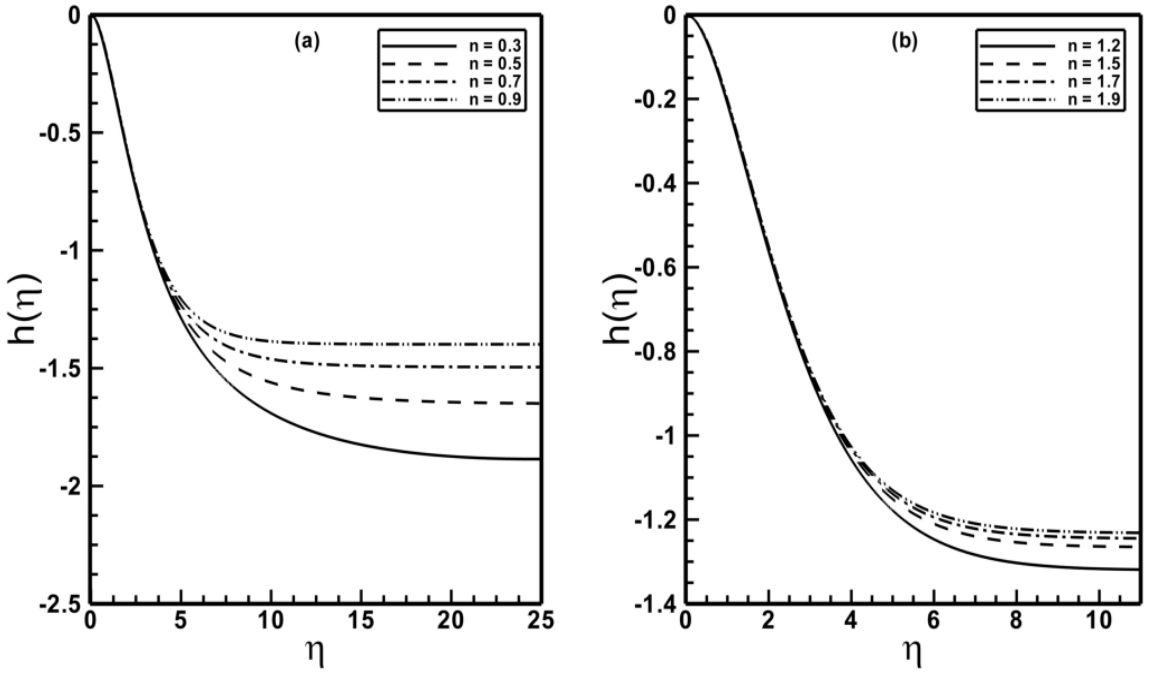

Figure 9.4: Profiles of the axial velocity component $h(\eta)$ for different values of the power-law index when $A=1.5$ is fixed.

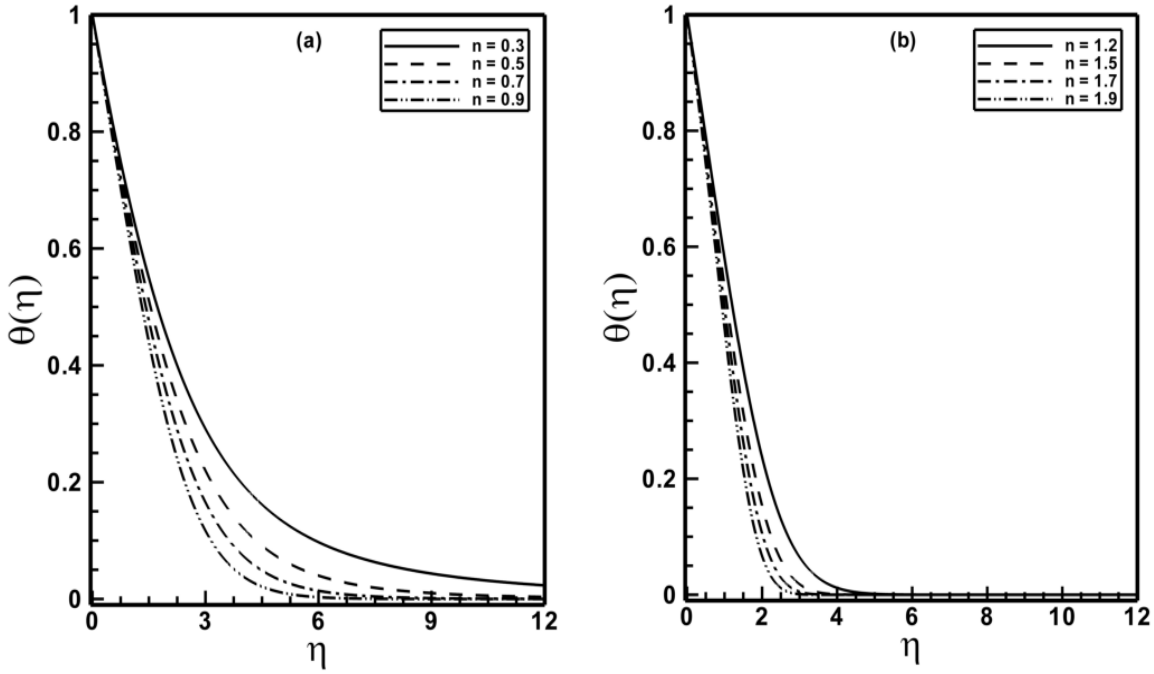

Figure 9.5: Profiles of the temperature $\theta(\eta)$ for different values of the power-law index when $A=1.5$ and $\Pr=2.0$ are fixed.

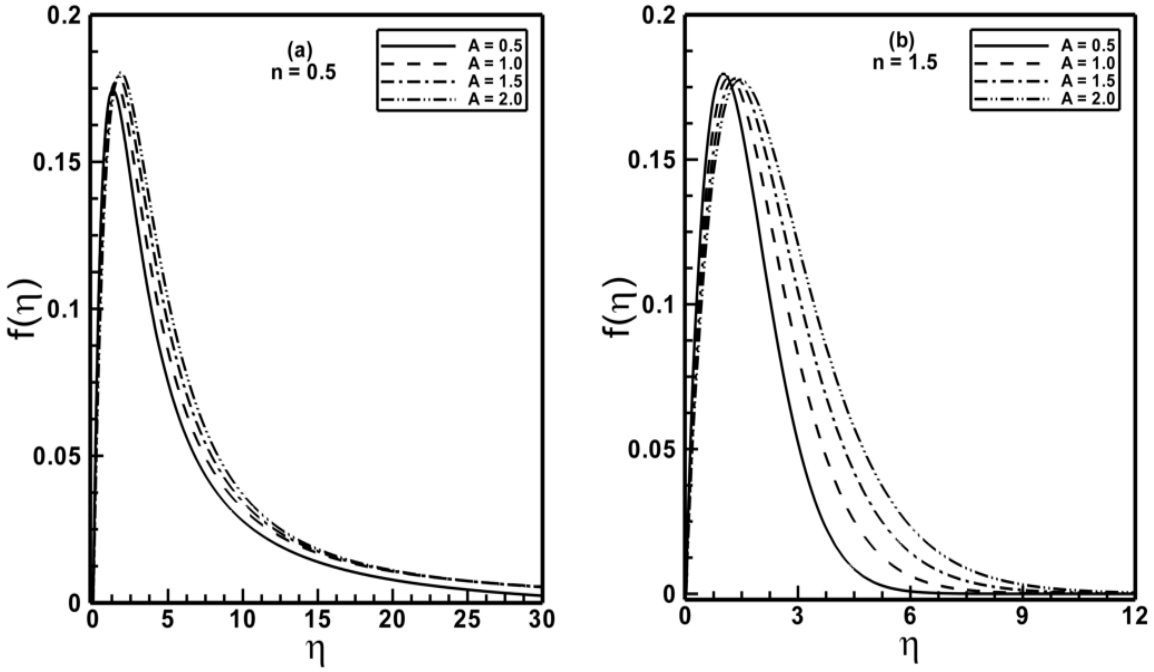

Figure 9.6: Profiles of the radial velocity component $f(\eta)$ for different values of the material parameter A of Sisko fluid.

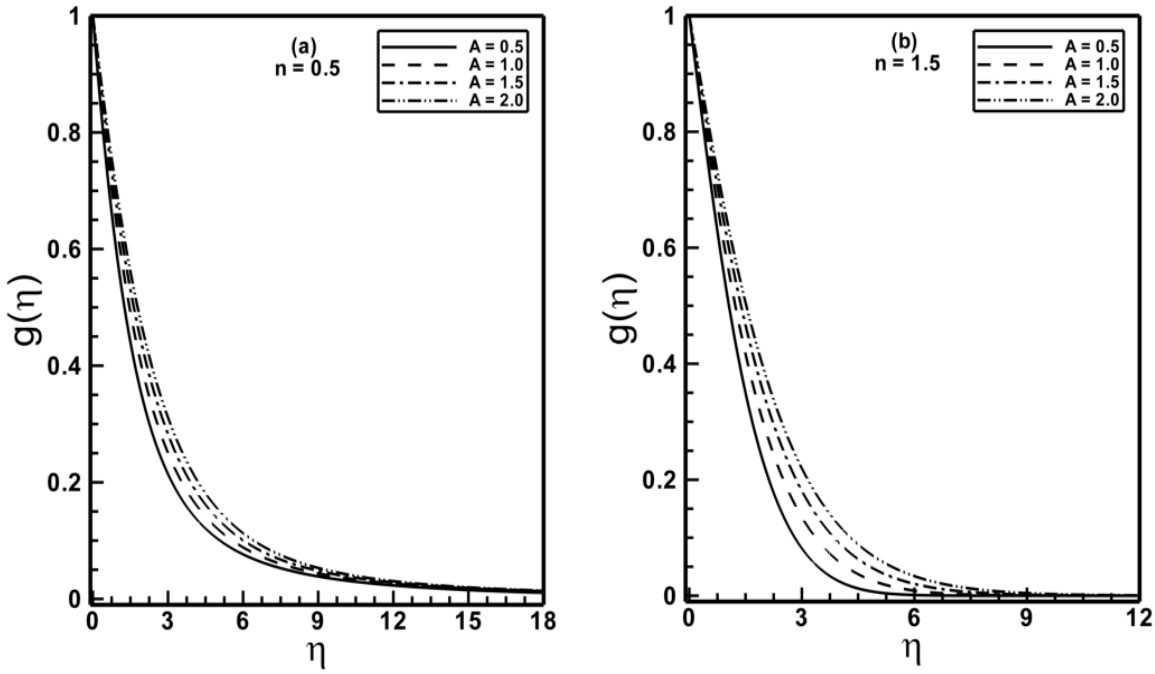

Figure 9.7: Profiles of the azimuthal velocity component $g(\eta)$ for different values of the material parameter A of Sisko fluid.

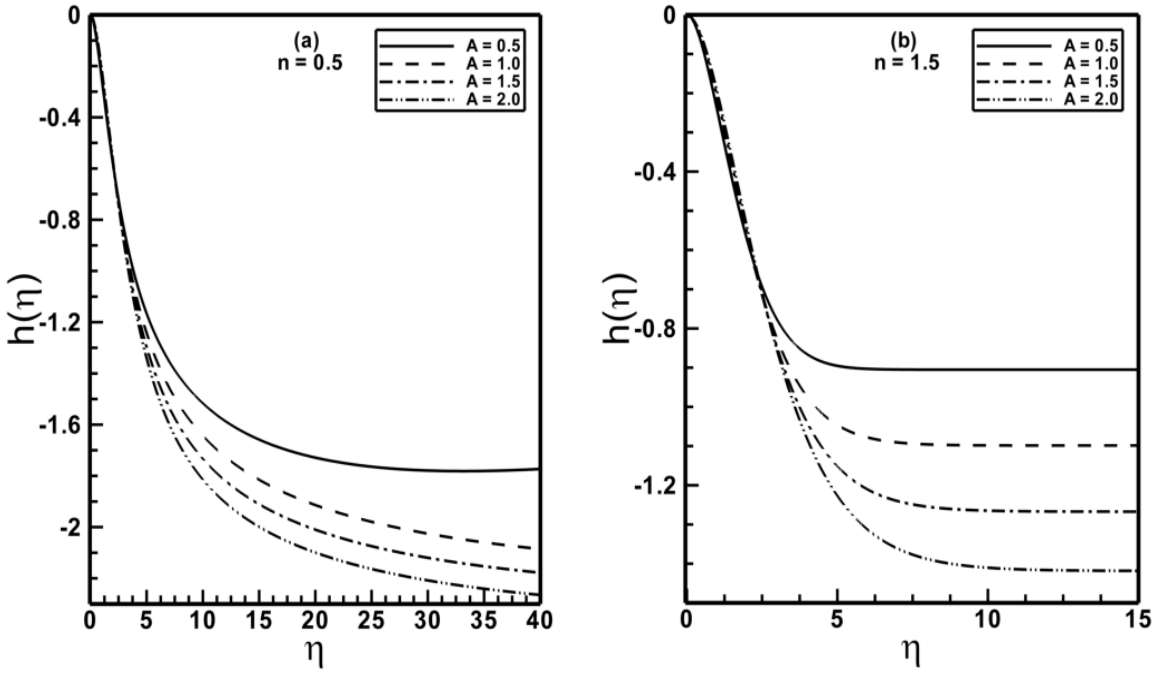

Figure 9.8: Profiles of the axial velocity component $h(\eta)$ for different values of the material parameter A of Sisko fluid.

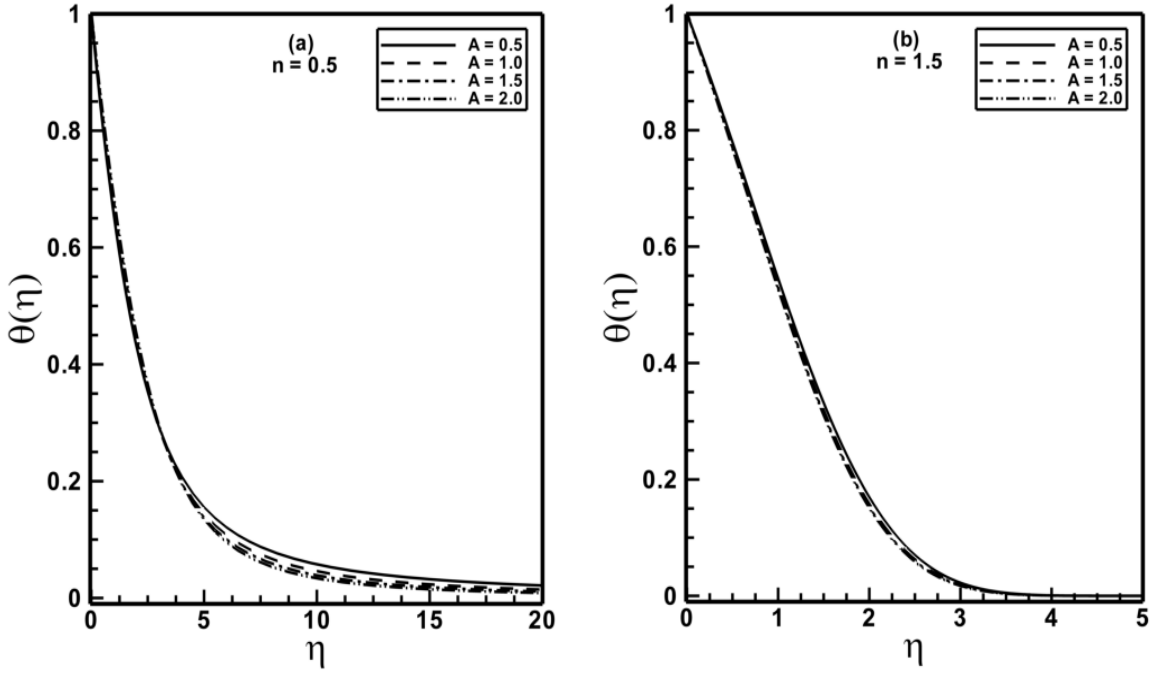

Figure 9.9: Profiles of the temperature $\theta(\eta)$ for different values of the material parameter A of Sisko fluid when $\Pr = 2$ is fixed.

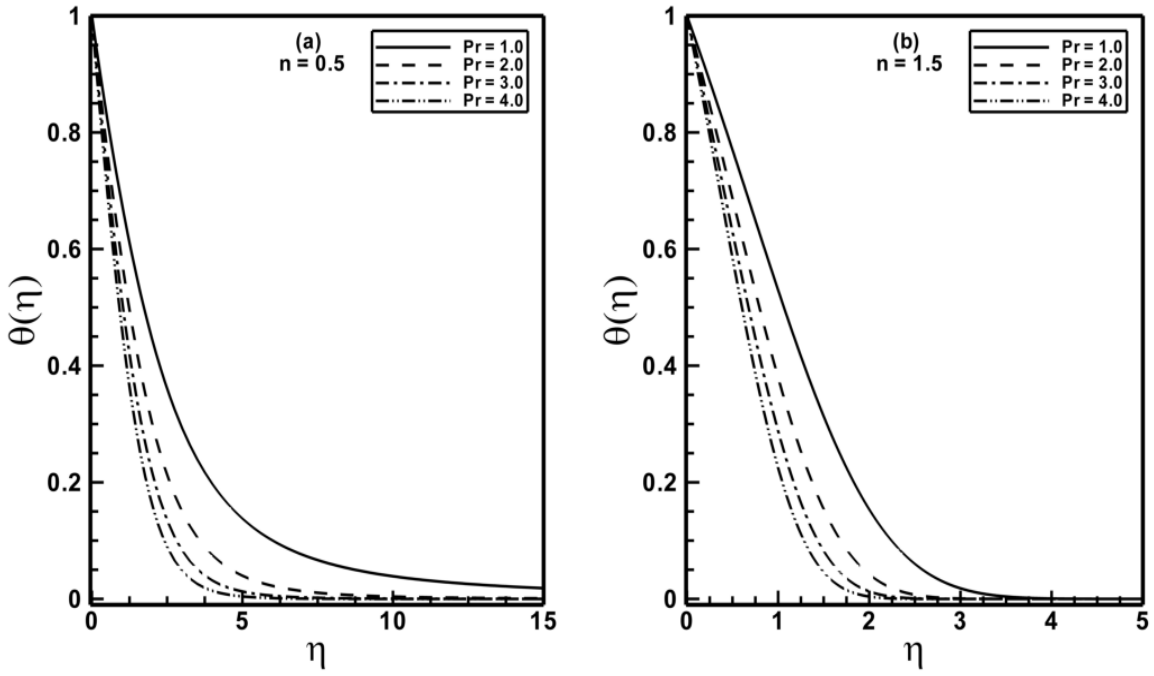

Figure 9.10: Profiles of the temperature $\theta(\eta)$ for different values of the Prandtl number Pr when $A=1.5$ is fixed.

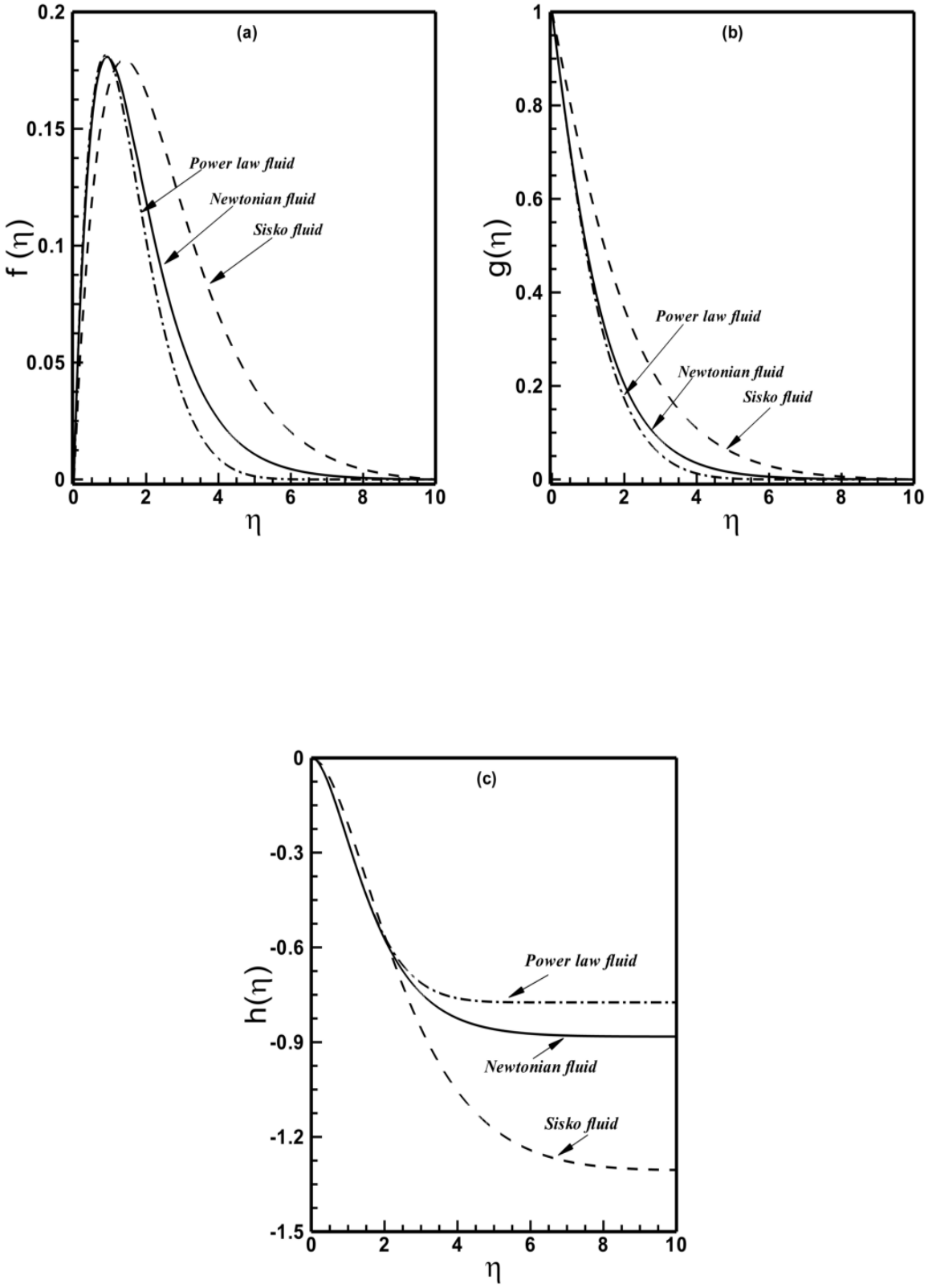

Figure 9.11:* A comparison of the radial, azimuthal and axial velocity components for different fluids.

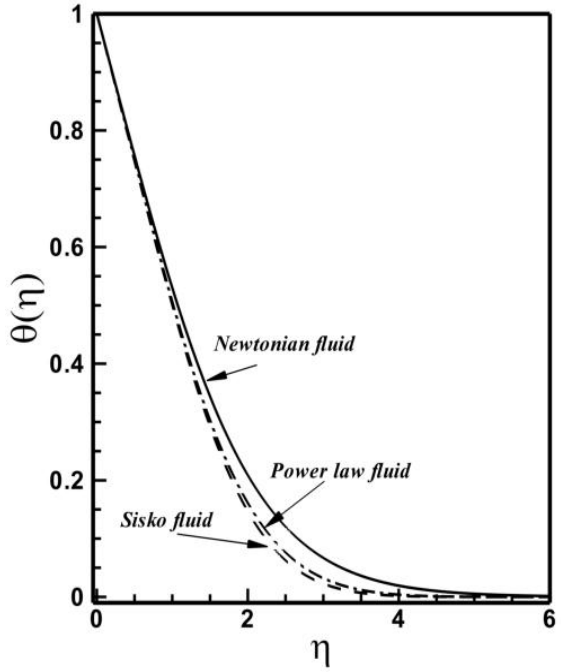

Figure 9.12:* A comparison of the temperature distribution for different fluids.

*Figures 9.11 and 9.12 are plotted for $A = 1.5,\ n = 1.2$ and $\Pr = 2$.

Chapter 10

Conclusions and Perspective

The aim of this thesis was to develop and contribute meaningful research in the promising field of non-Newtonian fluid mechanics. There is a little amount of research regarding non-Newtonian fluids particularly with respect to a non-Newtonian Sisko fluid in the literature and the main goal of this thesis was to fill this gap. In this thesis, we theoretically studied the flow and convective heat transfer to the Sisko fluid model. The thesis dealt with different flow configurations including the planar nonlinear stretching sheet, radially nonlinear stretching sheet, infinite wedge, stagnation point flow, bidirectional stretching sheet, and infinite rotating disk. Numerical solutions were obtained for nonlinear ordinary differential equations and the results were validated as a special case of the problem with exact analytic solutions and/or previously published pertinent literature. Effects of the relevant non-dimensional parameters such as the power-law index, stretching parameter, wall temperature parameter, material parameter of Sisko fluid, Prandtl number, Eckert number, wedge angle parameter, buoyancy parameter, velocity ratio parameter, temperature ratio parameter and radiation parameter on the velocity, temperature fields, skin friction coefficient and local Nusselt number have been analyzed. Additionally, a comparison amongst the Newtonian, power-law, Bingham plastic and Sisko fluids was made graphically. To grasp the understanding of the studies made in this work we have classified our research in six domains. Our computations have indicated the following.

As the value of the power-law index was increased the momentum boundary layer

and thermal boundary layer thicknesses decreased. The velocity and temperature profiles become more compact as the value of the power-law index was increased. The thermal boundary layer thickness was increased for the power-law-index $n<1,$ and decreased for $n\geq 1$ when the stretching parameter was increased and it affected the temperature profile strongly for the shear thickening regime. The parameter relating to the stretching in bidirectional stretching surface was the stretching ratio parameter. A qualitatively opposite trend was observed in the velocity components $f'(\eta)$ and $g'(\eta)$ for increasing value of the stretching ratio parameter. Further, a thinning of the thermal boundary layer was seen for increasing stretching ratio parameter and hence resulted in better heat transfer at the wall.

The material parameter of the Sisko fluid affects the temperature field almost to the same extent for the shear thinning and shear thickening Sisko fluids; however, effects were more dominant for low Prandtl number as compared to that of moderate and higher Prandtl numbers. Further, the temperature profile was seen to decrease as the value of the material parameter was incremented. For bidirectional stretching case, the thickness of the boundary layer for two lateral directions was the same, but thick in the shear thinning fluid as compared to that of the shear thickening fluid. The velocity profiles $f'(\eta)$ and $g'(\eta)$ augmented for each increment in the material parameter. Further, it was noted that there was an increase in the value of the local Nusselt number as the value of the material parameter was enhanced. Moreover, the local Nusselt number was larger for the radially stretching case compared to that of the planar stretching sheet. For the case of the rotating disk, the increase in material parameter increased the radial, azimuthal velocity components and axial inflow of the fluid. It was further observed that these velocity components respond vigorously for the shear thickening fluid.

The temperature profile increased when the Eckert number was incremented. The Eckert number affected dominantly for the highly shear thinning Sisko fluid and its effect went on decreasing as the value of Power law index was increased. For the same value of the Prandtl number, the value of adiabatic Eckert number was higher for the shear thickening fluid than that of the shear thinning fluid. Though, it was observed that thermal boundary layer thickness decreases as the Prandtl number was increased; however, for each value of the Prandtl number the thermal boundary layer thickness was slightly larger for shear thinning Sisko fluid. An exception exists for fluid flow over a rotating disk, where each Prandtl number possessed much thicker thermal boundary layer thickness for the shear thinning fluid compared to that of the shear thickening fluid.

Some conclusions regarding the wedge angle parameter were: an increase in the thermal boundary layer thickness was noticed as the value of the wedge angle parameter is decremented resulting in a decrease in heat transfer. The flow separation for the power-law index $n = 0.5$ and $n = 1.5$ corresponds to the expansion angle of $26 \cdot 2^{\circ}$ and $13 \cdot 4^{\circ}$, respectively. Theoretically, the shear thinning fluid has a stabilizing effect on the flow thereby delaying the separation of flow. It was further observed that the skin-friction coefficient was raised with each increment in the wedge angle parameter. Moreover, a sharp rise in the local Nusselt number was observed for the power-law index $n = 1.5$ when the wedge angle parameter was greater than one.

Some outcomes concerning the buoyancy parameter are as follows: it was concluded that for weakly assisting buoyant force the skin friction coefficient primarily was decreased then became constant with the power-law index. For intermediate assisting buoyant force, the skin friction coefficient firstly was increased then became constant with the power-law index. For opposing buoyant force the skin friction coefficient firstly

was decreased then approached a constant value as the power-law index increased. The buoyancy parameter exerted stronger influence on the local Nusselt number for shear thinning fluid. The skin friction coefficient was increased with an increase in the value of the material parameter and the shear thinning fluid was strongly affected with a change in the value of the buoyancy parameter. The local Nusselt number was increased for incremented values of the material parameter with a large variation in the value of the local Nusselt number for the shear thinning fluid.

Whilst comparing some other fluid models, it was observed that the power-law fluid has thinnest momentum boundary layer followed by Newtonian, Sisko and Bingham plastic fluids. On the other hand, a Sisko fluid has least thermal boundary layer thickness than those of the power-law, Newtonian and Bingham plastic fluids.

10.1 Future Recommendations

The research undertaken in this thesis has spanned a number of problems relating flow and heat transfer to a Sisko fluid. Although many problems still remain open to further investigation, the presented contributions bring us several steps forward in studying a non-Newtonian Sisko fluid. This study was restricted to the steady convective heat transfer to the Sisko fluid flows and an extension to unsteady convective heat transfer for three-dimensional and rotating flows to the Sisko fluid can be made. Moreover, we can propose the modeling and solutions of the fluid obeying the Cross model that encompass the whole viscosity-shear rate curve that is of more practical use, including the power-law and Sisko regions. It is worth mentioning that the Cross model can be reduced to the power-law and Sisko models.

In fact, it is the author's hope that the novel work presented here will assist the researchers in further development of non-Newtonian fluid mechanics.

References

[1] Sisko, A.W., *The Flow of Lubricating Greases,* Ind. Eng. Chem. Res., **50 (1)** (1958) 1789-1792.

[2] Barnes, H.A., Hutton, J.F. and Walters, K., *An Introduction to Rheology*, Elsevier, San Diego, (1989).

[3] NA, T.Y. and Hansen, A.G., *Radial flow of viscous non-Newtonian fluids between disks,* Int. J. Non-Linear Mech., **2** (1967) 261-273.

[4] Turian, R.M., Ma, T.W., Hsu, F.L.G. and Sung, M.D.I., *Flow of concentrated non-Newtonian slurries: 1, friction losses in laminar, turbulent and transition flow through straight pipe,* Int. J. Multiphase Flow, **24** (1998) 225-242.

[5] Xu, J., Rheology of Polymeric Suspensions: *Polymer Nano-composites and Waterborne Coatings, Industrial and Engineering Chemistry Coating*, Ph.D. Thesis, Ohio State University, (2005).

[6] Siddiqui, A.M., Ahmed, M. and Ghori, Q.K., *Thin film flow of non-Newtonian fluid on a moving belt,* Chaos, Solitons & Fractals, **33** (2007) 1006-1016.

[7] Siddiqui, A.M, Ansari, A.R., Ahmad, A. and Ahmad, N., *On Taylor's scraping problem and flow of a Sisko fluid,* Math. Model. Anal., **14** (2009) 515-529.

[8] Abelman, S., Hayat, T. and Momoniat, E., *On the Rayleigh problem for Sisko fluid in a rotating frame,* Appl. Math. Comput., **215** (2009) 2515-2520.

[9] Khan, M., Shaheen, N. and Shahzad, A., *Steady flow and heat transfer of a magnetohydrodynamic Sisko fluid through porous medium in annular pipe,* Int. J. Numer. Methods Fluids, **69** (2012) 1907-1922.

[10] Khan, M., Shahzad, A., Asia, A. and Mahomed, F.M., *Analytic approximate solutions for time-dependent flow and heat transfer of a Sisko fluid,* Int. J. Numer. Methods Heat Fluid Flow, **24 (5)** (2014) 1005-1019.

[11] Hayat, T., Moitsheki, R. J. and Abelman, S., *Stokes' first problem for Sisko fluid over a porous wall*, Appl. Math. Comput., **217** (2010) 622–628.

[12] Hayat, T., Abelman, S., Harley, C. and Hendi, A., *Stokes' first problem for a rotating Sisko fluid with porous space, J. Porous Media,* **15** (2012) 1079–1091.

[13] Gozde, S., Pakdemirli, M., Hayat, T. and Aksoy, Y., *Boundary layer equations and Lie group analysis of a Sisko fluid*, J. Appl. Math., **2012** (2012) 259608.

[14] Hayat, T., Abelman, S. and Hamese, M., *Oscillatory Couette flow of rotating Sisko fluid,* Appl. Math. Mech., **35(10)** (2014) 1301–1310.

[15] Schowalter, W.R., *The application of boundary layer theory to power-law pseudo-plastic fluids: Similar solutions*, AIChE J., **6** (1960) 24-28.

[16] Jadhav, B.P. and Waghmode, B.B., *Heat transfer to non-Newtonian power-law fluid past a continuously moving porous flat plate with heat flux*, Heat Mass Transf., **25** (1990) 377-380.

[17] Howel, T.G., Jeng, D.R. and Dewitt, K.J., *Momentum and heat transfer on a continuous moving surface in a power-law fluid*, Int. J. Heat Mass Transf., **40** (1997) 1853-1861.

[18] Hassanien, I.A., Abdullah, A.A. and Gorla, R.S.R., *Flow and heat transfer in a power-law fluid over a non-isothermal stretching sheet*, Math. Comput. Modell., **28** (1998) 105-116.

[19] Able, M.S., Datti, P.S. and Mahesha, N., *Flow and heat transfer in a power-law fluid over a stretching sheet with variable thermal conductivity and non-uniform heat source*, Int. J. Heat Mass Transf., **52** (2009) 2902-2913.

[20] Xu, H. and Liao, S.J., *Laminar flow and heat transfer in the boundary-layer of non-Newtonian fluids over a stretching flat sheet*, Comput. Math. Appl., **57** (2009) 1425-1431.

[21] Chen, C.H., *Effects of magnetic field and suction/injection on convection heat transfer of non-Newtonian power-law fluids past a power-law stretched sheet with surface heat flux*, Int. J. Therm. Sci., **47** (2008) 954–961.

[22] Prasad, K.V. and Vajravelu, K., *Heat transfer in the MHD flow of a power law fluid over a non-isothermal stretching sheet*, Int. J. Heat Mass Transf., **52** (2009) 4956–4965.

[23] Prasad, K.V., Pal, D. and Datti, P.S., *MHD power-law fluid flow and heat transfer over a non-isothermal stretching sheet*, Commun. Nonlinear. Sci. Numer. Simulat., **14** (2009) 2178–2189.

[24] Khan, M. and Shahzad, A., *On boundary layer flow of Sisko fluid over stretching sheet*, Quaest. Math., **36** (2013) 137-151.

[25] Khan, M. and Shahzad, A., *On axisymmetric flow of Sisko fluid over a radially stretching sheet*, Int. J. Non-Linear Mech., **47** (2012) 999-1007.

[26] Falkner, V.M. and Skan, S.W., *Some approximate solutions of the boundary layer equations*, Philosophical Magazine, **12** (1931) 865-896.

[27] Lin, H.T. and Lin, L.K., *Similarity solutions for laminar forced convection heat transfer from wedges to fluids of any Prandtl number*, J. Heat Mass Transf., **30** (1987) 1111-1118.

[28] Hsu, C.H., Chen, C.S. and Teng, J.T., *Temperature and flow fields for the flow of a second grade fluid past a wedge*, Int. J. Non-Linear Mech., **32** (1997) 933-946.

[29] Pantokratoras, A., *The Falkner–Skan flow with constant wall temperature and variable viscosity*, Int. J. Therm. Sci., **45** (2006) 378–389.

[30] Kuo, B.L., *Heat transfer analysis for the Falkner-Skan wedge flow by the differential transformation method*, Int. J. Heat Mass Transf., **48** (2005) 5036-5046.

[31] Kim, Y.J., *The Falkner-Skan wedge flows of power-law fluids embedded in a porous medium*, Transp. Porous Media, **44** (2001) 267-279.

[32] Chen, J.L.S. and Radulovic, P.T., *Heat transfer in non-Newtonian flow past a wedge with non-isothermal surfaces*, J. Heat Transf., **95** (1973) 498-503.

[33] Postelnicu, A. and Pop, I., *Falkner-Skan boundary layer flow of a power-law fluid past a stretching wedge*, Appl. Math. Comput., **217** (2011) 4359-4368.

[34] Rashidia, M.M., Rastegaria, M.T., Asadia, M. and Bég, O.A., *A study of non-Newtonian flow and heat transfer over a non-isothermal wedge using the homotopy analysis method*, Chem. Eng. Commun., **199** (2012) 231-256.

[35] Khan, M. and Shahzad, A., *Falkner-Skan boundary layer flow of a Sisko fluid*, Zeitschrift für Naturforschung A, **67a** (2012) 469-478.

[36] Wang, T.Y., *Mixed convection heat transfer from a vertical plate from a non-Newtonian fluid*, Int. J. Heat Fluid Flow, **16** (1995) 56-61.

[37] Hady, F.M., *Mixed convection boundary layer flow of non-Newtonian fluids on a horizontal plate*, Appl. Math. Comput., **68** (1995) 105-112.

[38] Chen, C.H., *Laminar mixed convection adjacent to vertical continuously stretching sheet*, Heat Mass Transf., **33** (1998) 471-476.

[39] Chen, C.H., *Magneto-hydrodynamic mixed convection of a power-law fluid past a stretching surface in the presence of thermal radiation and internal heat generation/absorption*, Int. J. Non-Linear Mech., **44** (2009) 596-603.

[40] Saleem, A.M., Aziz, M.A., Eldahab, E.M. and Elfatah, I.A., *Effect of variable density on hydromagnetic mixed convection flow of a non-Newtonian fluid past a moving vertical plate*, Commun. Nonlinear Sci. Numer. Simulat., **15** (2010) 1485-1493.

[41] Barletta, A., *Combined forced and free flow of a power-law fluid in a vertical annular duct*, Int. J. Heat Mass Transf., **43** (2000) 3673-3686.

[42] Mohammadein, A.A. and El-Amin, M. F., *Thermal radiation effects on power law fluid over a horizontal plate embedded in porous medium*, Int. Commun. Heat Mass Transf., **27** (2000) 1025-1035.

[43] Elgazery, N.S., *An implicit-Chebyshev pseudospectral method for the effect of radiation on power-law fluid past a vertical plate immersed in a porous medium*, Commun. Nonlinear Sci. Numer. Simulat., **13** (2008) 728-744.

[44] Kishan, N and Kavitha, P., *MHD non-Newtonian power law fluid flow and heat transfer past a non-linear stretching surface with thermal radiation and viscous dissipation*, J. Appl. Sci. Eng., **17** (2014) 267-274.

[45] Wang, C.Y., *The three dimensional flow due to a stretching flat surface*, Phys. Fluids, **27** (1984) 1915-1917.

[46] Ariel, P.D., *Generalized three-dimensional flow due to a stretching sheet*, Z. Angew. Math. Mech., **83** (2003) 844-852.

[47] Liu, I.C. and Andersson, H.I., *Heat transfer over a bidirectional stretching sheet with variable thermal conditions*, Int. J. Heat Mass Transf., **51** (2008) 4018-4024.

[48] Lakshmisha, K.N., Nath, G. and Venkateswaran, S., *Three-dimensional unsteady flow with heat and mass transfer over a continuous stretching surface*, J. Heat Transf., **110 (3)** (2009) 590-595.

[49] Ahmad, I., Ahmad, M., Abbas, Z. and Sajid, M., *Hydromagnetic flow and heat transfer over a bidirectional stretching surface in a porous medium*, Thermal Sci., **15** (2011) Suppl. 2 S205-S220.

[50] Gorla, R.S.R, Pop, I. and Dakappagari, V., *Three-dimensional flow of a power-law fluid due to a stretching flat surface*, Z. Angew. Math. Mech., **75** (1995) 389-394.

[51] Nadeem, S., Haq, R.U., Akbar, N. S. and Khan, Z.H., *MHD three-dimensional Casson fluid flow past a porous linearly stretching sheet*, Alexandria Eng. J., **52** (2013) 577-582.

[52] Shehzad, S.A., Alsaedi, A. and Hayat, T., *Hydromagnetic steady flow of Maxwell fluid over a bidirectional stretching surface with prescribed surface temperature and prescribed heat flux*, PLoS ONE, **8 (7)** (2013) e68139.

[53] Shehzad, S.A., Alsaedi, A., Hayat, T. and Alhuthali, M.S., *Three-dimensional flow of an Oldroyd-B fluid with variable thermal conductivity and heat*

generation/absorption, PLoS ONE, **8 (11)** (2013) e78240.

[54] Shehzad, S.A., Alsaedi, A., Hayat, T., Alhuthali, M.S. and Asghar, S., *MHD three-dimensional flow of Jeffrey fluid with Newtonian heating*, J. Cent. South Uni., **21** (2014) 1428-1433.

[55] Sparrow, E.M. and Gregg, J.L., *Heat transfer from a rotating disk to fluids of any Prandtl number*, J. Heat Transf., **81** (1959) 249–251.

[56] Riley, N., *The heat transfer from a rotating-disk*, Q. J. Mech. Appl. Math., **17** (1964) 331–349.

[57] Turkyilmazoglu, M., *Exact solutions for the incompressible viscous fluid of a rotating disk flow*, Prog. Appl. Math., **1** (2011) 90–97.

[58] Erdogan, M.E., *Flow due to parallel disks rotating about non-coincident axis with one of them oscillating in its plane*, Int. J. Non-Linear Mech., **34** (1999) 1019–1030.

[59] Andersson, H.I., de Korte, E. and Meland, R., *Flow of a power-law fluid over a rotating disk revisited*, Fluid Dyn. Res., **28** (2001) 75-88.

[60] Andersson, H. I. and de Korte, E., *MHD flow of a power-law fluid over a rotating disk*, Eur. J. Mech. B/Fluids, **21** (2002) 317–324.

[61] Attia, H.A., *Rotating disk flow and heat transfer through a porous medium of a non-Newtonian fluid with suction and injection*, Commun. Nonlinear Sci. Numer. Simulat., **13** (2008) 1571–1580.

[62] Ming, C., Zheng, L. and Zhang, X., *Steady flow and heat transfer of the power-law fluid over a rotating disk*, Int. Commun. Heat Mass Transf., **38** (2011) 280–284.

[63] Khan, M. and Shahzad, A., *On stagnation point flow of Sisko fluid over stretching sheet*, Meccanica, **48** (2013) 2391-2400.

[64] Chhabra, R.P. and Richardson, J.F., *Non-Newtonian Flow and Applied Rheology: Engineering Applications*, Burlington, Elsevier (2008).

[65] Sewell, G., *The Numerical Solution of Ordinary and Partial Differential Equations*, New Jersey, John Wiley & Sons. Inc. (2005).

[66] Na, T.Y., *Computational Methods in Engineering Boundary Value Problems*, London, Academic Press, Inc. (1979).

[67] Kunes, J., *Dimensionless Physical Quantities in Science and Engineering*, Czech Republic, Elsevier (2012).

[68] Mahapatra, T.R., Nandy, S.K. and Gupta, A.S., *Analytical solution of magnetohydrodynamic stagnation-point flow of a power-law fluid towards a stretching surface*, App. Math. Comput., **215** (2009) 1696–1710.

[69] Dandapat, B.S., Singh, S.N. and Singh, R.P., *Heat transfer due to permeable stretching wall in presence of transverse magnetic field*, Arch. Mech., **56** (2004) 87-101.

[70] Deshpande, A.P., Krishnan, J.M. and Kumar, S., *Rheology of Complex Fluids*, London, Springer (2010).

[71] Berk, Z., *Food Processing Engineering and Technology*, New York, Academic Press (2008).

[72] Chhabra, R.P., *Bubbles, Drops and Particles in Non-Newtonian Fluids*, Second Ed. Boca Raton, FL, CRC Press (2006).

[73] Shahzad, A., Ali, R. and Khan M., *On the exact solution for axisymetric flow and heat transfer over a nonlinear radially stretching sheet*, Chin. Phys. Lett., **29** (2012) 084705.

[74] White, F.M., *Viscous Fluid Flow*, New York, McGraw Hill (2011).

[75] Liao, S.J., *Homotopy Analysis Method in Nonlinear Differential Equations*, London, Springer (2012).

[76] Pantokratoras, A. and Fang, T., *Sakiadis flow with nonlinear Rosseland thermal radiation*, Physica Scripta, **87** (2013) 015703.

[77] Mitschka P. and Ulbrecht J., *Nicht-Newtonsche Flüssigkeiten IV. Strömung Nicht-Newtonscher Flüssigkeiten Ostwald-de Waeleschen Typs in der Umgebung Rotierender Drehkegel und Schieben*, *Coll*., Czech. Chem. Comm. **30** (1965) 2511–2526.